Three-dimensional Models of Core-collapse Supernovae From Low-mass Progenitors With Implications for Crab

G. Stockinger[1,2], H.-T. Janka[1][⋆], D. Kresse[1,2], T. Melson[1], T. Ertl[1], M. Gabler[3],

A. Gessner[4,5], A. Wongwathanarat[1], A. Tolstov[6], S.-C. Leung[7], K. Nomoto[8],

A. Heger[9−13]

[1]*Max Planck Institute for Astrophysics, Karl-Schwarzschild-Str. 1, 85748 Garching, Germany*
[2]*Physik-Department, Technische Universität München, James-Franck-Str. 1, 85748 Garching, Germany*
[3]*LATO/DCET, Universidade Estadual de Santa Cruz, Rod. Jorge Amado, km 16, Ilhéus, BA, CEP 45662-900, Brazil*
[4]*University of Tübingen, Maria-von-Linden-Str. 6, 72076 Tübingen, Germany*
[5]*Max Planck Institute for Intelligent Systems, Max-Planck-Ring 4, 72076 Tübingen, Germany*
[6]*The Open University of Japan, 2–11, Wakaba, Mihama-ku, Chiba, Chiba 261–8586, Japan*
[7]*TAPIR, Walter Burke Institute for Theoretical Physics, Mailcode 350-17, Caltech, Pasadena, CA 91125, USA*
[8]*Kavli Institute for the Physics and Mathematics of the Universe (WPI), The University of Tokyo Institute for Advanced Study,*
The University of Tokyo, Kashiwa, Chiba 277-8583, Japan
[9]*School of Physics & Astronomy, Monash University, Clayton 3800, Victoria, Australia*
[10]*Joint Institute for Nuclear Astrophysics, 1 Cyclotron Laboratory, National Superconducting Cyclotron Laboratory,*
Michigan State University, East Lansing, MI 48824-1321, USA
[11]*Tsung-Dao Lee Institute, Shanghai 200240, China*
[12]*Center of Excellence for Astrophysics in Three Dimensions (ASTRO-3D), Australia*
[13]*Australian Research Council Centre of Excellence for Gravitational Wave Discovery, Clayton, VIC 3800, Australia*

ABSTRACT

We present 3D full-sphere supernova simulations of non-rotating low-mass ($\sim 9\,\mathrm{M}_\odot$) progenitors, covering the entire evolution from core collapse through bounce and shock revival, through shock breakout from the stellar surface, until fallback is completed several days later. We obtain low-energy explosions ($\sim$0.5–1.0 $\times 10^{50}$ erg) of iron-core progenitors at the low-mass end of the core-collapse supernova (LMCCSN) domain and compare to a super-AGB (sAGB) progenitor with an oxygen-neon-magnesium core that collapses and explodes as electron-capture supernova (ECSN). The onset of the explosion in the LMCCSN models is modelled self-consistently using the VERTEX-PROMETHEUS code, whereas the ECSN explosion is modelled using parametric neutrino transport in the PROMETHEUS-HOTB code, choosing different explosion energies in the range of previous self-consistent models. The sAGB and LMCCSN progenitors that share structural similarities have almost spherical explosions with little metal mixing into the hydrogen envelope. A LMCCSN with less 2nd dredge-up results in a highly asymmetric explosion. It shows efficient mixing and dramatic shock deceleration in the extended hydrogen envelope. Both properties allow fast nickel plumes to catch up with the shock, leading to extreme shock deformation and aspherical shock breakout. Fallback masses of $\lesssim 5\times 10^{-3}\,\mathrm{M}_\odot$ have no significant effects on the neutron star (NS) masses and kicks. The anisotropic fallback carries considerable angular momentum, however, and determines the spin of the newly-born NS. The LMCCSN model with less 2nd dredge-up results in a hydrodynamic and neutrino-induced NS kick of $>40\,\mathrm{km\,s^{-1}}$ and a NS spin period of $\sim$30 ms, both not largely different from those of the Crab pulsar at birth.

Key words: Key words: supernovae: general – supernovae: individual: Crab – stars: massive – stars: neutron – neutrinos – hydrodynamics

1 INTRODUCTION

According to current understanding stars with initial masses of $\gtrsim 8$–$9\,\mathrm{M}_\odot$ end their lives in a core-collapse supernova (CCSN).

⋆ Email: thj@mpa-garching.mpg.de

The explosion is powered by gravitational energy, which is released when the core of the star collapses to a compact remnant (a neutron star or black hole), and a fraction of which is transferred to the ejecta by neutrino-energy deposition (Bethe & Wilson 1985; Colgate & White 1966). In the past six decades, numerous studies have focused on the collapse phase and subsequent evolution using 1D simulations. Over the past three decades, multi-dimensional simulations with successively improved treatment of the microphysics have driven our understanding of the explosion mechanism (see e.g. Janka et al. 2012; Janka 2012; Burrows 2013; Janka et al. 2016; Müller 2016). A close analysis of these models led to the discovery of new hydrodynamic instabilities such as the standing accretion shock instability (SASI) (Blondin et al. 2003; Blondin & Mezzacappa 2007; Ohnishi et al. 2006; Foglizzo et al. 2007; Fernández 2010). The increase of computational capabilities in the recent years along with new developments for neutrino transport methods (see, e.g. Buras et al. 2006; Takiwaki et al. 2012; O'Connor & Couch 2018a; Skinner et al. 2019; Glas et al. 2019a and references therein) have enabled full 3D simulations of the early explosion phase (see e.g. Takiwaki et al. 2014; Couch & O'Connor 2014; Melson et al. 2015a,b; Lentz et al. 2015; Summa et al. 2016; Roberts et al. 2016; Müller et al. 2017, 2018; Vartanyan et al. 2018; Ott et al. 2018; O'Connor & Couch 2018b; Melson et al. 2020; Vartanyan et al. 2019; Burrows et al. 2019).

Motivated by the historical SN1987A and its progenitor detection, a variety of studies in two and three dimensions also investigated the propagation of the shock wave from its initiation to its breakout from the stellar surface in 15–20 $M_\odot$ blue supergiant (BSG) models, which are suitable as progenitors of SN1987A. In first studies, the blast wave was launched through artificial energy deposition near the center (see e.g. Nomoto et al. 1987, 1988; Arnett et al. 1989b; Müller et al. 1991b; Fryxell et al. 1991), later the explosion was initiated with the neutrino-driven mechanism (see Kifonidis et al. 2003; Hammer et al. 2010; Wongwathanarat et al. 2013; Wongwathanarat et al. 2015). Müller et al. (2018) followed the long-time evolution of the explosion of ultra-stripped progenitors by 3D simulations, motivated by the importance of such stars in understanding the progenitor systems of the recent detections of NS-NS mergers by LIGO/Virgo (GW170817, Abbott et al. 2017, and GW190425, Abbott et al. 2020).

These theoretical works showed that supernova (SN) explosions are by far not spherical events as previously thought. Three-dimensional instabilities facilitate the explosion (Herant et al. 1994; Burrows et al. 1995; Janka & Müller 1996) and are a necessary ingredient to explain the clumpiness and mixing found in photospheric emission (Utrobin et al. 2015, 2017) and spectral analyses of the nebular phase of core-collapse events (Jerkstrand 2017). Wongwathanarat et al. (2015) showed that the final ejecta distribution carries imprints of the asphericities produced during the onset of the explosion ($t \sim 1$ s), which are further modified during later phases. Depending on the detailed progenitor structure, hydrodynamic instabilities arising at the composition interfaces, such as the Rayleigh-Taylor (RT) instability and the Richtmeyer-Meshkov (RM) instability, shape the final spatial and velocity distributions of nucleosynthetic products. The resulting ejecta morphology ranges from quasi-spherical ejecta (Müller et al. 2018) to strongly pronounced RT-fingers including cases that resemble the geometry found in Cas A (Wongwathanarat et al. 2017; Grefenstette et al. 2017). Due to the highly nonlinear and stochastic behaviour of non-radial instabilities and turbulence during the onset of the explosion phase and the subsequent evolution of RT instabilities, which depend on the progenitor structure, a clear connection between the asymmetries,

and thus the degree of mixing, and the progenitor properties has still to be worked out.

In this paper, we consider CCSN progenitors with initial masses near the low-mass end of about 9–10 $M_\odot$, where around 20% of all CCSNe are thought to occur (assuming a Salpeter initial mass function Salpeter 1955 and an upper mass limit of $\sim 20 M_\odot$ for CCSNe), to study the differences in their development of mixing instabilities during the explosion. To this end, we compare ECSNe from a super-AGB progenitor with an ONeMg core and CCSNe from red supergiant (RSG) progenitors with iron cores, all in a zero-age main sequence (ZAMS) mass range around 9 $M_\odot$.

The evolution of stars with masses $\lesssim 12 M_\odot$ is very sensitive to the initial stellar mass, various pulsational instabilities, and mass-loss phenomena (Woosley & Heger 2015). Iron-core CCSN progenitors with initial masses around 9–10 $M_\odot$ ignite oxygen burning off-center in contrast to their more massive ($M > 15 M_\odot$) counterparts. After oxygen burning, silicon ignites in a degenerate flash which might, in some cases, lead to additional mass loss in the last decade of evolution or is speculated to even eject parts of the hydrogen envelope (Woosley & Heger 2015).

The 8.8 $M_\odot$ progenitor of Nomoto (1984) is even more peculiar. It experiences several thermal pulses and off-center ignition of fusion material. In the end, it has a degenerate ONeMg-core surrounded by a dilute and extended hydrogen envelope.

When the core approaches its Chandrasekhar mass, electron captures on ^{24}Mg and ^{20}Ne via the reaction chains ^{24}Mg$(e^-, \nu_e)^{24}$Na$(e^-, \nu_e)^{24}$Ne and ^{20}Ne$(e^-, \nu_e)^{20}$F$(e^-, \nu_e)^{20}$O (Miyaji et al. 1980) destabilize the core due to a reduction of the effective adiabatic index of the electron-degeneracy dominated gas pressure. Continuous electron capture on ^{20}Ne, which further reduces the pressure support, works against the now beginning oxygen-burning as temperatures increase during the collapse. Simulations in 1D (see Kitaura et al. 2006; Hüdepohl et al. 2010; Fischer et al. 2010) and 2D (see Janka et al. 2008; Radice et al. 2017) suggest that the collapse proceeds despite the oxygen burning. Jones et al. (2016) simulated the deflagration of oxygen in ONeMg cores with different core densities. At $\log_{10}(\rho_c / \mathrm{g\,cm}^{-3}) = 9.95$ and lower densities their cores do not collapse but get partly unbound due to the inefficient semi-convective mixing during the electron-capture phase and the resulting strong thermonuclear runaway. Only when the central densities are higher than this threshold value of ρ_c, the core is found to collapse to a proto-neutron star (PNS). Recently, Kirsebom et al. (2019) investigated the influence of a newly measured strong transition between the ground states of ^{20}Ne and ^{20}F on the electron-capture rate and thus on the evolution of ONeMg cores. Adding the new transition increases the likelihood that the star is (partially) disrupted by a thermonuclear explosion (termed tECSN) rather than collapsing to form a PNS. However, Zha et al. (2019), using state-of-the-art electron-capture rates including the latest rate for the second forbidden transition of ^{20}Ne$(e^-, \nu_e)^{20}$F from Suzuki et al. (2019), found that the oxygen deflagration starting from $\log_{10}(\rho_c / \mathrm{g\,cm}^{-3}) > 10.01$ (< 10.01) leads to collapse (thermonuclear explosion). Their estimate of the central density when the oxygen deflagration is initiated in an evolving ONeMg core exceeds this critical value. Therefore they conclude that ONeMg cores are likely to collapse.

For this reason, in our study we assume that the ONeMg core collapses to a PNS, leading to a "collapse ECSN" (cECSN). This assumption receives additional motivation by the fact that recent studies considering the galactic chemical evolution of the Milky Way stress the importance of cECSNe to reproduce the solar abundances of several important and problematic isotopes including,

e.g., ^{48}Ca, ^{50}Ti, and several of the isotopes from Zn to Zr (Jones et al. 2019).

Despite the narrow range of central densities for which cEC-SNe are expected to occur (Leung et al. 2020), and despite the open questions associated with a variety of competing processes that decide about collapse or thermonuclear explosion and that depend strongly on many uncertain aspects of the employed physics, connections to cECSNe have been made for observations of SN1994N, 1997D, 1999br, 1999eu, 2011dc and 2005cs (Stevenson 2014). However, comparisons of the nebular spectra of some of these cases with 1D neutrino-driven SN models are ambiguous or disfavor the link to cECSNe (Jerkstrand et al. 2018). Also SN1054 (the Crab) has been speculated to be a cECSN (Nomoto et al. 1982; Hillebrandt 1982; Tominaga et al. 2013; Smith 2013), although such an interpretation is in conflict with results by Gessner & Janka (2018) for the maximum kick velocity of PNSs produced by cECSNe.

With the help of full-sphere three-dimensional simulations we aim at investigating the following questions:

• What are the differences in the early stages (first seconds) of the explosion in low-mass Fe-core and ONeMg-core progenitors?
• What is the influence of the different progenitor structures on the long-time evolution of the explosion? In particular, what is the influence on the formation of reverse shocks and the efficiency of outward mixing of neutrino-heated material?
• Are CCSNe of low-mass progenitors able to produce highly asymmetric ejecta and strong radial mixing of metals similar to findings for more massive RSG and BSG stars in previous studies?
• How do the properties of the compact remnants change on long time-scales due to the fallback of matter? Are there significant changes to the remnants' mass, kick, and angular momentum?

The structure and contents of our paper are the following: In Section 2, the basic properties of the considered models of non-rotating, low-mass (super-AGB and RSG) progenitors are introduced. Section 3 provides a brief description of the numerical methods and input physics used in our simulations. Section 4 contains our results for the first second(s) of the explosion, focusing on shock dynamics, explosion energies, neutrino emission, PNS properties and the chemical composition of the ejecta. In Section 5, for the first time in 3D explosion modeling, the SN evolution of low-mass super-AGB and RSG progenitors is described until and beyond shock breakout concerning the development of mixing instabilities and ejecta asymmetries, the spatial distribution of chemical elements, and the effects of fallback on the properties of the newly formed NSs. In Section 6, we briefly compare our results with previous studies, and in Section 7, we conclude with a summary and discussion. Several appendices contain basic information on more technical aspects concerning the simulation inputs and the analysis methods.

2 PROGENITORS

In this paper, we study an ECSN of a non-rotating 8.8 M$_\odot$ super-AGB star (e8.8), which is constructed from the envelope model of Jones et al. (2013) and a collapsing core model (Leung et al. 2020; A. Tolstov, S.-C. Leung, and K. Nomoto, 2017, private communication), and two CCSNe resulting from non-rotating low-mass RSGs with iron cores (z9.6, s9.0), evolved to the onset of collapse by A. Heger (2015, private communication) and by Woosley & Heger (2015), respectively. The considered ECSN progenitor is explored

here for the first time, whereas the explosions of the iron core progenitors were simulated in 3D with the Vertex-Prometheus code and some results were published in Melson et al. (2015a) and Melson et al. (2020).

2.1 ONeMg-core progenitor

Model e8.8 is a solar-metallicity progenitor with a ZAMS mass of $M_{\rm ZAMS} = 8.8\,{\rm M_\odot}$. Its degenerate ONeMg-core undergoes electron capture which ignites the O-Ne deflagration at the center. The central density ($\rho_{\rm c}$) and the electron fraction (Y_e), and thus the core mass M(ONeMg) at the ignition, depend on the convective stability criterion, extent of the convective mixing, and the electron capture rate (Zha et al. 2019). Leung et al. (2020) adopted the core with $\rho_{\rm c} \sim 10^{9.975}\,{\rm g\,cm^{-3}}$, $Y_e = 0.496$, and M(ONeMg) $= 1.39\,{\rm M_\odot}$, and calculated the propagation of the convective deflagration. The deflagration incinerates ONeMg-core material into nuclear statistical equilibrium (NSE). In the NSE region, electron capture on iron-group nuclei and free protons dominates nuclear energy release, thus inducing collapse. When the central density reaches $\rho_{\rm c} \sim 10^{10.64}\,{\rm g\,cm^{-3}}$, the NSE region extends to $\sim 0.45\,{\rm M_\odot}$. The SN simulations started from this progenitor condition. The structure of the core is well approximated by a spherical model.

When transferring the progenitor model of e8.8 to the SN simulations, the mass of the ONeMg-core was reduced to $1.34\,{\rm M_\odot}$ in the course of providing an easy-to-handle fit to the complex density structure. This has no relevant influence on the dynamical evolution of the explosion, as can be concluded from the close similarity of the explosion behavior of model e8.8 with that of a previous version of the progenitor (Nomoto 1984; Nomoto 1987; K. Nomoto, 2008, private communication), which is commonly termed e8.8 in the literature and e8.8$_{\rm n}$ in this publication. Model e8.8$_{\rm n}$ had a degenerate core of $1.375\,{\rm M_\odot}$, but a smaller hydrogen envelope (see Figure 1). It is a reference case for simulations of ECSNe and was used in various studies, focusing on explosion properties (Kitaura et al. 2006; Fischer et al. 2010), nucleosynthesis (Janka et al. 2008; Wanajo et al. 2011; Wanajo et al. 2018), effects of microphysics (Hüdepohl et al. 2010; von Groote 2014; Radice et al. 2017), and PNS kicks (Gessner & Janka 2018). In order to compensate for possible uncertainties in our ECSN simulations with the new progenitor model of e8.8, we vary its explosion energy in a set of 2D simulations, denoted by e8.8$_3$, e8.8$_6$, e8.8$_{10}$, and e8.8$_{15}$ for $E_{\rm exp} = (3, 6, 10, 15) \times 10^{49}$ erg.

Progenitor model e8.8 has the very sharp density gradient at $1.34\,{\rm M_\odot}$ near the edge of its compact ONeMg-core ($\xi_{2.5} = 5.7 \times 10^{-6}$, $\xi_{1.5} = 8.0 \times 10^{-6}$)[1] that is characteristic of such progenitors prior to the onset of core collapse. This steep gradient is a prominent feature of the density (ρ) profile in Figure 1. In the same same figure we also show the ρr^3-profile as well as the electron fraction Y_e and the temperature T. All of these quantities are displayed as functions of enclosed mass and radius. The inner $\sim 0.45\,{\rm M_\odot}$ of the degenerate core contain iron-group nuclei and α-particles in NSE. The dash-dotted, dashed, and dotted lines indicate the positions of the NSE/ONeMg, CO/He, and He/H composition interfaces, respectively. We define the locations of the composition interfaces,

---

[1] Because the core structure of higher-mass progenitors can be characterized by the compactness parameter $\xi_M \equiv \frac{M/{\rm M_\odot}}{R(M_{\rm bary}=M)/10^3\,{\rm km}}$ (O'Connor & Ott 2011), we provide values for this quantity here. However, due to the steep density gradient outside of the core in the considered progenitors, the value of this parameter in the context of our work is limited.
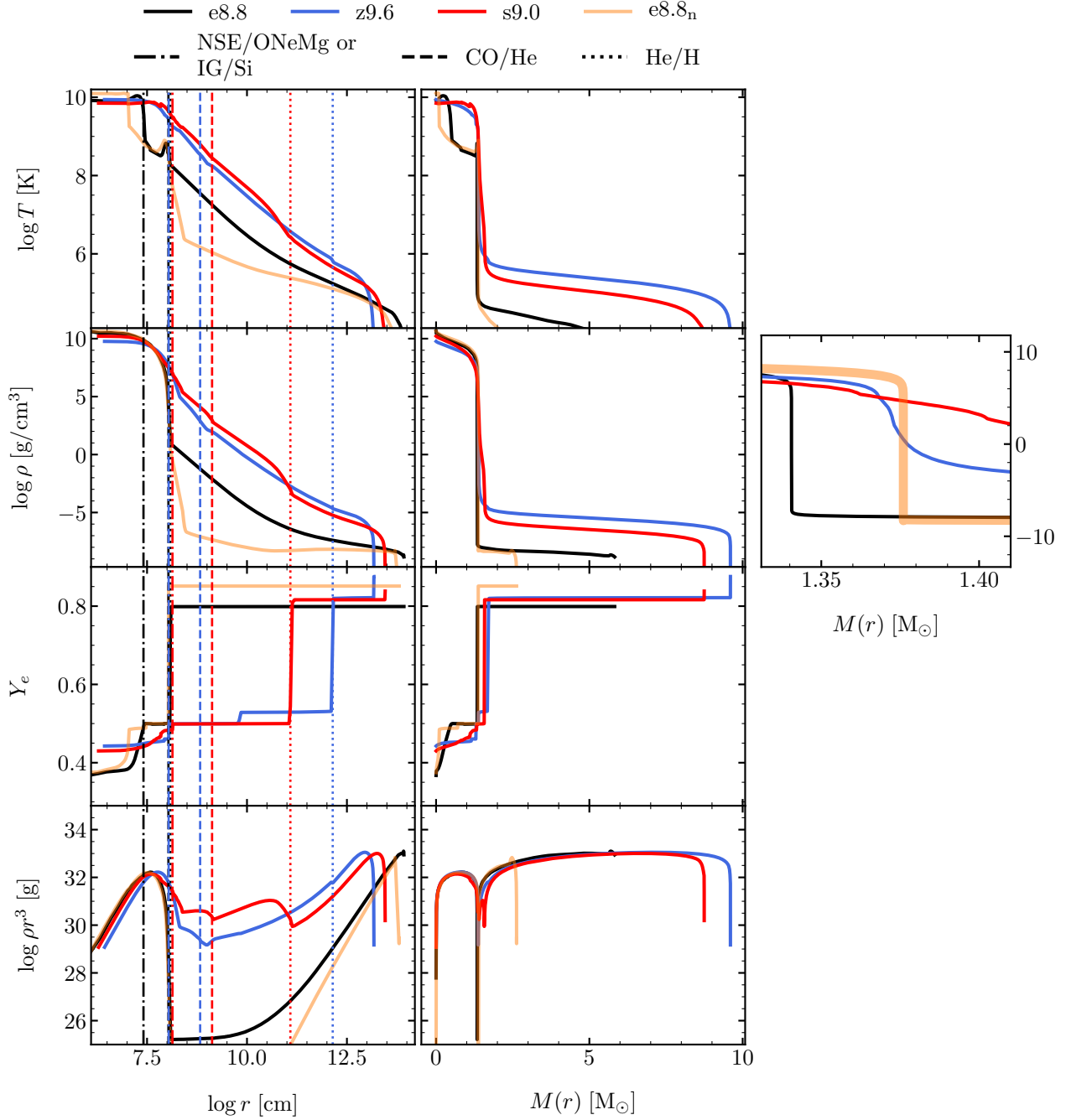
Figure 1. Profiles of the temperature (T), density (ρ), electron fraction (Y_e) and ρr^3 for the pre-collapse progenitor models as functions of radial coordinate (left panels) and mass coordinate (right panels). Indicated by dash-dotted, dashed, and dotted lines are the outer boundaries of the degenerate (iron or NSE), CO, and He cores, respectively. Note the huge differences in the density and ρr^3-profiles between the progenitors with iron and ONeMg-cores, in particular just outside of the CO core. We show the difference in the core structures of our ONeMg-core models in a zoom of the ρ vs. $M(r)$ profiles in the rightmost panel.

similar to Wongwathanarat et al. (2015), as those positions at the bottom of the respective layers of the star where the mass fractions X_i drop below half of their maximum values in the layer. The radial positions of the composition interfaces are summarized in Table 1. In the top panel of Figure 2 we present the composition of model e8.8, where we combine all elements with mass numbers greater than 28 into "iron-group" (IG) material or nuclei in NSE.

The ONeMg-core is surrounded by very thin carbon and helium shells ($M_C \approx 8.1 \times 10^{-3}\,M_\odot$, $M_{He} \sim 2.1 \times 10^{-6}\,M_\odot$) and a hydrogen (H+He) envelope ($M_H \approx 4.49\,M_\odot$). The total masses of the different nuclei present in the entire pre-SN model are listed in Table 5.

For collapse and post-bounce evolution of an ONeMg-core progenitor we employ in all of this paper the new progenitor model e8.8 in 1D, 2D, and 3D simulations with the PROMETHEUS-HOTB
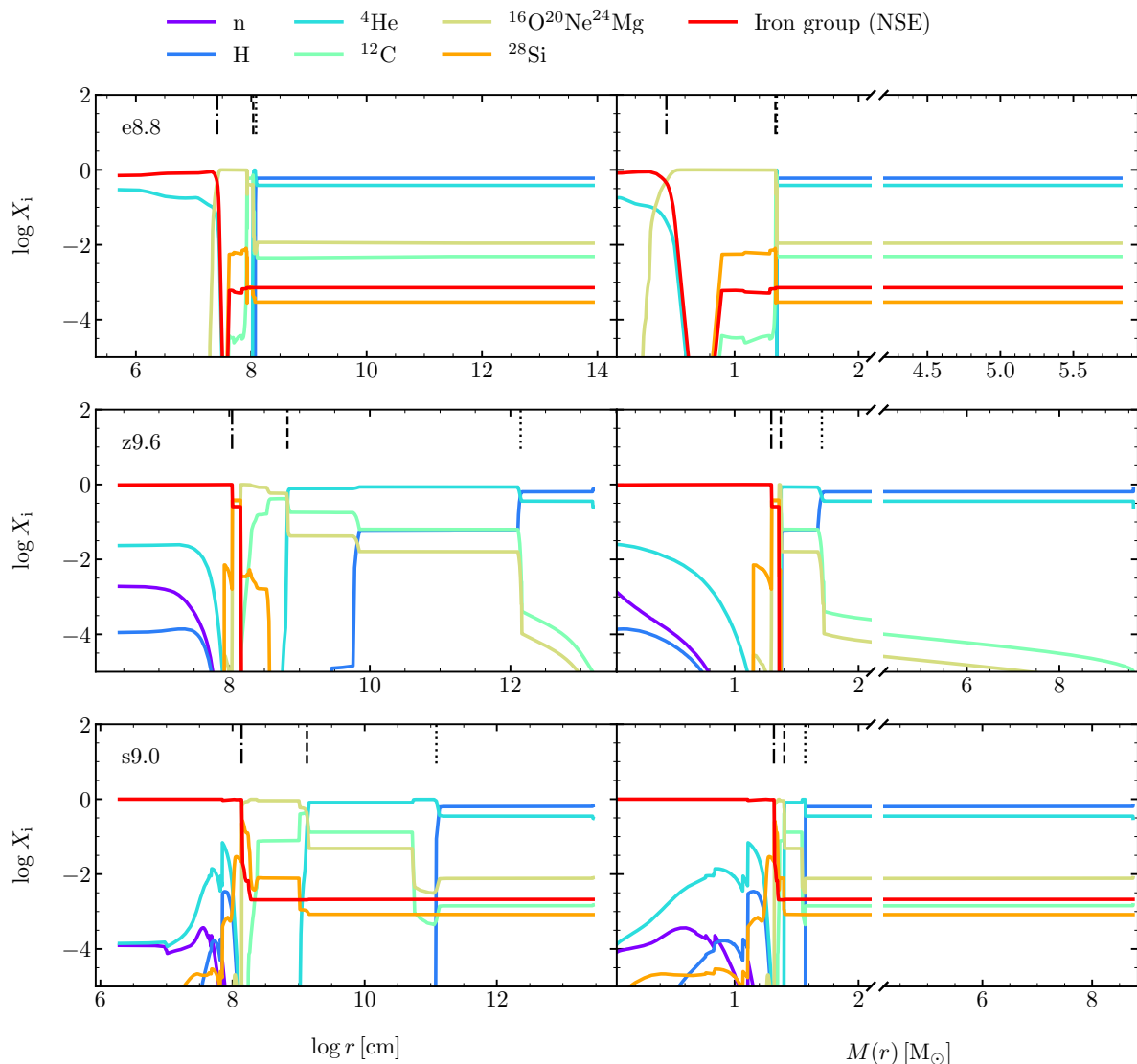
Figure 2. Pre-collapse composition of models e8.8 (top), z9.6 (middle) and s9.0 (bottom) as a function of radius (left) and enclosed mass (right). Note the broken horizontal axis of the right panels. We combine all chemical elements with mass numbers greater than 28 into the "iron-group" (IG). The dash-dotted, dashed, and dotted lines indicate the outer boundaries of degenerate (iron or NSE), CO, and He cores, respectively.

code as detailed in Section 3.4. The profile of the old progenitor e8.8$_n$ is shown in Figure 1 merely for illustration and reference.

2.2 Fe-core progenitors

As a second progenitor we employ a zero-metallicity $M_{ZAMS} = 9.6\,M_\odot$ star, termed z9.6. It was first used by Janka et al. (2012) and was also considered in other studies such as Müller et al. (2013); Radice et al. (2017); Müller et al. (2019). This iron core progenitor is structurally similar to the ECSN model. It also shows a sharp decline of the density at the edge of its iron core, enabling low-energy explosions in 1D (Melson et al. 2015a; Radice et al. 2017). Evolved by A. Heger (2012, private communication) as an extension to Heger & Woosley (2010), the pre-SN model develops an iron core of about $1.30\,M_\odot$. The iron core is surrounded by a $0.061\,M_\odot$ Si-layer, a $0.016\,M_\odot$ CO-layer, and has a hydrogen-free helium layer of about $0.004\,M_\odot$ below a $0.33\,M_\odot$ convective H/He-

layer with a hydrogen mass fraction of $\sim 6\%$, which is surrounded by a massive hydrogen envelope of nearly $8\,M_\odot$ ($\xi_{2.5} = 7.66 \times 10^{-5}$, $\xi_{1.5} = 2.38 \times 10^{-4}$). The H/He-layer is in the process of extended, but incomplete, 2nd dredge-up of the He-layer that is typical for AGB/sAGB stars and those at the low-mass end of the CCSN domain. The star is basically an iron-core AGB star, maybe should be called a hyper-AGB (hAGB) star.

As the envelope is not rich of metals, mass loss is expected to play only a negligible role during the star's evolution. This leaves the total mass of the star almost unchanged (see Table 1). Due to its structure it was one of the first iron-core progenitors that exploded in fully self-consistent 3D simulations by Melson et al. (2015a) with VERTEX-PROMETHEUS and was also investigated by Radice et al. (2017) and Müller et al. (2019). The result of Melson et al. (2015a) provides the initial state for our investigation.

Moreover, we investigate a solar-metallicity $M_{ZAMS} = 9.0\,M_\odot$ star, termed s9.0, of Sukhbold et al. (2016). Its $1.30\,M_\odot$ iron

Table 1. Shell structure of the pre-collapse progenitor models.

Model	Interface	R_{shell} [cm]	M_{shell} [$M_\odot$]	$t_{\text{sh,max}}^{\text{3D}}$ [s]	E_{bind} [10^{49} erg]
	NSE/ONeMg	2.57×10^7	0.45	-	
	ONeMg/C	8.48×10^7	1.33	0.19	$E_{\text{bind}}(m > M_{\text{map}}) = -5.99$
e8.8	C/He	1.09×10^8	1.34	0.20	
	He/H	1.21×10^8	1.34	0.21	
	Surface	8.43×10^{13}	5.83	4.1×10^5	
	IG/Si	1.10×10^8	1.30	0.09	
	Si/CO	1.45×10^8	1.36	0.11	$E_{\text{bind}}(m > M_{\text{map}}) = -5.82$
	CO/He	6.48×10^8	1.37	0.40	
z9.6	He/H (H<1%)	6.24×10^9	1.38	2.64	
	He/H (H<10%)	1.40×10^{12}	1.70	1.8×10^3	
	Surface	1.50×10^{13}	9.60	1.1×10^5	
	IG/Si	1.24×10^8	1.30	0.08	
	Si/CO	1.55×10^8	1.33	0.30	$E_{\text{bind}}(m > M_{\text{map}}) = -2.63$
s9.0	CO/He	1.34×10^9	1.40	1.30	
	He/H	1.22×10^{11}	1.57	124.0	
	Surface	2.86×10^{13}	8.75	1.8×10^5	

Notes: The radii of the composition interfaces, R_{shell}, are defined as those positions at the bottom of the stellar layers (e.g. CO) where the mass fractions (e.g. C+O) drop below half of their maximum values in the respective layer. Progenitor model z9.6 is in the process of deep 2nd dredge-up with hydrogen reaching basically to the bottom of the former helium layer; hence two values are provided for the He/H interface. In all Figures we refer to the "high" value, since it is often used also in other context, e.g., for the "α-parameter" in common-envelope (CE) studies. We also show the mass M_{shell} contained within the corresponding radius and the post-bounce time when the outermost radius of the forward shock of our 3D models reaches the interface. E_{bind} is the binding (i.e., internal + kinetic + potential) energy in the progenitor star outside of M_{map}, which is the location of the final mass cut. For values see Table 3.

core is surrounded by a silicon shell of $0.03\,M_\odot$, a carbon-oxygen layer of $0.068\,M_\odot$, and a helium shell of $0.169\,M_\odot$ (see Table 1). The hydrogen envelope extends from $1.57\,M_\odot$ up to $8.75\,M_\odot$ ($\xi_{2.5} = 3.83 \times 10^{-5}$, $\xi_{1.5} = 5.24 \times 10^{-3}$). In comparison to model z9.6, model s9.0 is just slightly less evolved on its track to 2nd dredge-up of the He core, however, the convection is better driven by the iron-peak opacity from the outside-in. The s9.0 progenitor was chosen to be representative for low-mass CCSNe by Jerkstrand et al. (2018), who studied the late-time nebular spectra of the supernova (SN), by Glas et al. (2019a) focusing on the neutrino emission during the explosion, and by Burrows et al. (2019) in a large set of 3D simulations. The three-dimensional exploding model for our investigation is provided by Melson et al. (2020) and has also been modeled with Vertex-Prometheus.

Although the progenitors considered in this study have very similar ZAMS masses, their pre-collapse core structures differ significantly (see Figure 1). We stress that the ρr^3-profiles of the progenitors are decisive for the long-time evolution of the explosion (Kifonidis et al. 2003; Wongwathanarat et al. 2015). The behavior of the ρr^3-profile yields important information on the propagation of the shock through the stellar structure, because, according to Sedov et al. (1961), positive gradients of ρr^3 cause shock deceleration, whereas negative gradients cause the opposite. Additionally, variations of the shock velocity produce crossing pressure and density gradients behind the shock front near the composition-shell interfaces (Chevalier & Klein 1978). Such conditions are essential for RT instabilities as detailed in Section 5.1, assigning them a crucial role for explaining high-velocity metal-rich ejecta and radial mixing of heavy elements (e.g., Arnett et al. 1989a; Nomoto et al. 1990; Wongwathanarat et al. 2015).

The ECSN progenitor exhibits an extremely sharp drop of the ρr^3-profile just outside of the ONeMg-core. It is this drop in density that enables fast explosions due to an early, rapid decline of the mass accretion rate and of the corresponding ram pressure

at the SN shock (Kitaura et al. 2006). Outside of the core, the ρr^3-profile grows monotonically as no other composition interfaces are encountered. The z9.6 progenitor falls into the class of ECSN-like progenitors also in this respect: Similar to the electron-capture progenitor, the z9.6 model shows a monotonic growth of the ρr^3-profile exterior to the CO core, where only a small step in the density profile can be seen at the He/H interface. Model s9.0 on the other hand exhibits strong variations in its ρr^3-profile. Each interface of different composition layers is accompanied by a negative ρr^3-gradient close to the interface. Of particular interest are the CO/He and He/H interfaces. These interfaces have an impact on the long-time evolution of the explosion as will be discussed in Section 5.1.

For this paper we performed spherically symmetric (1D), axisymmetric (2D) and fully three-dimensional (3D) simulations for all progenitors beyond the moment when the shock reaches the surface of the star. The different setups and approaches for these simulations will be described in the following section.

3 NUMERICAL METHODS AND PHYSICAL SETUP

In order to cover collapse, shock revival, and shock propagation through the envelope and circumstellar material we employ a step-wise approach. Core collapse, bounce, and post-bounce evolution until the explosion is well on its way, i.e., the neutrino-dominated phases of the first second(s) around and after core bounce, of the iron-core progenitors are simulated with the VERTEX-PROMETHEUS code. The corresponding long-time simulations covering the shock propagation through the star, after the onset of the explosion until and beyond shock breakout, are conducted with the PROMETHEUS-HOTB code. The explosion of the ECSN progenitor is simulated entirely with PROMETHEUS-HOTB.[2]

In the following sections we describe the numerical and physical features of the codes and the setups applied during the different stages of the evolution.

3.1 VERTEX-PROMETHEUS code

VERTEX-PROMETHEUS is a hydrodynamics code based on an implementation of the Piecewise Parabolic Method (PPM) of Colella & Woodward (1984), coupled with a three-flavor, energy-dependent, ray-by-ray-plus (RbR+) neutrino transport scheme that iteratively solves the neutrino energy and momentum equations with a closure determined from a tangent-ray Boltzmann solver (Rampp & Janka 2002). It employs the full set of neutrino reactions and microphysics presented in Buras et al. (2006) and the high-density equation of state (EoS) of Lattimer & Swesty (1991) with a nuclear incompressibility of $K = 220$ MeV. At low densities ($\rho \leq \rho_{HD} = 10^{11}$ g/cm^3) VERTEX-PROMETHEUS uses the EoS of Janka & Müller (1995), which includes the contributions of photons, arbitrarily degenerate and arbitrarily relativistic e^+/e^-, and non-degenerate, non-relativistic nucleons and nuclei. The relative abundances of 23 nuclear species (including some neutron-rich nuclei) are determined by an NSE solver in regions with temperatures above T_{NSE}. Below T_{NSE} a flashing scheme is used to approximately treat nuclear burning (see Rampp & Janka 2002). For unshocked, collapsing stellar matter we choose $T_{NSE} = 0.5$ MeV, and for neutrino-heated postshock matter we take $T_{NSE} = 0.5$ MeV for the simulation of model z9.6 and $T_{NSE} = 0.34$ MeV for model s9.0.[3]

The simulations presented here are performed with a 1D gravitational potential including general relativistic corrections, Case A of Marek et al. (2006). The neutrino transport solver contains corrections for general relativistic redshift and time dilation effects. VERTEX-PROMETHEUS makes use of the axis-free Yin-Yang grid (Kageyama & Sato 2004) based on the implementation of Melson (2016).

3.2 PROMETHEUS-HOTB code

PROMETHEUS-HOTB is based on the same hydrodynamics module as VERTEX-PROMETHEUS and uses the implementation of the Yin-Yang grid presented in Wongwathanarat et al. (2010a). It employs the EoS of Lattimer & Swesty (1991) for high densities above a threshold value ρ_{HD} (usually 10^{11} g/cm^3) and the "Helmholtz" EoS of Timmes & Arnett (1999) for densities below ρ_{HD}, which takes into account arbitrarily degenerate and relativistic electrons and positrons, photons, and a set of non-degenerate, non-relativistic nuclei. The set of nuclei consists of neutrons n, protons p, 13 α-nuclei (^{4}He, ^{12}C, ^{16}O, ^{20}Ne, ^{24}Mg, ^{28}Si, ^{32}S, ^{36}Ar, ^{40}Ca, ^{44}Ti, ^{48}Cr, ^{52}Fe, ^{56}Ni), and an additional tracer nucleus Tr, which tracks the production of neutron-rich nuclei and replaces ^{56}Ni in environments with low electron fraction, $Y_e < 0.49$. These nuclear species are described as non-relativistic Boltzmann gases. The advection of the species is treated with the Consistent Multi-fluid Advection (CMA) scheme of Plewa & Müller (1999). NSE is assumed above $T_{NSE} = 9 \times 10^9$ K and accounted for by an NSE table including the nuclei listed above (Kifonidis 2004, private communication). Nuclear burning is considered at temperatures below T_{NSE} with a 13-species α-network, which is consistently coupled to the hydrodynamic modeling. At the boundary between network and NSE we assume that all free neutrons and protons recombine to yield ^{4}He. We thus add the mass fractions of p and n onto the mass fraction of ^{4}He, accounting for the corresponding energy release[4]. The PROMETHEUS-HOTB code uses a 3D gravitational potential with the general-relativistic (GR) monopole correction of Marek et al. (2006) as discussed by Arcones et al. (2007), while higher multipoles are obtained from a solution of Poisson's equation as described in Müller & Steinmetz (1995).

Different from VERTEX-PROMETHEUS, PROMETHEUS-HOTB uses a three-flavor grey neutrino transport scheme as presented in Scheck et al. (2006),[5] which is applicable at low and moderate optical depths. Therefore, the high-density core of the PNS, with a mass of $M_c = 1.1$ M$_\odot$ and densities well above those of the neutrinospheric layer, is replaced by a closed (Lagrangian) inner grid boundary at radius R_{ib}. The excised 1.1 M$_\odot$ PNS core is taken into account in the gravitational potential as a central point mass. The contraction of the PNS is mimicked by an inward movement of the boundary radius R_{ib}, whose motion is followed by all grid points in the computational domain. We use the contraction of R_{ib} as prescribed by Ertl et al. (2016). The time-dependent neutrino luminosities at R_{ib} are imposed as boundary conditions as provided by an analytic one-zone cooling model following Ugliano et al. (2012), Sukhbold et al. (2016), Ertl et al. (2016), and Ertl et al. (2020). This time-dependent treatment of the central-core region employs five parameters (p, a, $R_{c,f}$, t_0, $R_{ib,f}$; see Appendix A for definitions), which can be calibrated to yield explosions that fulfill the constraints set by observed SNe or by fully self-consistent 3D simulations of CCSNe. The reader is referred to Appendix A for a more detailed description of the parametric approach and to Table 2 for the parameters of the core model employed in our work.

3.3 Collapse and post-bounce setup in VERTEX-PROMETHEUS

The collapse of the iron core progenitors is computed in 1D using the full set of neutrino interactions until 10 ms after bounce. Thereafter,

---

[2] The reason for these different treatments is mainly technical: The VERTEX-PROMETHEUS version used for ONeMg core collapse by Kitaura et al. (2006); Janka et al. (2008), and Hüdepohl et al. (2010) has not yet been updated with the 3D developments and parallelisation optimization applied to the version used for Fe-core collapse. However, for suitable choices of parameter values, the explosion dynamics of ECSNe computed with PROMETHEUS-HOTB is very similar to the fully self-consistent 2D VERTEX-PROMETHEUS and CoCoNuT-VERTEX explosion models discussed by Janka et al. (2008) and Janka et al. (2012), respectively.

[3] VERTEX-PROMETHEUS does not apply a nuclear network for $T < T_{NSE}$. The choice of a lower value of T_{NSE} permits us to follow the ejection of mass through neutrino heating for a longer time period in model s9.0, where the expansion velocity of the expelled matter is smaller than in z9.6, thus facilitating nucleon recombination to α particles and heavy nuclei.

[4] In a newer version of the code we allow only paired free neutrons and protons to recombine to ^{4}He, thus also satisfying charge conservation.

[5] Some improvements to the neutrino transport module are described in Appendix B.

Table 2. Summary of the PNS core parameter values used for the e8.8 model and resulting explosion energies from 1D simulations. Definitions of these parameters in the context of our modeling approach are given in Appendix A. The explosion energy is essentially independent of dimensionality (1D, 2D, 3D).

Model	E_{exp} [foe]	p [index]	a [factor]	$R_{c,f}$ [km]	t_0 [s]	$R_{ib,f}$ [km]
e8.8$_3$	0.03	-3	1.0×10^{-2}	27	0.1	40
e8.8$_6$	0.06	-3	1.2×10^{-2}	22	0.1	40
e8.8$_{10}$	0.10	-3	4.0×10^{-1}	20	0.1	40
e8.8$_{15}$	0.15	-3	5.8×10^{-1}	18	0.1	40

the simulations are mapped onto the three-dimensional Yin-Yang grid and random cell-to-cell density perturbations are imposed with an amplitude of 0.1%. The simulations employ a non-equidistant radial grid with initially 400 zones extending to 10^9 cm, which is refined in steps to more than 600 zones. This guarantees a resolution $\Delta r/r$ of better than 1% at the gain radius. The innermost 1.6 km are calculated in spherical symmetry to avoid time stepping constraints at the grid center. The angular resolution of the z9.6 model is $2°$. The post-bounce evolution of model s9.0 is computed with a newly implemented static mesh refinement (SMR) scheme presented in Melson et al. (2020), which increases the angular resolution to $1°$ outside of the gain radius and to $0.5°$ exterior to a radius of 160 km.

The simulations with full neutrino transport are too expensive to continue them to late post-bounce times. At $t_{pb} \gtrsim 0.5$ s the neutrino transport is therefore switched off and replaced by a simplified scheme for neutrino heating and cooling, which ensures an essentially seamless continuation with a minimum of transient artifacts. Details of this scheme are given in Appendix E. During this phase of simplified neutrino treatment both model z9.6 and s9.0 are simulated with uniform angular resolution of $2°$.

3.4 Collapse and post-bounce setup in PROMETHEUS-HOTB

During the spherically symmetric simulation of the collapse up to core bounce, PROMETHEUS-HOTB uses the parametrized deleptonization scheme described in Liebendörfer (2005). The necessary $Y_e(\rho)$-trajectory was provided by Hüdepohl (2018, private communication) from his core-collapse simulations of the ONeMg-core progenitor e8.8$_n$ with VERTEX-PROMETHEUS.

For the simulation of the ECSNe progenitor we take $\rho_{HD} = 10^{11}$ g cm^{-3} and assume NSE in regions where the temperature exceeds $T_{NSE} = 9 \times 10^9$ K and apply the α-network for temperatures lower than this value. After bounce PROMETHEUS-HOTB employs the grey neutrino transport scheme and modeling approach as presented in Scheck et al. (2006). Thus, the neutrino-opaque central core of the PNS is excised from the computational domain and replaced by the analytic core model of Ugliano et al. (2012). In Table 2 we list the parameter values of the PNS core model used for a set of simulations of model e8.8. We perform 1D and 2D simulations for all four sets of parameter values and choose the e8.8$_{10}$ calibration as our reference case for a 3D simulation. The 1D and 2D simulations possess a non-equidistant radial grid with 2000 zones up to a radius of $R_{ob} = 2 \times 10^{10}$ cm. The 3D run has only 1400 radial zones for computational efficiency. The multi-dimensional simulations are conducted with an angular resolution of $2°$, and the 3D simulation makes use of the Yin-Yang grid. We restrict ourselves to a 1D gravitational potential with GR corrections (Arcones et al. 2007) because the explosions of model e8.8 are nearly spherical.

3.5 Setup for the long-time simulations

The simulations of the long-time evolution of all models are computed with PROMETHEUS-HOTB. For this we map the final state of a post-bounce simulation at time t_{map} onto a new computational grid within PROMETHEUS-HOTB, similar to the procedure described in Wongwathanarat et al. (2015). We also add the low-density extensions to the Helmholtz EoS described therein. In Table 3 we list the times of mapping and the inner and outer radii of the new computational domain, R_{ib} and R_{ob}, respectively. The mass contained within R_{ib} is treated as a point mass[6] and is called M_{map}.

The time t_{map} is chosen such that the explosion energy has effectively converged to its asymptotic value and a neutrino-driven wind region has developed around the PNS, where the outflow is essentially spherical and reaches supersonic velocity.

All long-time simulations are computed with an angular resolution of $2°$. We use a non-equidistant (geometrically increasing) radial grid from the inner to the outer boundary. In order to guarantee sufficient resolution where needed, the radial grid is allowed to move with the ejecta starting from $t_{pb} \sim 10$ s. Gravity is accounted for by a 1D GR-corrected potential and nuclear reactions are still considered. When mapping the iron core models, z9.6 and e9.0, into PROMETHEUS-HOTB, we recombine free n and p from the freeze-out of NSE into ^{4}He under the condition of charge conservation and account for the energy release. Moreover, we combine all neutron-rich nuclei formed in neutrino-heated ejecta into tracer (Tr) material.

When mapping from the simulations of the onset of the explosion to the follow-up simulations, the central region interior to R_{ib} (Table 3) is removed from the computational domain. Similar to Wongwathanarat et al. (2015) we prescribe an inflow boundary condition at R_{ib}, which corresponds to the neutrino-driven baryonic mass-loss ("neutrino-wind"; e.g Qian & Woosley 1996) generated by ongoing neutrino-energy deposition in the surface layers of the cooling PNS. In contrast to Wongwathanarat et al. (2015), we employ neutrino-wind results adopted from 1D simulations of the explosions, seamlessly connected to the fully multi-dimensional explosion simulations by choosing R_{ib} to be in the supersonic wind region (ensuring that perturbations cannot propagate back to the inner boundary creating artifacts) and by applying the wind data at times when the outflow properties match closely between the 1D and the (angle-averaged) multi-dimensional models. This is possible because the PNSs in 1D and multi-dimensional models are extremely similar and the neutrino-emission and thus the neutrino-driven winds also have very similar properties. For the long-time run of model z9.6, we therefore employ neutrino-wind conditions of a 1D simulation of this model with the VERTEX-PROMETHEUS code. This model treats PNS convection with an approach based on mixing-length theory and exhibits neutrino-emission properties that are hardly distinguishable from the multi-dimensional calculation (Mirizzi et al. 2016, see). The time dependence of the radial velocity v_r, density ρ, and total (i.e. kinetic + internal) energy density e, which are needed for setting the boundary condition, are shown in Figure 3 (solid lines) as extracted from the 1D explosion simulation of the z9.6 model at a radius of 600 km (in the supersonic wind domain). For the 3D simulation of model e8.8 we use the neutrino-wind results from the corresponding 1D run with the same explosion energy (see dashed lines in Figure 3), whereas we do not impose a wind boundary condition in the long-time simulation of

---

[6] We ensure that matter at radii smaller than R_{ib} has velocities smaller than the local escape velocity and will thus eventually contribute the to final NS mass.
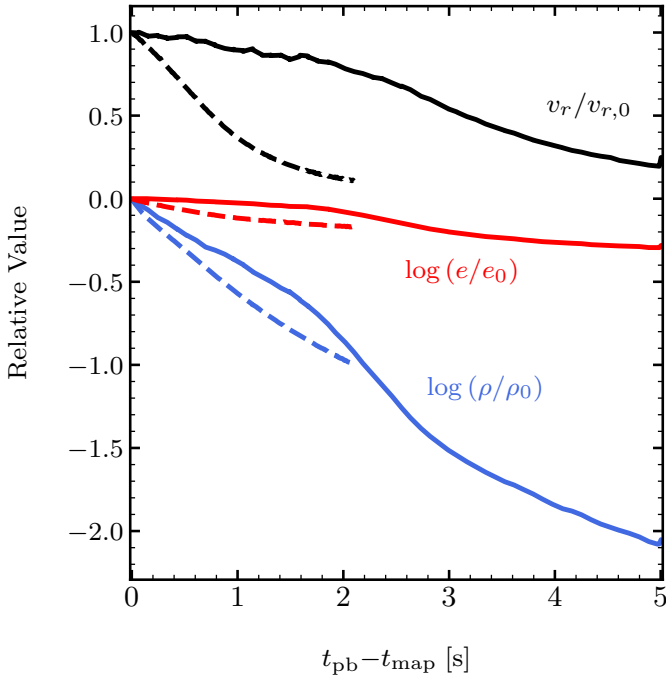
Figure 3. Time-dependent behavior of neutrino-wind density ρ, radial velocity v_r, and total energy density e, normalized to their initial values at t_{map} (see Table 3), which defines the start of the long-time simulations of model e8.8 and z9.6. The data for model z9.6 are extracted from a 1D simulation of the explosion of the $9.6\,M_\odot$ progenitor with VERTEX-PROMETHEUS (see Mirizzi et al. 2016), evaluated at a radius of 600 km (solid lines). For model e8.8 we use data of the respective 1D simulation with PROMETHEUS-HOTB (dashed lines).

Table 3. Initial positions of inner (R_{ib}) and outer (R_{ob}) grid boundaries, baryonic mass contained within the inner boundary (M_{map}) and mapping times t_{map} in seconds after bounce for our long-time simulations.

Model	Dim.	R_{ib} [km]	R_{ob} [km]	M_{map} [M$_\odot$]	t_{map} [s]
e8.8$_3$	2D	1000	8.4×10^8	1.334	2.515
e8.8$_6$	2D	1000	8.4×10^8	1.327	2.515
e8.8$_{10}$	2D	1000	8.4×10^8	1.319	2.515
e8.8$_{15}$	2D	1000	8.4×10^8	1.309	2.515
e8.8	3D	500	8.4×10^8	1.326	0.470
z9.6	3D	600	1.5×10^8	1.353	1.440
s9.0	3D	1000	2.9×10^8	1.351	3.140

model s9.0, since the neutrino-driven wind in this model is already very weak at the time of mapping. Using time dependences of the boundary conditions normalized by the initial value at the mapping time t_{map} guarantees a smooth, seamless transition from the earlier evolution to the long-time evolution of the explosion. Transient artifacts are thus kept minimal.

Additionally, for the long-time simulations we include the decay of radioactive nickel, which becomes a relevant source of energy during late phases of the explosion. Radioactive ^{56}Ni (half-life $t_{1/2} = 6.077$ days) decays to ^{56}Co via electron capture (EC) decay. The resulting ^{56}Co nucleus is unstable ($t_{1/2} = 77.23$ days) and decays to ^{56}Fe by means of electron capture and via positron decay (β^+). We thus add ^{56}Co and ^{56}Fe to our set of nuclei. The respective

decay reactions are given by

$$\text{EC}: \quad e^- + {}^{56}_{28}\text{Ni} \rightarrow {}^{56}_{27}\text{Co} + \nu_e + \gamma,$$

$$\text{EC}: \quad e^- + {}^{56}_{27}\text{Co} \rightarrow {}^{56}_{26}\text{Fe} + \nu_e + \gamma \quad (81\%),$$

$$\beta^+: \quad {}^{56}_{27}\text{Co} \rightarrow {}^{56}_{26}\text{Fe} + e^+ + \nu_e + \gamma \quad (19\%).$$
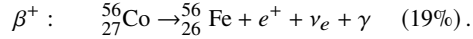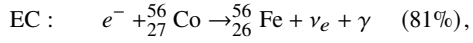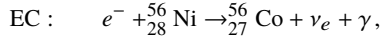
The above reactions provide an energy source for the surrounding plasma in the form of gamma radiation (E_γ) and kinetic energy (E_{kin,e^+}) of the positrons that are produced in the β^+ decays. We include the annihilation energy of the positrons with electrons (E_{ann}) in E_γ. The produced neutrinos escape freely. The average energy available (including the kinetic energy of the positron in the cobalt decay) per decay is $E_{\gamma,\mathrm{Ni}} = 1.72$ MeV, $E_{\gamma,\mathrm{Co}} = 3.735$ MeV (Nadyozhin 1994). A fraction of the γ's may escape depending on the (radial) optical depth $\tau(r)$ of the gas up to the stellar surface at radius R_*. This optical depth is defined as

$$\tau(r) = -\int_{R_*}^r \kappa_\gamma Y_e(r')\rho(r')\,\mathrm{d}r', \tag{1}$$

where Y_e the electron fraction and κ_γ the optical opacity. In the practical application the integral boundary r in Equation (1) is the radial location of a considered grid cell, and we assume that the trapped fraction of the locally produced γ radiation, $(1 - \exp[-\tau(r)])$, deposits its energy locally in the same cell of the computational grid. Assuming Compton-scattering is the dominant opacity source, we adopt a constant value of $\kappa_\gamma = 6.0 \times 10^{-2}$ cm^2 g^{-1} (Swartz et al. 1995). Therefore, the energy per mass $\Delta E_i / \Delta M$ deposited by each species i, with mass fraction X_i and nuclear mass m_i, into the surrounding plasma during a time step Δt is given by

$$\frac{\Delta E_i}{\Delta M} = \frac{\Delta X_i}{m_i}\left[E_\gamma\left(1 - \mathrm{e}^{-\tau(r)}\right) + E_{\mathrm{kin},e^+}\right], \tag{2}$$

where $\Delta X_i = \left(1 - \mathrm{e}^{-\Delta t/t_{0,i}}\right)$ is the change of X_i during Δt with $t_{0,i} = t_{1/2,i}(\ln(2))^{-1}$ being the life-time of species i, and E_{kin,e^+} is the kinetic energy of the positron in the cobalt decay. The energy is assumed to be deposited locally, and thermodynamic quantities are self-consistently updated.

4 EVOLUTION DURING THE FIRST SECONDS

4.1 Shock propagation and explosion energetics

In the following we provide a brief overview of the most important features of the early post-bounce evolution in the 3D simulations of models e8.8, z9.6, and s9.0. The reader is referred to Melson et al. (2015a) and Melson et al. (2020) for a detailed analysis of the post-bounce phase of the iron-core progenitors in VERTEX-PROMETHEUS simulations. Generic properties of the explosion of ECSNe are given in Kitaura et al. (2006); Janka et al. (2008); Hüdepohl et al. (2010); Fischer et al. (2010); Radice et al. (2017); Gessner & Janka (2018). The dynamics of our simulations for the 8.8 $M_\odot$ progenitor closely resemble these previous findings. In Figure 4 we show the evolution of the angle-averaged radius of the SN shock and the diagnostic explosion energy of our three-dimensional simulations during the first three seconds after bounce. The angle-averaged shock radius is calculated as

$$\langle R_{sh}\rangle = \frac{1}{4\pi}\int R_{sh}(\theta, \phi)\mathrm{d}\Omega, \tag{3}$$

where $\mathrm{d}\Omega = \sin\theta\mathrm{d}\theta\mathrm{d}\phi$. The diagnostic explosion energy at all times is given by the integral of the total (i.e., kinetic plus internal plus gravitational) energy density in the postshock region, defined as

$e_b = e_{int} + e_{kin} + e_{grav}$, over volume elements where it has a positive value

$$E_{exp} = \int_{V_{postshock}(e_b > 0)} dV \, e_b . \tag{4}$$

The sharp drop in density outside of the ONeMg-core in model e8.8 leads to an early and strong decrease of the accretion rate and hence ram pressure at the shock. Consequently, the SN shock expands rapidly and reaches the core/envelope boundary ($R_{He/H} = 1210$ km), at 0.21 s after core bounce. This is in stark contrast to the typical CCSN, where the high ram pressure stalls the shock expansion at a small radius for several 100 ms. The explosion energy starts rising steeply, fuelled by the onset of a neutrino-driven wind, as soon as the shock leaves the ONeMg-core.

The acceleration of the shock at the core/envelope boundary is followed by a drastic switch to deceleration after the shock passes the lower boundary of the H-envelope (see upper right panel of Figure 4). This is caused by a sudden change of the density gradient at the core/envelope transition. Consequently, the neutrino-heated ejecta pile up in a dense, compressed and decelerated shell behind the SN shock.

The ECSN-like structure of model z9.6 is reflected in the evolution of the SN shock front and in the growth of the diagnostic explosion energy. The shock radii remain almost perfectly spherical in both the e8.8 and z9.6 models. The acceleration of the blast wave outside of the iron core, however, ends earlier in model z9.6 than in model e8.8 because of the more gradual changes in the density profile. In both cases the explosion energies also start to rise early and saturate just after $t_{pb} \sim 1$ s.

In contrast to the z9.6 and e8.8 models, model s9.0 lacks the very steep density gradient at the edge of the Fe-core, as can be seen in Figure 1. The shock can expand initially up to 180 km at $t_{pb} \sim 130$ ms, but then it enters a phase of recession. The arrival of the Si/O interface at the shock and the decreasing mass-accretion rate within the oxygen shell eventually lead to shock expansion at ~0.32 s after bounce. Shock expansion is aided by strong convection behind the shock front (see also Melson et al. 2020). Similar to the results presented in Glas et al. (2019a), who used the same progenitor, the model remains convection-dominated and does not exhibit any sign of the oscillatory growth of the SASI (Blondin et al. 2003; Foglizzo et al. 2007). However, although SASI does not develop in the simulation, the forward shock experiences large-scale deformation with a dipole amplitude of ~10% (compared to the angle-averaged shock radius). This deformation is driven by big plumes that form in the post-shock layer. Contrary to the ECSN-like models, strong anisotropic, non-radial mass flows persist around the PNS during several seconds after bounce. Continuous mass accretion onto the PNS through narrow funnels delays the emergence of the spherical neutrino-driven wind, which is why we needed to continue the simulations including PNS and neutrino treatment for more than three seconds after bounce. Explosion energy and shock velocity in model s9.0 remain considerably lower than in the other two progenitors (see Figure 4).

4.2 Neutrino emission properties

In the following we present the neutrino emission properties of our two 3D simulations performed with the VERTEX-PROMETHEUS code. Figure 5 displays the neutrino luminosities (defined as 4π-integrated energy fluxes) and mean neutrino energies (defined as ratio of angle-averaged energy density to number density) for ν_e, $\bar{\nu}_e$

and heavy-lepton neutrinos ν_x, as well as the three lowest-order multipoles (monopole, dipole, and quadrupole) of the electron-neutrino lepton-number flux for models z9.6 and s9.0 as functions of post-bounce time (z9.6 left column, s9.0 right column). All quantities are evaluated at 400 km (transformed to an observer frame at rest at infinity). The formulas for the spherical harmonics decomposition are provided in Appendix C.

In the case of z9.6 the luminosities of all three species become very similar after only ~180 ms, signalling the end of PNS accretion caused by the quick onset of the explosion and the rapid shock expansion. In contrast, PNS accretion continues at a significant rate until roughly 350 ms in model s9.0. Only afterwards the luminosities in this model converge to nearly the same level, mirroring the characteristic trend when the cooling emission of the newly formed NS begins. Overall, the time evolution and the values of the neutrino luminosities and mean energies of both models are very similar to each other, consistent with the nearly equal masses of the PNSs in both cases (see Table 4). Model s9.0 exhibits additional accretion emission between ~150 ms and ~350 ms, which enhances the ν_e and $\bar{\nu}_e$ luminosities slightly and drives a continuous increase of the mean energies of ν_e and $\bar{\nu}_e$. However, the trend does not persist for long enough (and the PNS does not gain enough mass) to reach a crossing of the electron antineutrino energy with the heavy-lepton neutrino energy as reported by Marek et al. (2009) for more massive progenitors with more massive PNSs.

The bottom panels of Figure 5 demonstrate that both models develop a lepton-number emission dipole that dominates the higher-order multipoles and can reach and even exceed the monopole for longer periods of time (i.e., hundreds of milliseconds, see also Tamborra et al. 2014b). Note that the dipole amplitude displayed in Figure 5 is, by normalization, one third of the dipole amplitude considered by Tamborra et al. (2014b) (see also Appendix C). A long-lasting lepton-number emission dipole, whose direction is nearly stable or migrates only very slowly, is a characteristic feature of the LESA (Lepton-Emission Self-sustained Asymmetry) phenomenon that was first witnessed in 3D VERTEX-PROMETHEUS simulations with neutrino transport by Tamborra et al. (2014b) and Janka et al. (2016). This striking phenomenon has meanwhile been confirmed with fully multi-dimensional instead of ray-by-ray neutrino transport by O'Connor & Couch (2018b), Glas et al. (2019b) and Vartanyan et al. (2019).

Neither in model z9.6 nor in s9.0 does SASI play a role and, in addition, model z9.6 explodes after a very brief period of post-bounce accretion. In both models the PNS emission is therefore not masked by asymmetric accretion due to SASI shock sloshing or spiral motions. Because accretion in particular in model z9.6 does not contribute to the neutrino emission at any significant level after the onset of the explosion, its lepton-number flux asymmetry is merely determined by asymmetric convection inside of the PNS, where outward transport of lepton number is strongly suppressed in the anti-LESA direction. Therefore the lepton-number flux can even be negative in the anti-LESA direction (see Fig. 6, two upper left panels). This means that one hemisphere of the PNS radiates a greater number of $\bar{\nu}_e$ than ν_e, whereas there is the usual excess of ν_e number loss from the other hemisphere. The models, in particular z9.6 with no long-lasting accretion, therefore confirm that LESA is a phenomenon primarily generated by hemispherically asymmetric convection in the interior of the PNS, well below the neutrinosphere; the reader is referred to the more detailed discussion by Glas et al. (2019b), where also a 3D simulation with successful explosion of
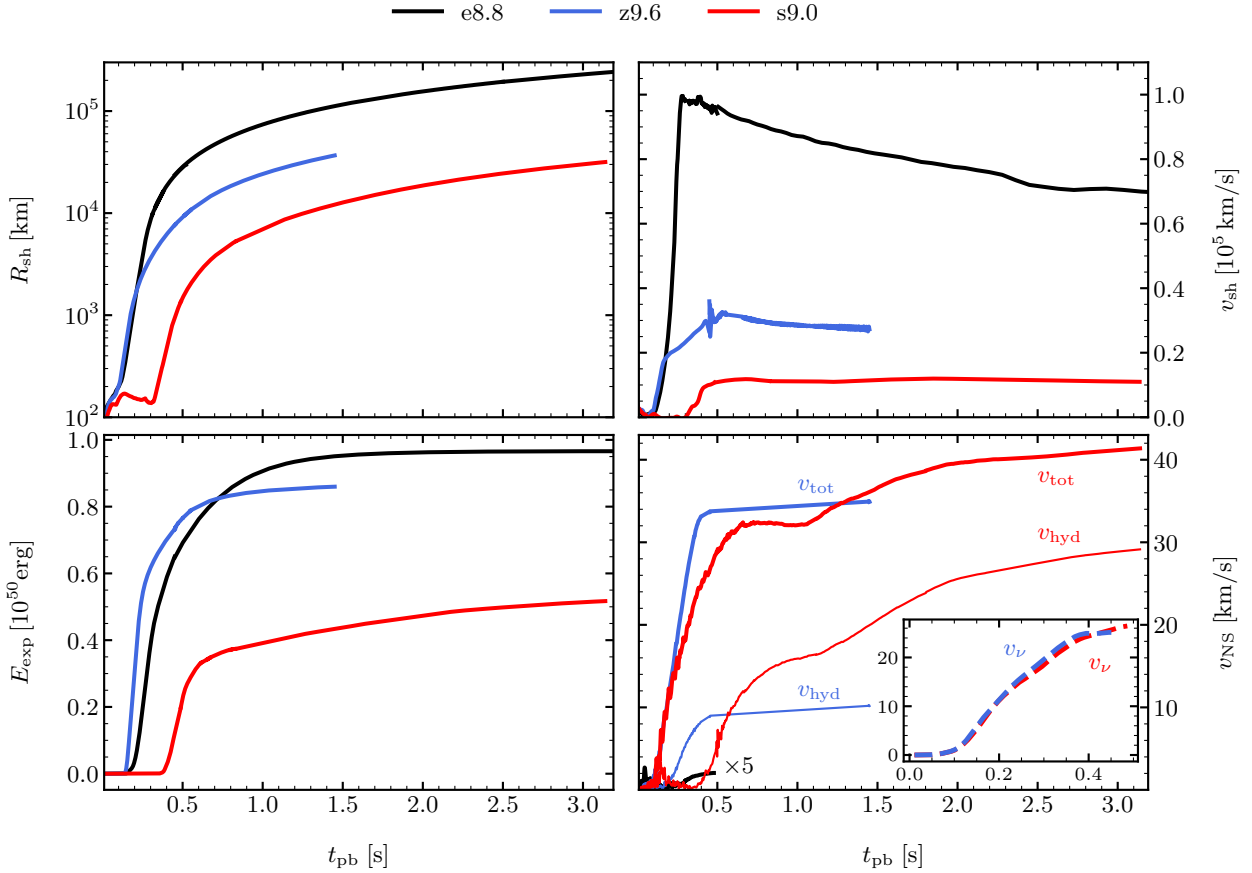
Figure 4. Shock radius (upper left panel), shock velocity (upper right panel) and diagnostic explosion energy (lower left panel) versus post-bounce time for all of our 3D models. The wiggles in the shock velocity of model z9.6 at ~0.45 s are a consequence of small-amplitude neutron-star vibrations when the VERTEX neutrino transport is switched off and the heating/cooling scheme of Appendix E is switched on. Owing to an improved treatment this numerical transient is much reduced in model s9.0. We also show the total PNS kick velocities (thick lines) and the hydrodynamically induced PNS kick velocities (thin lines) in the lower right panel. For better visibility, the inset of this panel displays the PNS kick velocities caused by asymmetric neutrino emission due to the LESA phenomenon (see text for details). The total velocities are the vector sum of the hydrodynamic PNS kick and the neutrino-induced kick. Despite nearly equal neutrino-induced kicks in z9.6 and s9.0 and lower hydrodynamic kick in z9.6, this latter model has a higher total kick velocity for some time, because its hydrodynamic and neutrino-induced kick directions are essentially parallel, in contrast to the situation in model s9.0. For the iron-core progenitors we can track only hydrodynamic contributions to the kick after the transport module of VERTEX-PROMETHEUS is switched off at $t_{neut} = 0.45$ s and $t_{neut} = 0.49$ s for models z9.6 and s9.0, respectively. For the ONeMg case our simplified neutrino treatment with the excised core of the PNS does not allow us to monitor the LESA induced kick. The kick of model e8.8 is scaled by a factor of 5 for better visibility.

the $9.0 M_\odot$ progenitor is evaluated.[7] It is also interesting to note that the lepton-emission multipole ($\ell \neq 0$) that grows fastest and thus develops high amplitudes of asymmetry first is the one of order $\ell = 4$, which is also in line with the results reported by Glas et al. (2019b).

Interestingly, there are phases in both of our models when the dipole and quadrupole amplitudes become similar (Figure 5). This is also suggested by the Aitoff projections for time t_{pb}=0.45 s near the end of our simulation of z9.6 (Fig. 6). At this late time a quadrupole pattern is superimposed on a hemispheric dipole asymmetry, whereas at $t_{pb} = 0.30$ s a much cleaner dipole is present. This reflects the evolution of the multipole amplitudes visible for z9.6 in

the bottom left panel of Figure 5. The late-time rapid growth of the dipole in the lepton-number emission of model s9.0 at $t_{pb} > 0.43$ s (bottom right panel of Figure 5) is an apparent feature caused by a transient phase of a reduced lepton-emission dipole between ~0.35 s and ~0.45 s. This reduction is a consequence of an accretion asymmetry that channels matter towards the PNS predominantly in one hemisphere, whereas a mighty outflow in the form of a huge, rising bubble develops in the opposite hemisphere (see the bottom panels of Figures 7 and 8). The main downflow direction is misaligned with the LESA dipole direction by roughly 90° and fuels enhanced lepton-number emission by the one-sided accretion. This enhanced lepton-number emission combined with the displaced LESA dipole strengthens the quadrupole component of the electron lepton-number emission and at the same time weakens its dipole. The remaining dipole level in the interval of [0.35 s, 0.45 s] signifies that the LESA dipole is stronger than the emission of lepton number by accretion. The dipole amplitude recovers to the full LESA

---

[7] In contrast to the models of Glas et al. (2019b), in which a 1D core of 10 km was used, the 3D simulations discussed here were computed with a very small central 1D core of only 1.6 km radius. Both sets of simulations show very similar LESA features, which means that the 10 km core had no relevant influence on the previous results.

Table 4. Overview of PNS properties in our multi-dimensional models at t_{map}.

Model	Dim.	t_{map} [s]	E_{exp} [10^{50} erg]	$v_{\mathrm{NS}}^{\mathrm{tot}}$ [km/s]	$v_{\mathrm{NS}}^{\mathrm{hyd}}$ [km/s]	v_{NS}^{ν} [km/s]	$J_{\mathrm{NS}}/10^{45}$ [cm^{2}g/s]	$\theta_{\nu J}$ [°]	α_{ej} [%]	α_{ν} [%]	M_{b} [M$_\odot$]	R_{NS} [km]	M_{map} [M$_\odot$]	M_{g} [M$_\odot$]	P_{NS} [s]
e8.8$_3$	2D	2.515	0.3	1.55	1.55	-	1.78	-	1.154	-	1.323	49.85	1.334	1.216	4.18
e8.8$_6$	2D	2.515	0.6	0.94	0.94	-	2.75	-	0.041	-	1.316	50.22	1.327	1.210	2.69
e8.8$_{10}$	2D	2.515	1.0	0.13	0.13	-	4.19	-	0.004	-	1.308	50.57	1.319	1.203	1.75
e8.8$_{15}$	2D	2.515	1.5	0.59	0.59	-	1.67	-	0.011	-	1.299	50.86	1.309	1.195	4.37
e8.8	3D	0.470	1.0	0.44	0.44	-	0.70	90.0	0.004	-	1.307	50.57	1.326	1.210	10.58
z9.6	3D	1.440	0.86	34.90	10.16	24.89	2.55	45.4	4.623	1.354	1.340	20.98	1.353	1.231	2.96
s9.0	3D	3.140	0.48	40.87	28.45	26.46	8.05	31.3	10.02	1.178	1.350	19.58	1.351	1.230	0.94

Notes: All values are given at the end of our explosion simulations with neutrino treatment (t_{map}). E_{exp} is the diagnostic explosion energy, which is essentially identical to the final explosion energy because of the small envelope binding energy (see Table 5). $v_{\mathrm{NS}}^{\mathrm{tot}}$ is the total NS kick velocity resulting from the hydrodynamic ($v_{\mathrm{NS}}^{\mathrm{hyd}}$) plus the neutrino-induced (v_{NS}^{ν}) contributions. We measure the contribution of neutrinos to the total kick until the neutrino transport is switched of at $t_{\mathrm{neut}} = 0.45$ s and $t_{\mathrm{neut}} = 0.49$ s after core bounce for models z9.6 and s9.0, respectively. Hydrodynamic contributions and total kick velocities are monitored until t_{map}. J_{NS} is the total angular momentum transported to the PNS through a radius of 100 km until t_{map}. $\theta_{\nu J}$ is the angle between the direction of the total kick velocity $\boldsymbol{v}$ and the direction of $\boldsymbol{J}$. α_{ej} and α_{ν} are the final hydrodynamic and neutrino anisotropy-parameters, respectively (see Appendix D). For the iron-core progenitors we average α_{ν} over the time when the emission dipole is largest until the end of the simulation. M_{b} is the baryonic PNS mass, which is defined as the enclosed mass within the radius R_{NS}, at which the density drops below 10^{11} g cm^{-3}. Note that for the simulations of the e8.8 progenitor, R_{NS} is determined by the chosen parameters of the inner grid boundary (see Table 2). M_{map} (see also Table 3) is the central mass contained within the excised region, from which we calculate the gravitational mass M_{g} for a PNS radius of 12 km (see Appendix D). P_{NS} is the PNS spin period at the end of our post-bounce simulations, assuming a final NS radius R_{NS} of 12 km, angular momentum conservation, and a gravitational mass of M_{g}.

strength after $t_{\mathrm{pb}} \sim 0.45$ s because the mass-accretion rate onto the PNS declines continuously.

The Aitoff projections show that not only the electron-neutrino lepton-number flux exhibits large-scale (low-order multipolar) asymmetries, but also the ν_e plus $\bar{\nu}_e$ energy flux as well as the total neutrino energy flux (the summed energy fluxes of ν_e plus $\bar{\nu}_e$ plus four times that of ν_x). However, while the directional variations of the lepton-number flux can be several times bigger than the angular average of this quantity, the ν_e plus $\bar{\nu}_e$ energy flux varies only within roughly 6–8% and the total neutrino energy flux even less within about 4–6% (Figure 6). These directional variations, in particular the hemispheric asymmetries, have consequences for NS kicks and the neutron-to-proton ratio in the ejecta. This will be discussed in the following Sections 4.3 and 4.4.

4.3 Neutron star kicks by asymmetric mass ejection and neutrino emission

In order to compare the final state of the post-bounce simulations of our model set, we present in Figure 7 planar slices showing the entropy at the times t_{map} when we start our long-time simulations. The left panels are chosen such that they align with the plane of the largest shock deformation. The right panels align with the plane of the smallest shock deformation. Note the basically spherical shape of the shock and the mild post-shock asymmetries in both the e8.8 and z9.6 models. In strong contrast to the ECSN-like models, model s9.0 shows a clear dipolar shock deformation and ejecta morphology.

The asymmetries that develop during the explosion also affect the kick of the PNS. In Table 4 we provide properties of the PNS resulting from our post-bounce simulations.[8] We list the PNS kick velocity (v_{NS}), ejecta anisotropy parameter (α_{ej}), PNS angular momentum (J_{NS}), angle between total PNS kick and angular momentum vector $\theta_{\nu J}$ and PNS spin period (P_{NS}) along with the

[8] We refer the reader to Appendix D for the equations involved in the analysis underlying the results presented in Table 4.

PNS radius (R_{NS}) and baryonic PNS mass (M_{b}) at the moment in time (t_{map}) when we terminate the post-bounce simulations that include neutrino transport or neutrino heating (see also Table 3). The PNS radius R_{NS} is defined as the radius where the angle-averaged density drops below 10^{11} g cm^{-3}. The PNS mass M_{b} is the mass contained interior to R_{NS}. M_{map} is the mass contained within our inner grid boundary, and thus removed from the hydrodynamic grid at the start of the long-time simulations at t_{map} (see Table 3). M_{g} the corresponding gravitational mass.

The acceleration of the PNS is caused by two different mechanisms. Firstly, aspherical ejection of matter leads to a gravitational tug, which accelerates the PNS into the hemisphere opposite to the maximum shock expansion and fastest ejecta (Scheck et al. 2006; Wongwathanarat et al. 2010b, 2013). Secondly, anisotropic neutrino emission, due to the LESA phenomenon (Tamborra et al. 2014b), can accelerate the PNS opposite to the direction of the largest total neutrino-energy flux. LESA manifests itself in a dominant and stable $\ell = 1$ spherical harmonics mode of the lepton-number emission and a corresponding energy-emission dipole amplitude of several percent compared to the monopole (see Tamborra et al. 2014a; Tamborra et al. 2014b, and Section 4.2). LESA is observed in both simulations conducted with VERTEX-PROMETHEUS. The almost spherical explosions of the ECSN-like progenitor yield very low hydrodynamic kick velocities by the "gravitational tug-boat effect" (Gessner & Janka 2018). Anisotropic neutrino emission cannot be evaluated in our simulation of model e8.8, because of the spherical treatment of the central PNS region. The kick contribution by anisotropic neutrino emission in model s9.0 is of a magnitude comparable to the contribution associated with the aspherical ejection of matter and even exceeds the hydrodynamic kick contribution in model z9.6.

We show in Figure 8 planar slices of the electron fraction (left panels) and entropy per nucleon (right panels) of the iron-core progenitors. The black, blue, and green arrows indicate the total, hydrodynamic, and neutrino-induced directions of the PNS kick. In the case of model z9.6, the hydrodynamic and neutrino-induced kicks are nearly aligned. This results from the anti-correlation of the LESA lepton-number emission dipole and the direction of the maximum $\nu_e + \bar{\nu}_e$ as well as total neutrino luminosity (see Tamborra
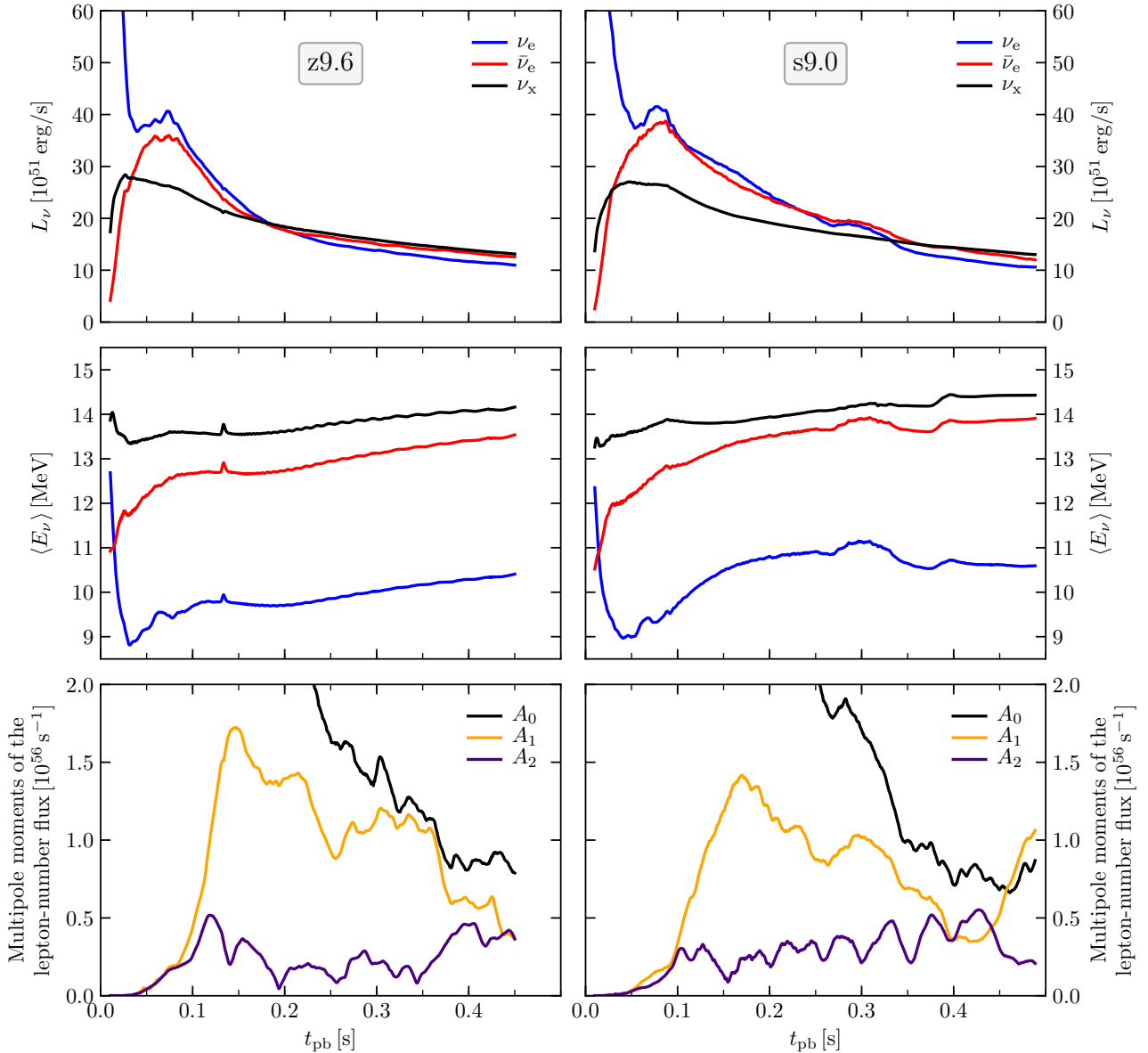
Figure 5. Neutrino luminosities (top), mean energies (middle), all averaged over all viewing directions, and lowest-order multipole moments (A_0, A_1, A_2 for monopole, dipole, and quadrupole) of the electron-neutrino lepton-number flux (bottom) as functions of time for models z9.6 (left) and s9.0 (right). All quantities are evaluated at 400 km, transformed to an observer frame at rest at infinity. With ν_x we denote one species of the heavy-lepton neutrinos. Note that the dipole moment, A_1, plotted here is one third of the dipole amplitude of the lepton-number flux defined by Tamborra et al. (2014a) (see Appendix C for details).

et al. 2014b and Section 4.2). Increased heating by $\nu_e + \bar{\nu}_e$ absorption in the postshock region in the hemisphere opposite to the LESA dipole pushes the SN shock to larger radii. The induced asymmetry of the post-shock ejecta leads to the hydrodynamic acceleration of the PNS in the opposite direction due to the gravitational pull of the slower ejecta. The neutrino-induced NS kick acts in the same direction, i.e., nearly aligned with the LESA dipole, because of the maximum total neutrino luminosity being in the anti-LESA direction.

Due to the weak postshock convection and only small-scale ejecta asymmetries in model z9.6, the anisotropic neutrino emission produces the dominant contribution to the PNS kick. While the gravitational tug of the ejecta can only account for $v_{\mathrm{NS}}^{\mathrm{hyd}} \sim 10\,\mathrm{km\,s^{-1}}$, the asymmetric emission of neutrinos alone would cause a kick velocity

of $v_{\mathrm{NS}}^{\nu} \sim 25\,\mathrm{km\,s^{-1}}$. The total kick sums up to $v_{\mathrm{NS}}^{\mathrm{tot}} \approx 35\,\mathrm{km\,s^{-1}}$. A correlation or even alignment of the neutrino-induced and hydrodynamic kicks is less clear in model s9.0. The asymmetric neutrino energy emission is also responsible for a sizeable contribution to the PNS kick in this case, and even for the dominant contribution during the first 0.5 s after bounce. However, the neutrino-induced kick in s9.0, despite being in the same hemisphere as the LESA dipole vector, is not closely aligned with the LESA dipole direction as in model z9.6. The hydrodynamic PNS kick, however, is in the opposite hemisphere, different from the case of model z9.6. Both, this different orientation of the hydrodynamic kick relative to the LESA dipole, and the misalignment of LESA direction and neutrino-induced kick in model s9.0, are a consequence of the fact that hydrodynamic instabilities in the postshock layer are much
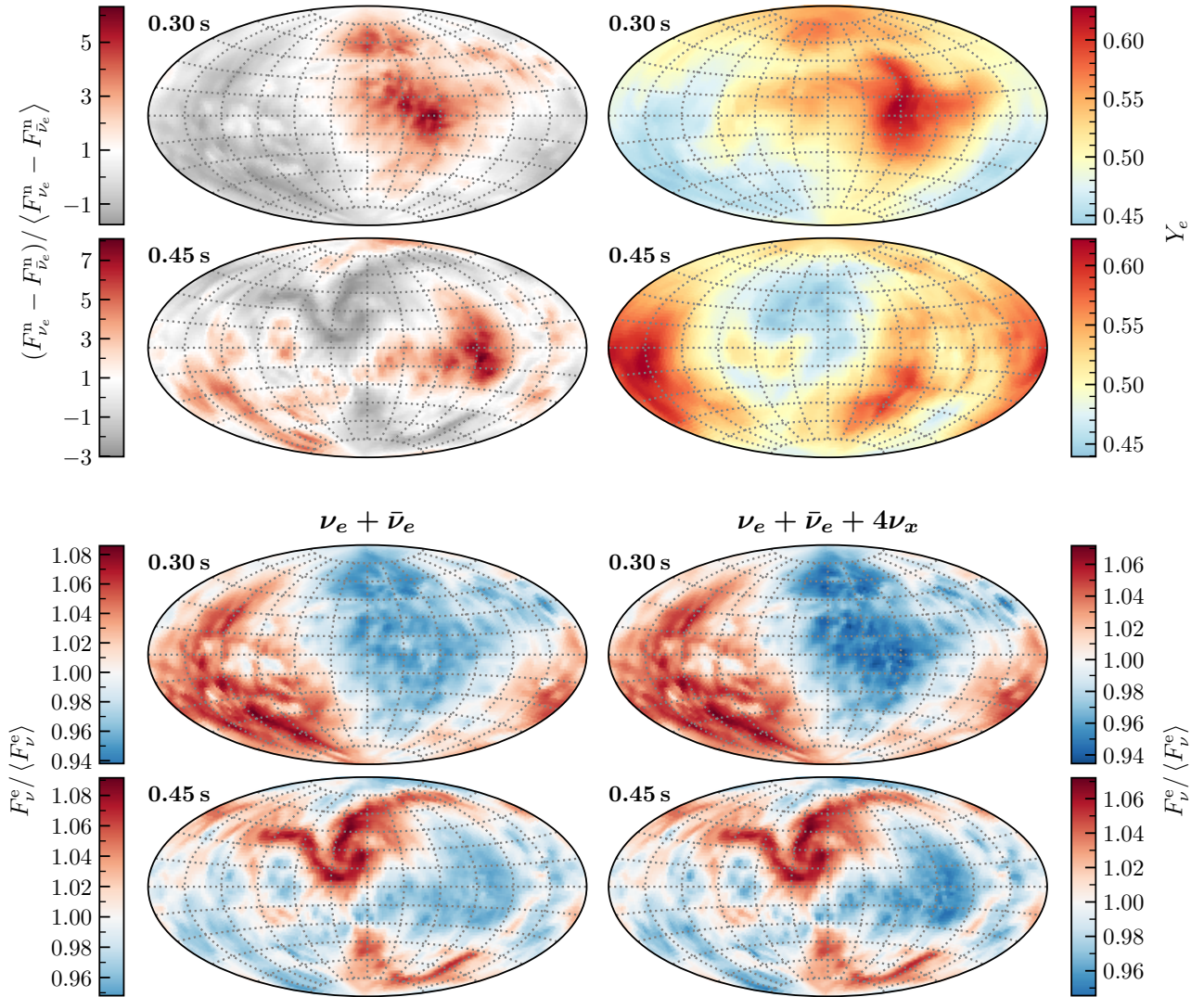
Figure 6. Full-sphere Aitoff projections of various LESA related quantities for model z9.6 at 0.30 s and 0.45 s after bounce. The two upper left panels display the relative variation of the electron-neutrino lepton-number flux, $(F_{\nu_e}^n - F_{\bar{\nu}_e}^n)/\langle F_{\nu_e}^n - F_{\bar{\nu}_e}^n \rangle$ (normalized by the angular average) at a fixed radius of 400 km as function of polar angles θ and ϕ. The two upper right panels show the variation of the electron fraction Y_e in the neutrino-heated ejecta at 250 km. The two lower left panels visualize the relative variation of the energy flux of ν_e plus $\bar{\nu}_e$, and the two lower right panels the corresponding relative variation of the total energy flux as sum of all contributions of ν_e, $\bar{\nu}_e$ and ν_x, again evaluated for lab-frame quantities at 400 km. Note that the amplitude of the energy-flux variation is considerably lower than that of the lepton-number flux, and the dipole directions of both fluxes possess opposite orientations.

stronger and longer-lasting. Therefore the corresponding asymmetries of the mass distribution around the PNS are more extreme in model s9.0 than in z9.6. The direction of the neutrino-induced kick is thus affected by the neutrino-emission dipole that is associated with one-sided PNS accretion. This asymmetric neutrino-emission due to accretion is transiently superimposed on the LESA dipole during the time interval of [0.35 s,0.45 s] after bounce. It is displaced by roughly 90° from the LESA direction (see Section 4.2) and thus shifts the neutrino-induced kick away from the LESA direction (Figure 8, lower panels).

The neutrino-heating asymmetry associated with LESA, causing more heating in the anti-LESA direction (where the ν_e plus $\bar{\nu}_e$ luminosity is higher and also the number flux of the $\bar{\nu}_e$ with their harder spectra is higher), has a mild influence only in model z9.6. Therefore the explosion in this model is slightly stronger in the anti-LESA direction, and the hydrodynamic PNS kick is nearly aligned with the LESA vector and with the direction of the neutrino-induced

PNS kick. In contrast, in model s9.0 the neutrino-heating asymmetry associated with LESA is not powerful enough to determine the deformation of the explosion. Convective mass motions, the corresponding accretion asymmetries, and the associated anisotropic neutrino emission and absorption between PNS and SN shock play a more important role and have a dominant influence on the morphology of the postshock flow. In model s9.0 the shock expansion and explosion are weaker in the anti-LESA direction, where convective downdrafts towards the PNS are numerous and massive and thus direct the hydrodynamic PNS kick towards this hemisphere (blue arrows in the southern hemisphere of the lower panels of Figure 8). As explained above, accretion-associated asymmetries of the total neutrino luminosity are also the reason why the neutrino-induced kick is not well aligned with the LESA lepton-emission dipole. The combined hydrodynamic and neutrino-induced kicks in model s9.0 lead to a PNS velocity of ~41 km s⁻¹ at mapping time t_{map}. It must be emphasized that in both models, z9.6 and s9.0,
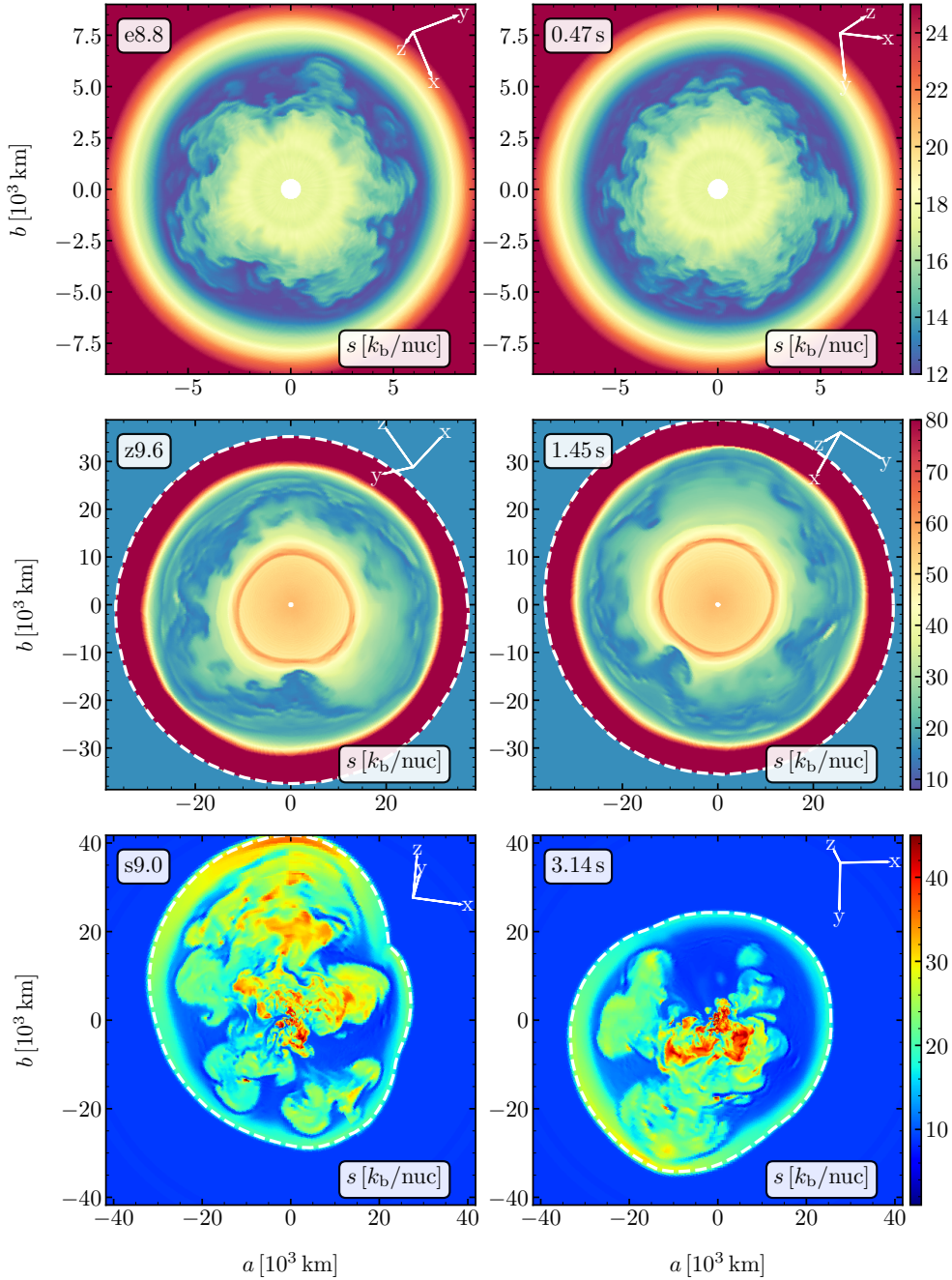
Figure 7. Planar slices of our 3D models showing the entropy color-coded at t_{map}. The left panels display the plane of largest shock deformation, whereas the right panels present the plane of smallest shock expansion. The coordinate directions of the plots (indicated by the tripods in the top right corners) have no association with the coordinates of the computational grid. Note the almost spherical morphology of model e8.8 and the deformed ejecta morphology of models s9.0 and z9.6. For better visibility of the small-scale structures of model s9.0 we choose a different color representation in this case. The white dashed line marks the shock surface. This line is missing in the top two panels because in model e8.8 the shock is at more than 20,000 km at this time already, far ahead of all explosion asymmetries.

the VERTEX-PROMETHEUS neutrino transport was switched off after about 0.5 s of post-bounce evolution, namely at ~0.45 s and ~0.49 s after bounce, respectively. At this time the neutrino-induced kicks have not reached their final values, which might be higher than the numbers presented in Table 4.

4.4 Electron fraction of neutrino-heated ejecta

Since the explosions of models z9.6 and s9.0 are computed with detailed neutrino transport, we describe the evolution and distribution of their electron fraction, Y_e, in the following. Corresponding 2D results obtained for ECSN models in simulations with the VERTEX-PROMETHEUS and COCONUT-VERTEX codes were presented by Wanajo et al. (2011) and Wanajo et al. (2018), respectively. The
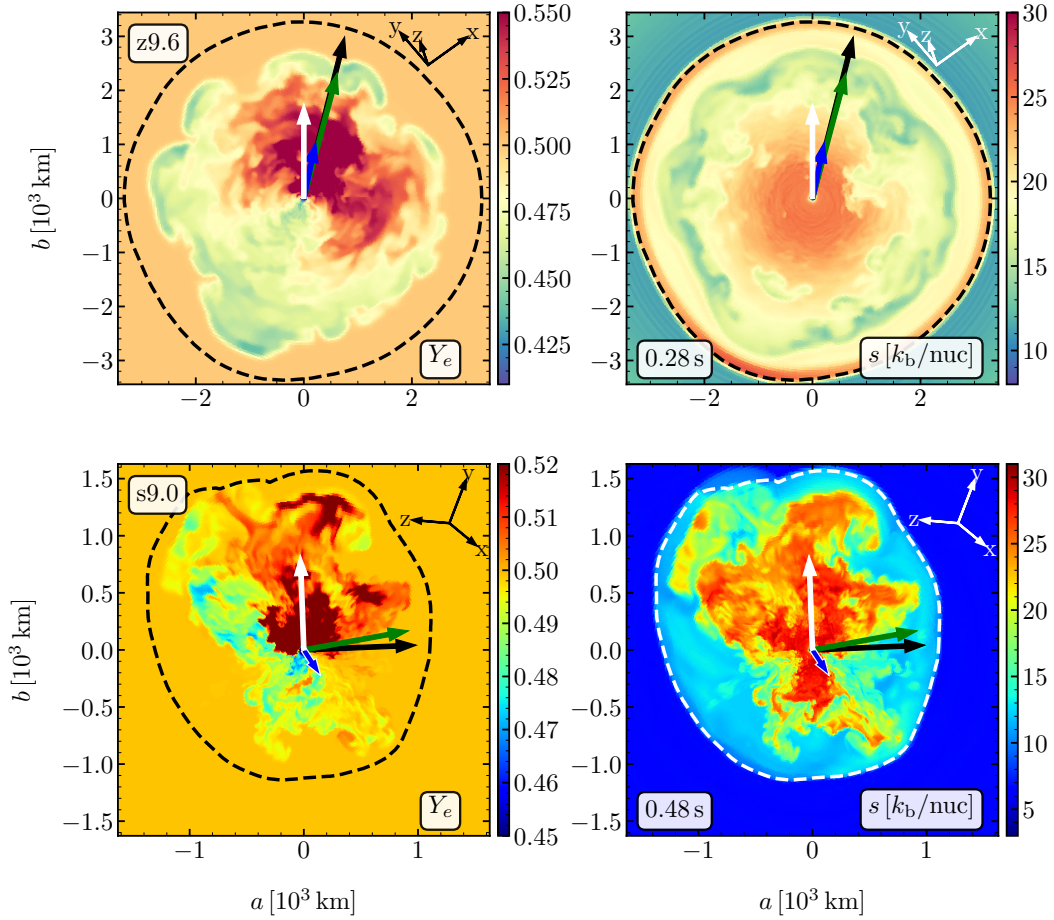
Figure 8. Planar slices of the electron fraction Y_e (left panels) and entropy per nucleon (right panels) of models z9.6 and s9.0 at 0.28 s and 0.48 s after bounce, respectively. We choose times where the LESA dipole is strong in both models. The planes are spanned by the LESA vector (white arrow) and the vector of the total PNS kick (black arrow) and oriented such that the LESA dipole direction points to the north. The positioning of the plane in the global coordinate system of the simulation output is shown by the tripod in the upper right corner of each panel. The arrows indicate the directions of the total PNS kick velocity (black), the hydrodynamic PNS kick velocity (blue), and the neutrino-induced kick velocity of the PNS (green), all computed as integrals of the accelerations until the displayed times. The black or white dashed lines mark the shock radius. Note that in model z9.6 the blue and green arrows are nearly aligned, adding up to the black arrow.

electron fraction in the neutrino-heated ejecta of our 3D model e8.8 is only approximate because of the simplified treatment of the neutrino physics and the replacement of the central $1.1\,M_\odot$ PNS core by an inner grid boundary in the simulations with the PROMETHEUS-HOTB code (see Section 3.2). Therefore we will not further discuss the neutron-to-proton ratio in the ejecta of this model but refer the reader to Wanajo et al. (2011) and Wanajo et al. (2018).

The Y_e distributions of models z9.6 and s9.0 in the left panels of Figure 8 exhibit a clear asymmetry: proton-rich neutrino-driven outflow (red and orange) in the hemisphere of the LESA dipole vector, and neutron-rich neutrino-wind ejecta (blue hues) in the opposite hemisphere. The proton excess is a consequence of the fact that the PNS develops an enhanced emission of ν_e relative to $\bar{\nu}_e$ in the hemisphere of the LESA direction, which leads to a predominant production of protons by ν_e absorption on neutrons ($\nu_e + n \rightarrow e^- + p$) in the ejecta of the same hemisphere. In the anti-LESA direction the emission of $\bar{\nu}_e$ by the PNS is relatively higher, allowing for more efficient creation of neutrons through the reaction $\bar{\nu}_e + p \rightarrow e^+ + n$ in the neutrino-heated outflow.

In addition to this spatial asymmetry in the neutron-to-proton ratio, which is present in both explosion models computed with the

VERTEX-PROMETHEUS code, model z9.6 exhibits neutron-richness in the mushroom-shaped heads of Rayleigh-Taylor plumes in all directions, very similar to previous findings in 2D explosion simulations of the low-mass progenitors of models e8.8 and z9.6 with self-consistent neutrino transport (see Wanajo et al. 2011; Wanajo et al. 2018). The plumes contain the earliest neutrino-heated ejecta. Their neutron excess is explained by the extremely fast outward propagation of the SN shock in these two models, which is enabled when the mass-accretion rate of the shock plummets because of the steep density decline at the edge of the degenerate core. The fast shock acceleration allows the neutrino-heated, buoyant gas to expand very quickly away from the gain radius. The gas rises so rapidly that neutrino absorption is unable to increase Y_e from its low values ($\sim$0.25–0.35) near the gain radius to 0.5 or higher. Instead, the mushroom plumes stay considerably neutron rich in model z9.6, in contrast to model s9.0, where the slower shock acceleration and the correspondingly slower expansion of the first bubbles of neutrino-processed matter lead to Y_e around 0.5 due to the dominant absorption of ν_e (Figure 8).

Figure 9 permits a closer look at the situation in model z9.6. The upper left panel displays trajectories (projected onto the x-y-
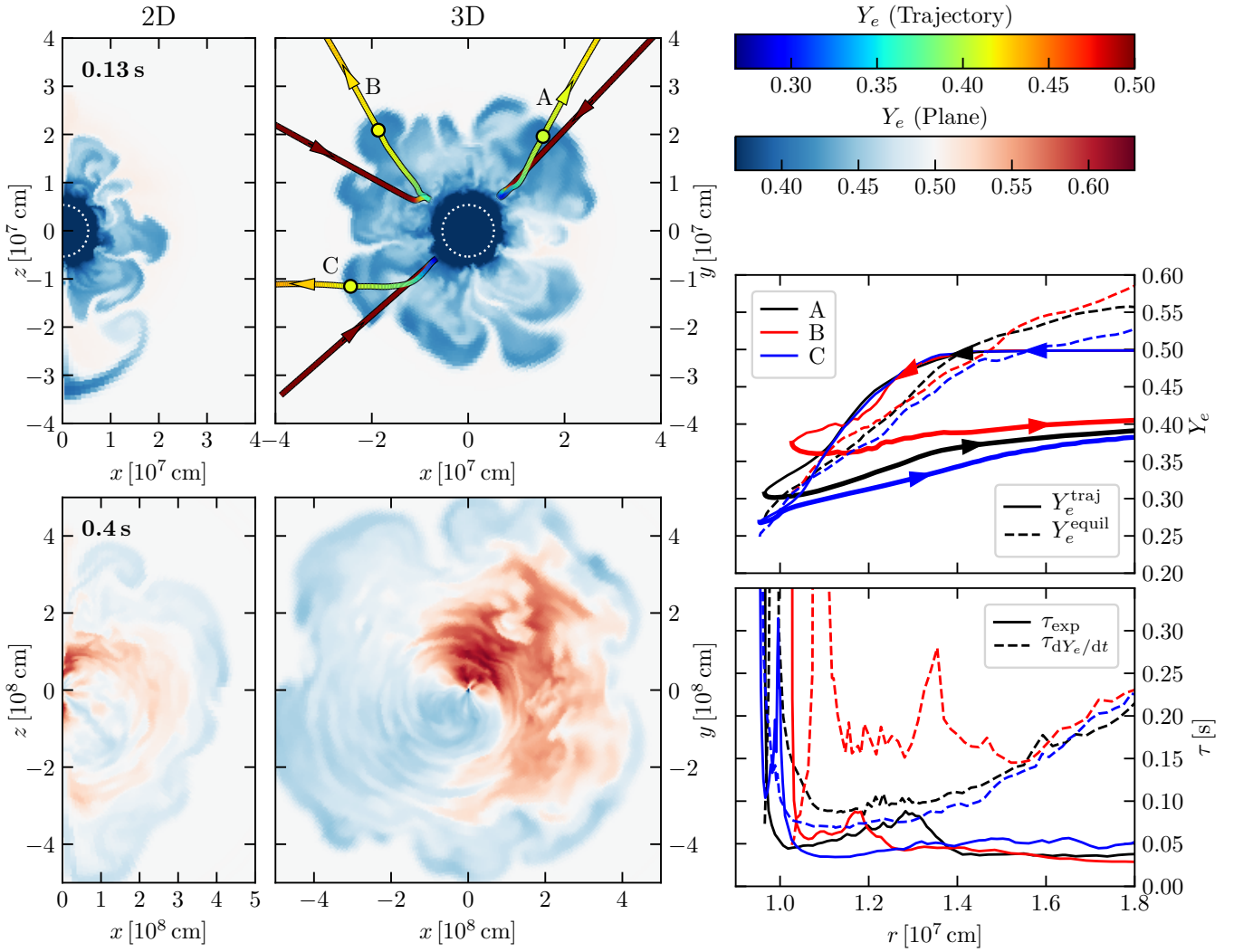
Figure 9. *Left panels:* Distribution of Y_e in cross-sectional slices of 2D (left) and 3D (right) simulations of model z9.6 at 0.13 s (top) and 0.4 s (bottom) after core bounce. The ejection of neutron-rich matter (with $0.39 \lesssim Y_e \lesssim 0.50$) in fast-rising, buoyant plumes is visible. Note that the chosen color range (lower color bar) does not allow to display the Y_e variation at radii below ~100 km. The colored lines visualize the infall and escape trajectories (projected onto the x-y-plane of the cross-sectional slice, the flow direction is marked by arrows) for three selected mass elements (trajectories A,B,C), which ultimately get expelled in the neutron-rich mushroom heads. The local Y_e value along the trajectories is color coded according to the upper color bar. The Y_e evolution of these fluid elements is more quantitatively represented in the right panels. The locations of these elements at the time of the plot (0.13 s) are indicated by small colored circles. The white dotted circle marks the mean neutrinosphere, defined by a spectrally averaged optical depth of 2/3. The lower left panels, besides showing the farther expanded, neutron-rich plumes, display neutrino-driven wind ejecta, which develop neutron-rich conditions in one hemisphere (bluish colors) and proton-richness in the opposite hemisphere (reddish colors) because of the LESA dipole asymmetry of the ν_e and $\bar{\nu}_e$ emission from the nascent neutron star. We stress that the increase of Y_e in the expanding mushroom heads between 0.13 s and 0.40 s is not a consequence of neutrino reactions (which basically cease at $r \gtrsim 250$ km). Instead, a gradual, slow Y_e increase is caused by numerical diffusion connected with the ejecta mass flowing over the Eulerian grid. *Upper right panel:* Evolution of the electron fraction for the three selected mass elements that are ejected in the neutron-rich mushroom heads. The Y_e evolution during the infall is shown by thin solid lines, during the re-ejection by thick solid lines (indicated by arrows). Note that during the infall all three lines, A, B, and C, lie on top of each other, starting at $Y_e = 0.5$. The dashed lines represent the local electron fraction, Y_e^{equil}, for reactive equilibrium. *Bottom right panel:* Expansion timescale, τ_{exp} (solid lines), and timescale of Y_e changes, $\tau_{\text{d}Y_e/\text{d}t}$ (dashed lines), measured along the outflow parts of the solid curves in the upper right panel.

plane) of three infalling, then neutrino-heated, and finally outgoing mass elements. The color-coding of these trajectories as well as the upper right panel show that the infalling matter starts with a value of $Y_e = 0.5$, gets neutronized by electron captures during infall, reverses direction at a minimum radius around 100 km close to the gain radius, and experiences an increase of Y_e again as it speeds away from the gain radius. The rise of Y_e, however, flattens when the expansion time scale, $\tau_{\text{exp}} = r\,|v_r|^{-1}$ (with v_r being the local radial

component of the velocity), becomes shorter than the timescale of Y_e changes, $\tau_{\text{d}Y_e/\text{d}t} = Y_e\,|\dot{Q}_{Y_e}|^{-1}$ (with $\dot{Q}_{Y_e}$ being the local net rate of ν_e and $\bar{\nu}_e$ emission and absorption reactions as computed during the hydrodynamic simulation). This can be seen in the upper and lower right panels. The electron fraction in the expanding ejecta stays well below the value for local kinetic equilibrium, Y_e^{equil}, which corresponds to the condition when ν_e and $\bar{\nu}_e$ absorption and
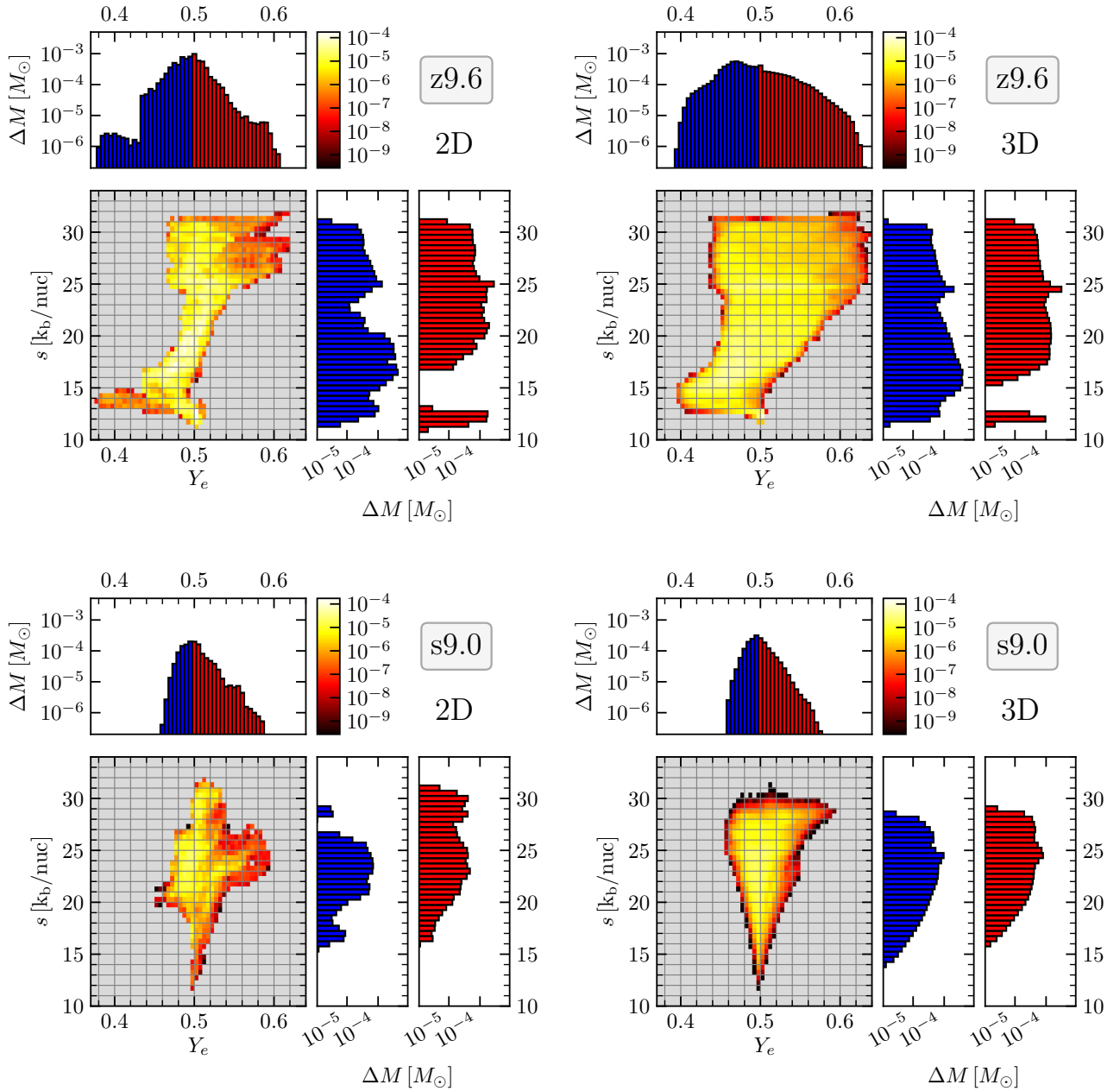
Figure 10. Ejecta mass distributions versus Y_e and entropy per nucleon, s (in units of Boltzmann's constant), for 2D (left) and 3D (right) simulations of model z9.6 (top) and model s9.0 (bottom). The central panels in each case display the mass distribution in the Y_e-s-plane (color coding in units of $M_\odot$ according to the color bar), the corresponding panels above and to the right show the marginal distributions. Blue and red bars indicate $Y_e < 0.5$ and $Y_e > 0.5$, respectively. In order to minimize effects of numerical diffusion, the mass distributions for Y_e and s were measured for outflowing material ($v_r > 0$) at a radius of $r = 250$ km.

emission reactions are balanced for the density and temperature of the tracked mass elements at each radius r. Close to the point of return the radial velocities become small and $\tau_{\exp}$ increases steeply, whereas farther out $|v_r| \propto r$ roughly holds and $\tau_{\exp}$ becomes nearly constant. The values of $\tau_{dY_e/dt}$ for trajectories A and C increase at small radii, because these mass elements approach the NS so closely that their Y_e at the return point drops to values near $Y_e^{\rm equil}$, for which reason $\dot{Q}_{Y_e}$, the net rate of Y_e changes, becomes low. In contrast, mass element B returns outward at a considerably larger radius and its Y_e value never gets close to the local $Y_e^{\rm equil}$. Only at $r \approx 110$ km the condition $Y_e^{\rm traj} \sim Y_e^{\rm equil}$ is incidentally fulfilled in mass element B, and $\tau_{dY_e/dt}$ exhibits a prominent maximum at this position. With

growing distance from the NS, $\tau_{dY_e/dt}$ increases and exceeds the expansion timescale, because all neutrino rates become slow and ultimately cease when the mass elements gain distance from the neutrino source and move to low densities and temperatures. This explains why the asymptotic values of Y_e along the trajectories stay well below the local equilibrium values at large radii.

In order to unravel similarities and differences between our current 3D models and the 2D explosion simulations of low-mass progenitors considered previously by Wanajo et al. (2018), we compare the ejecta properties of our 3D models to corresponding 2D results in the following three paragraphs. Neutron-rich, buoyant, fast plumes are not only present in the 3D case but also in the cor-

Table 5. Total masses of chemical elements M_i of the pre-collapse progenitor models as shown in Figure 2 (top), behind the shock front in our 3D SN simulations at the time of mapping to the long-time runs, t_{map}, and at the time when the entire shock has broken out from the surface of the exploding star, t_{sbo}. Also given are the binding energies still ahead of the shock at time t_{map}.

	e8.8	z9.6	s9.0	e8.8	z9.6	s9.0
		M_i [M$_\odot$]			M_i [M$_\odot$]	
Species		Progenitor				
H	2.68	5.10	4.54			
^{4}He	1.79	3.11	2.68			
^{12}C	2.71×10^{-2}	2.24×10^{-2}	3.37×10^{-2}			
^{16}O ^{20}Ne ^{24}Mg	0.94	0.04	0.13			
^{28}Si	3.98×10^{-3}	2.32×10^{-2}	1.34×10^{-2}			
Iron-group/NSE	0.39	1.30	1.32			
Species		Postshock ejecta at t_{map}			Postshock ejecta at t_{sbo}	
n	-	4.25×10^{-5}	8.22×10^{-8}	-	-	-
p	-	4.64×10^{-4}	7.27×10^{-5}	-	5.34×10^{-4}	5.81×10^{-5}
H	1.97×10^{-7}	0	0	2.68	5.10	4.54
^{4}He	4.90×10^{-3}	8.24×10^{-3}	5.48×10^{-5}	1.74	3.12	2.68
^{12}C	4.08×10^{-5}	1.52×10^{-3}	3.25×10^{-3}	2.19×10^{-2}	2.26×10^{-2}	4.04×10^{-2}
^{16}O ^{20}Ne ^{24}Mg	1.00×10^{-4}	2.20×10^{-3}	4.13×10^{-2}	4.95×10^{-2}	7.76×10^{-3}	0.11
^{28}Si	1.63×10^{-5}	2.27×10^{-4}	1.29×10^{-3}	1.33×10^{-3}	2.71×10^{-4}	7.10×10^{-3}
^{56}Ni or ^{56}Ni ^{56}Co ^{56}Fe	1.05×10^{-3}	6.50×10^{-4}	4.72×10^{-3}	3.41×10^{-3}	3.93×10^{-3}	6.35×10^{-3}
Tr	6.69×10^{-3}	1.05×10^{-3}	1.06×10^{-6}	1.30×10^{-2}	1.05×10^{-3}	8.62×10^{-7}
Binding energy ahead of the shock at t_{map}		[10^{47} erg]				
$E_{bind}(r > R_{sh})$	-0.56	-6.89	-9.76			

Notes: n and *p* label free neutrons and protons, respectively, left unbound after the freeze-out from NSE, whereas H labels hydrogen from the envelope. Since the onset of the explosion of model e8.8 was simulated with PROMETHEUS-HOTB, no free protons remain in the ejecta. The high mass of ^{4}He compared to ^{56}Ni and Tr in model z9.6 at t_{map} is a consequence of the high value of the temperature when NSE was switched off in this simulation, $T_{NSE} \sim 5.8 \times 10^9$ K, instead of $T_{NSE} \sim 4.0 \times 10^9$ K in model s9.0. $E_{bind}(r > R_{sh})$ is the total binding (i.e. internal + kinetic + gravitational) energy ahead of the shock at the mapping time t_{map}. Free neutrons at t_{map} are assumed to decay and are added to free protons at t_{sbo}. Since our network in the long-time runs contains only ^{56}Ni, ^{56}Co, and ^{56}Fe, all other iron-group species (from the explosion models or the progenitor) are included in the mass of these nuclei listed for t_{sbo}.

responding 2D models (left panels in Figure 9). However, in the 2D case extended regions around the PNS with proton excess or neutron excess exist in all directions in the northern as well as southern hemisphere. If this finding is connected to a 2D phenomenon that corresponds to LESA in 3D, the LESA direction is less stable in 2D than in 3D. Indeed, an inspection of the dipole of the electron-neutrino lepton-number flux shows that the dipole direction in 2D flips from one hemisphere to the other with a full cycle period of ~0.1 s. Moreover, the grid axis seems to have a disturbing influence that leads to artificial effects, because both in the northern and southern directions proton-rich, collimated outflows appear very close to the axis, where they are much stronger than at large angles away from the axis. Because of the influence of the artificial symmetry axis, it is not easy to diagnose whether the flipping 2D dipole has any physical relation to the stable or slowly migrating lepton-emission dipole of LESA in 3D.

In Figure 10, we present the ejecta mass distributions versus entropy per nucleon, s, and electron fraction, Y_e, for 2D and 3D simulations of z9.6 (top) and s9.0 (bottom), including the fast convective plumes as well as the neutrino-driven wind material. The mass distributions are constructed by integrating all matter that flows through a sphere of 250 km radius with positive radial velocities. This choice of radius ensures that neutrino interactions have essentially ceased at this location, but effects due to numerical diffusion and mixing in the outflowing material, when it moves across the Eulerian (i.e., spatially fixed) computational grid, are minimized in the mass-versus-Y_e distributions extracted from the simulations for nucleosynthesis discussions. A comparison of the upper and lower left panels in Figure 9 demonstrates the consequences of this diffusion. The mushroom heads are very neutron rich at 200–300 km and $t_{pb} = 0.13$ s. However, although the neutrino reactions basically cease at $r \gtrsim 250$ km, the electron fraction in the nearly self-similarly expanding mushroom heads still continues to increase slowly to values closer to 0.5 (see lower left panels for $t_{pb} = 0.4$ s). This is partly an unphysical, but unavoidable, consequence of the fact that the mushroom heads experience gradual numerical mixing (besides some unclear degree of physical mixing) with the surrounding postshock matter, which possesses $Y_e = 0.5$.

The 2D and 3D mass distributions exhibit close similarity in their shapes as well as widths, with differences only in details of their substructure. These differences originate mainly from the fact that in 2D there are only a few plumes, which are axially symmetric, massive objects, whereas in 3D there is a greater number of such bubbles, of which each one contains less mass than the toroidal 2D objects. The 3D distributions are therefore smoother and possess less fine structure. The total masses of neutrino-processed ejecta until about 0.5 s after bounce are 10.34×10^{-3} M$_\odot$ in model z9.6 and 2.64×10^{-3} M$_\odot$ in model s9.0. In both cases about 60% of these masses are in the fastest mushroom-shaped plumes, the remaining 40% are carried by the neutrino-heated subsequent outflows. Also in both cases roughly 50% of this latter component are neutron-rich (1.90×10^{-3} M$_\odot$ in z9.6 and 0.55×10^{-3} M$_\odot$ in s9.0), and about 50% are proton-rich (2.31×10^{-3} M$_\odot$ in z9.6 and 0.51×10^{-3} M$_\odot$ in s9.0).

The mass-versus-Y_e distributions of model z9.6 in 2D and 3D resemble closely the corresponding distributions obtained in

2D explosion simulations for the ONeMg-core progenitor e8.8ₙ (mentioned in Section 2.1) and for our $9.6\,M_\odot$ Fe-core progenitor and another ultra-metal-poor Fe-core progenitor of $8.1\,M_\odot$, whose results were presented in Wanajo et al. (2011) and Wanajo et al. (2018) (see figure 2 in both papers). In all cases the distributions are very wide, stretching from $Y_e \sim 0.55$–0.6 on the proton-rich side to $Y_e \sim 0.40$ (or even a bit lower in the 2D models) on the neutron-rich side. The corresponding nucleosynthetic abundance patterns are extremely similar and characteristic of this class of "ECSN-like" explosions, with high production factors for light trans-Fe elements from Zn to Zr, resulting from the appreciable ejection of neutron-rich matter in these models (Wanajo et al. 2018). In contrast, model s9.0 displays a mass-vs-Y_e distribution that resembles the result for the $11.2\,M_\odot$ model s11 in Wanajo et al. (2018). It is more strongly peaked around 0.5 and has steeper and less extended left and right wings. In particular, considerably less matter with neutron excess is ejected, and the minimal Y_e is around 0.46 instead of $\lesssim 0.40$. The reason for this difference are the lower velocities with which the neutrino-heated ejecta expand outward from the gain radius. This slower expansion allows ν_e-absorption to lift Y_e from its low initial values at the gain radius to values closer to 0.5. Such conditions are less favorable for the production of neutron-rich trans-Fe species. The abundance pattern in the neutrino-processed ejecta of model s9.0 must be expected to show similarities with model s11 of Wanajo et al. (2018). A detailed investigation of the formation of chemical elements in s9.0 in comparison to z9.6 is deferred to future work.

4.5   Elemental distribution shortly after shock revival

In order to assess the strength of physical mixing due to multidimensional hydrodynamical flows during the first seconds in our 3D models, we present in Figure 11 normalized mass distributions for selected chemical elements behind the shock radius as functions of velocity (top panels) and mass coordinate (lower panels). To sample the velocity space, we choose 50 bins between the maximal and minimal velocities within the considered region. We use 30 bins to sample the distribution in the mass coordinate. The total masses in the postshock volume at the time $t_{\rm map}$ when we map our models onto the new computational grid for the long-time simulations are listed in Table 5.

The quasi-spherical explosion of model e8.8 manifests itself also in the distribution of the chemical elements over mass and velocity coordinates, since the initial shell structure of the progenitor is essentially preserved. Because of the extreme shock acceleration in the steep density gradient at the edge of the degenerate core, most material of the thin carbon shell of the progenitor travels with $\gtrsim 30,000$–$70,000\,{\rm km\,s^{-1}}$ ahead of the outer mass shells of the former ONeMg-core, which propagate with up to $\sim 60,000\,{\rm km\,s^{-1}}$. Most of the newly synthesized iron-group and α-nuclei expand with velocities below $\sim 30,000\,{\rm km\,s^{-1}}$. Inefficient mixing also confines the neutrino-heated ejecta within $M(r) \leq 1.338\,M_\odot$.

Slightly more powerful convective overturn in model z9.6 leads to more efficient mixing in mass and velocity space (see middle panels of Figure 11). Therefore some neutrino-heated material gets mixed into the carbon and oxygen shells and travels at more than $\gtrsim 20,000\,{\rm km\,s^{-1}}$. The bulk of the metal-rich ejecta still expands with slower velocities, however. Similar to model e8.8, the deceleration of the SN shock at the CO/He interface in model z9.6 also compresses parts of the ejecta into a dense shell. Model s9.0, again, differs distinctively from the ECSN-like models. Strong and long-lasting convective overturn in the postshock layer completely erases the initial onion-shell structure of the progenitor. The chemical ele-

ments become nearly homogenously mixed over mass and velocity coordinates (see right panels of Figure 11). The fastest neutrino-heated ejecta are associated with a big high-entropy plume inducing a dipolar deformation of the shock wave, which can be seen in Figure 7.

5   EVOLUTION BEYOND SHOCK BREAKOUT

5.1   Linear stability analysis

As mentioned already, the velocity of the forward shock depends on the progenitor structure, in particular the ρr^3-profile. According to Sedov et al. (1961) one expects an increase/decrease in the shock velocity when the gradient of the ρr^3-profile is negative/positive. This acceleration and deceleration lead to density and pressure gradients in the post-shock region with opposite signs. Thus, perturbations in the matter distribution become unstable to the Rayleigh-Taylor (RT) instability (Rayleigh 1882; Chevalier & Klein 1978). As the ρr^3-profiles, and hence the shock speed, vary significantly between the progenitors, the growth of RT instabilities will affect the long-time evolution of our models in different ways.

In order to aid us with the interpretation of our three-dimensional simulations, we appeal to 1D long-time simulations which are started from angle-averaged states of the 3D explosion models at the same times as given in Table 3. The numerical and physical setup for the spherically symmetric simulations remains unchanged compared to the 3D runs. The 1D models can teach us about the behavior of the shock, while it propagates through the envelope. Additionally, we can compute the linear RT growth rates $\sigma_{\rm RT}$ of small initial perturbations by tracking Lagrangian mass coordinates in our 1D simulations, following Müller et al. (1991a). In the incompressible case the growth rate is given by

$$\sigma_{\rm RT,incmp} = \sqrt{-\frac{p}{\rho}\frac{\partial \ln p}{\partial r}\frac{\partial \ln \rho}{\partial r}}, \tag{5}$$

where p and ρ are the pressure and density. In the compressible case the growth rate becomes

$$\sigma_{\rm RT,cmp} = \frac{c_s}{\gamma}\sqrt{\left(\frac{\partial \ln p}{\partial r}\right)^2 - \gamma\frac{\partial \ln p}{\partial r}\frac{\partial \ln \rho}{\partial r}}, \tag{6}$$

where c_s is the speed of sound and γ the adiabatic index. Equation (6) is less restrictive than its incompressible counterpart[9]. For the time-dependent amplification factor of an initial perturbation ξ_0 we integrate Equation (6) according to

$$\Sigma_{\rm RT}(t) = \frac{\xi}{\xi_0}(t) = \exp\left(\int_0^t \sigma_{\rm RT}(t')dt'\right). \tag{7}$$

This analysis enables us to estimate the time and locations in mass coordinate where the fluid becomes unstable to the RT instability, helping us to understand the origin of outward/inward mixing of different layers of chemical elements.

In Figure 12 we show the amplification factors in the incompressible (colored lines) and compressible (gray line) cases for our spherically symmetric simulations. Significant differences between the models are evident.

The left panel of Figure 12 shows the integrated growth rate

---

[9] Note that we are interested in the locations of maximal growth but not in the actual values. Calculating the growth factors from multidimensional models using angle averaged-values gives similar overall structure but lower amplitudes (Müller et al. 2018).
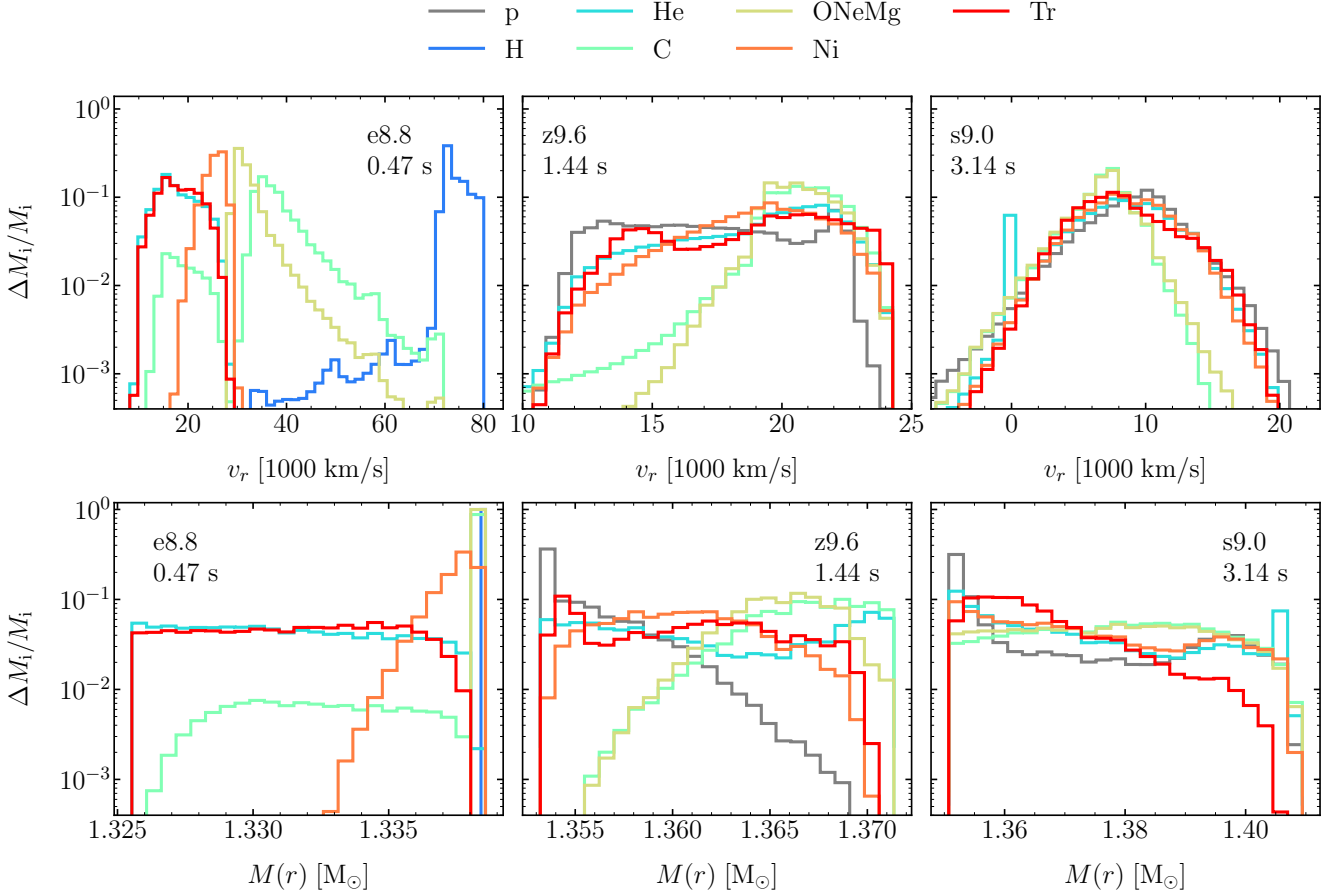
Figure 11. Normalized binned distributions of chemical elements as functions of radial velocity (top panels) and enclosed mass (bottom panels) for all of the unbound postshock material in our 3D models at t_{map} (see Table 3). We use 50 bins in velocity space and 30 bins in the mass coordinate, and the normalization for each species employs the total unbound mass behind the shock. The mass coordinate in the 3D models is defined by the mass enclosed by given radius and starts at the mass value contained by the PNS. Note that according to Table 5 only model e8.8 contains a small amount of hydrogen from the envelope in the postshock region at t_{map}.

of the 1D version of model e8.8$_{10}$. The extreme deceleration of the forward shock when moving into the hydrogen envelope induces very high growth factors at $M(r) \sim 1.34\,\mathrm{M_\odot}$. The ECSN-like structure of model z9.6 is reflected in its amplification factors. Strong deceleration of the forward shock at the CO/He interface creates the necessary condition for the RT instability to grow there. As can be seen in Figure 12, the amplification factors at $\sim 1.37\,\mathrm{M_\odot}$ reach extremely high values as observed in the ECSN case, too. Interestingly, no growth is expected at the He/H interface, which is a consequence of the tiny step in the ρr^3 profile at this interface (see Figure 1, bottom left panel, blue curve, at $r \approx 10^{12}$ cm).

Model s9.0 shows striking differences to the models described above. Due to its more shallow ρr^3-profile in the core region and the consequently weaker episodes of shock deceleration and acceleration, the peak amplitudes of the growth factors are smaller. They are, however, of similar magnitude as in the more massive models investigated by Wongwathanarat et al. (2015). Two distinct regions of instability can be discerned around the CO/He and He/H interfaces. Similar to the RSGs presented in Wongwathanarat et al. (2015), the strongest contribution arises from the He/H interface followed by the CO/He interface, where the amplification factors are about 10 orders of magnitude lower.

While the compressible and incompressible analyses give similar results for models e8.8 and z9.6, the compressible evaluation of the growth factors in model s9.0 predicts additional growth within the He-shell of the star. This is caused by the passage of the reverse shock at later times ($t_{\mathrm{pb}} > 3 \times 10^3$ s). Note, however, that at this advanced stage of evolution the instability is already in a strongly non-linear regime, where Equation (6) loses its validity.

5.2 Propagation of the supernova shock

In Figure 13 we show the angle-averaged shock radii R_{sh}, reverse-shock radii R_{rsh} and shock velocities v_{sh} for our 3D long-time simulations.

5.2.1 3D model e8.8

In model e8.8 the forward shock has passed the He/H interface and is traveling through the H-envelope. It left the core with about $100,000$ km s^{-1} and is progressively decelerated due to the monotonically increasing ρr^3 within the H-envelope (see also Figure 4). Since the innermost neutrino-heated ejecta are not in sonic contact
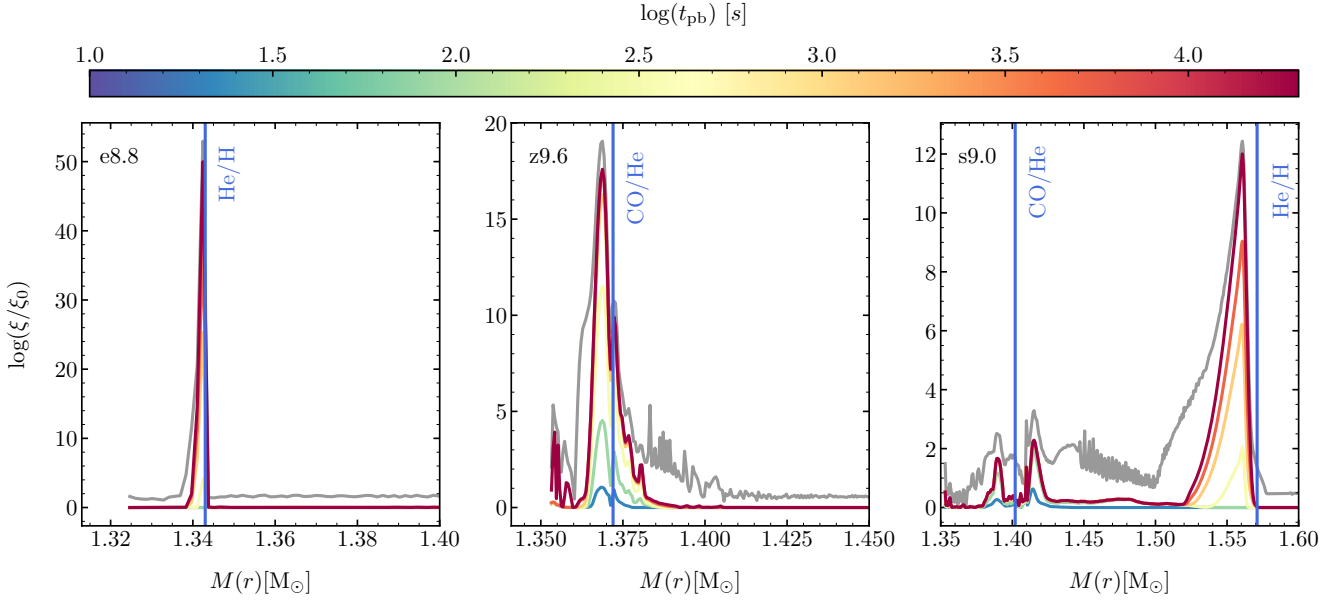
Figure 12. Integrated growth rates for RT instability for all considered models at different times evaluated with Equation (7) for the incompressible case (colored lines). The different composition interfaces of the progenitors are indicated by vertical blue lines. The gray line denotes the growth factor in the compressible case at $t = 10^4$ s. The different progenitor structures have a large impact on the estimated growth factor as can be seen most prominently by comparing models z9.6 and s9.0. While the ECSN-like progenitors develop only a narrow region of instability around the interface with the steepest density gradient (e.g. He/H for model e8.8 and CO/He for model z9.6), model s9.0 shows two distinct regions of high growth factor around the CO/He and the He/H interfaces.

with the SN shock, they do not feel the deceleration and thus travel with constant velocity of $\approx 35,000$ km s^{-1} until they catch up with the immediate post-shock matter at $t_{pb} \approx 130$ s. The interaction of the fast neutrino-heated ejecta with the post-shock material keeps the shock at slightly higher velocities (see small kink at $r \sim 10^7$ km, lower left panel in Figure 13). Nevertheless, the forward shock decelerates continuously (without relevant phases of acceleration) until it reaches the surface of the star. Note the dramatic deceleration of the shock from its initial velocity of $75,000$ km s^{-1} at $t_{pb} = 2.55$ s down to <1000 km s^{-1} when it leaves the star. A large fraction ($\sim 75\%$) of the kinetic energy of the shock wave is used up for heating the hydrogen in the outer layers of the envelope, leaving only around 2.5×10^{49} erg of kinetic energy in the ejecta.

The early strong deceleration of the forward shock at the bottom of the H-envelope at $t_{pb} \gtrsim 0.25$ s (see also Figure 4) leads to the compression of the CO and He layers into a high density shell. Less than 1 s later, a strong reverse shock forms at the base of this shell as the forward shock is progressively slowed down. The dense shell separates the postshock material from the neutrino-heated wind ejecta, which can be seen in the density profiles shown in Figure 14. It is remarkable that in the ECSN the neutrino-heated ejecta are denser than the postshock shell of the matter swept up by the shock in the H-envelope. The formation of the dense shell or "wall" (Kifonidis et al. 2006) has important consequences for the evolution of the metal-rich ejecta as well as for the growth of Rayleigh-Taylor instabilities. After $t_{pb} \approx 1$ h, continuous deceleration of the forward shock causes the reverse shock to travel back in mass coordinate (see Figure 14). It takes, however, a total of approximately ~ 9 h for the reverse shock to reach the inner boundary of our computational domain in model e8.8 (Figure 13).

5.2.2 3D model z9.6

In model z9.6 the forward shock has already crossed the CO/He interface at t_{map} (see Table 1) and is traveling at roughly $27,000$ km s^{-1}. Behind the shock, a dense shell has formed due to the deceleration of the fast neutrino-driven wind in a wind-termination shock (Figure 14). In between the shocks, the high density peak atop the bulk of the ejecta is formed by the deceleration of the forward shock at the CO/He interface. Outside of the CO/He interface, with similarity to model e8.8, a featureless density profile in the He-core and hydrogen envelope leads to an untroubled but gradually decelerated expansion of the forward shock, which reaches the stellar surface at around $t_{pb} \approx 1.3$ d. At the time of shock breakout the forward shock propagates only at ~ 2000 km s^{-1} because of its strong deceleration in the hydrogen envelope of the star. Different from the ECSN progenitor, the wind-termination shock moves inward at $t_{pb} \approx 10$–15 s (see Figure 14) to get reflected at the center before $t_{pb} \approx 40$ s. A second reverse shock forms within the He-core of the star and propagates back in radius after ~ 400 s to reach the inner boundary at $t_{pb} \approx 800$ s (Figure 13), which is more than 8 hours earlier than in model e8.8.

5.2.3 3D model s9.0

For the 3D simulation of model s9.0 the trajectories of the forward and reverse shocks are shown in the right panels of Figure 13. The long-time simulation is initiated at $t_{pb} = 3.14$ s, when the forward shock has just crossed the CO/He interface and is traveling at $v_{sh} \approx 11,000$ km s^{-1}, only a fraction of the shock velocity found in the ECSN-like models. Acceleration and deceleration of the SN shock at the CO/He interface cause the formation of a dense shell in the post-shock region (see Figure 14). The density contrast be-
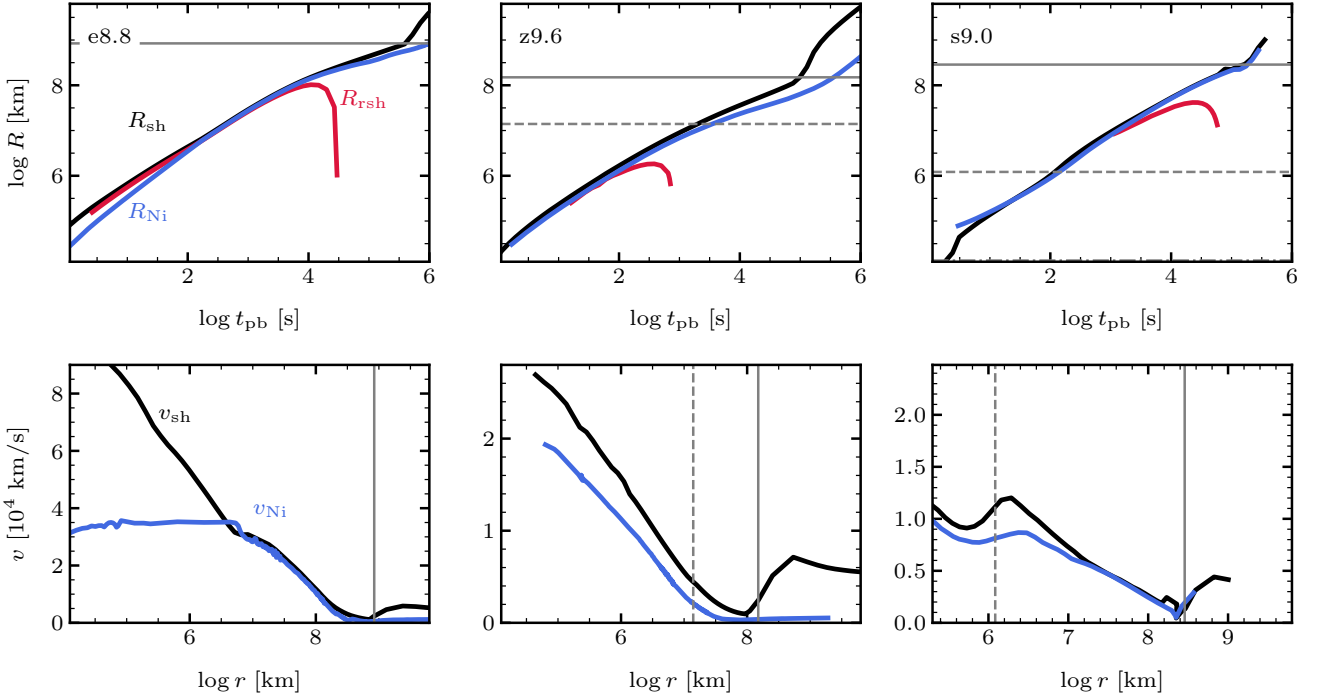
Figure 13. *Upper panels*: Angle-averaged shock radius R_{sh} (black), angle-averaged reverse shock radius R_{rsh} (red) and maximum radius of the iso-surface of mass fraction $X_{^{56}Ni+Tr} = 0.03$ (blue). *Lower panels*: Average shock velocity v_{sh} (black) and maximum velocity of the iso-surface of $X_{^{56}Ni+Tr} = 0.03$ (blue) in our 3D long-time simulations. The horizontal or vertical gray dashed and solid lines mark the location of the He/H interface and the surface of the progenitor star, respectively. The expansion of the forward shock in the ECSN-like progenitors proceeds with continuous deceleration nearly until the shock reaches the stellar surface. In contrast, the forward shock in model s9.0 accelerates strongly around the He/H interface. The reverse shocks in models e8.8 and z9.6 form within ≈1 s and ≈100 s, respectively, whereas we witness the formation of a reverse shock from the He/H interface in model s9.0 at ≈2500 s. Note that in model s9.0 the velocity of the fastest clump containing $^{56}Ni+Tr$ is higher than the average shock velocity within the hydrogen envelope of the star.
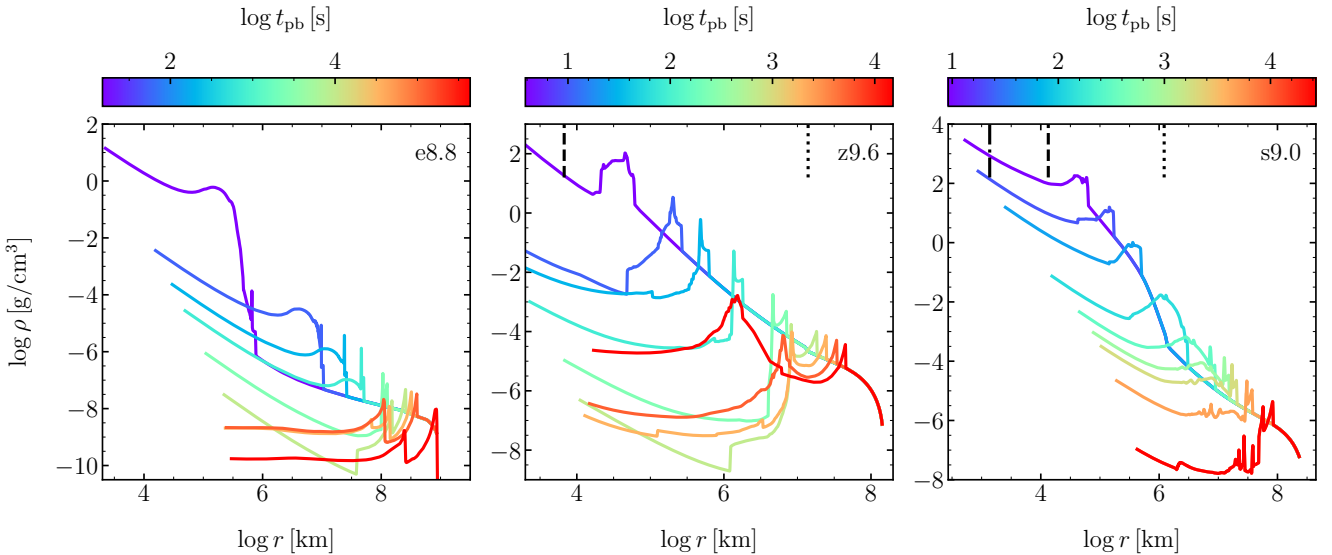
Figure 14. Radial profiles of the density of our 1D long-time simulations at representative times. The dash-dotted, dashed and dotted vertical black lines represent the outer boundaries of the degenerate core, CO, and He cores, respectively. See text for discussion.

tween the shell and the ejecta is, however, around one order of magnitude smaller than found for the dense shells that formed at the core/envelope boundary in model e8.8, and at the CO/He interface in model z9.6. In the following, the shock slows down to $v_{sh} \approx 7,500 \, km \, s^{-1}$ within the He-core of the star, before it accelerates again around the He/H composition interface, reaching $v_{sh} \approx 11,500 \, km \, s^{-1}$. This is due to the steep density gradient just below the He/H interface in the progenitor. Thereafter, the forward shock encounters the increasing ρr^3 in the hydrogen envelope and is thereby strongly decelerated, causing a compression of the post-shock material into a double-peaked dense shell. At the bottom of the hydrogen shell, a strong reverse shock forms shortly afterwards (see Figures 13 and 14). Note that the formation of this reverse shock from the He/H interface occurs much later than witnessed in the ECSN-like progenitors. Eventually the reverse shock reaches the inner boundary of our numerical grid at $t_{pb} \approx 16 \, h$. A first reverse shock from the CO/He interface had formed around $t_{pb} \approx 30 \, s$ (Figure 14), but was swept outward with the expanding ejecta. The main, spherically shaped SN shock encounters the stellar surface at $t_{pb} \approx 2.8 \, d$, whereas the maximum radius of the shock, pushed by a giant, nickel-rich bubble, reaches the surface already at $t_{pb} \approx 2.1 \, d$ (see discussion in Section 5.3 and Figures 21 and 22).

5.3   Morphology of neutrino-heated ejecta

In the following we focus on the long-time development of the early-time asymmetries which we trace by the propagation of the neutrino-heated ejecta or more specifically the ^{56}Ni+Tr-rich material. Kifonidis et al. (2003) already noted that ^{56}Ni is produced between the high-entropy bubbles that expand due to strong neutrino-heating from below. Thus the distribution of ^{56}Ni traces the asymmetries that developed during the onset of the explosion.

5.3.1   3D model e8.8

In Figure 15 we show slices of the ^{56}Ni+Tr mass fraction of the 3D simulation of model e8.8. The dashed white line indicates the shock radius, whereas the thin dotted black line indicates the position where the enclosed mass equals the mass interior to the He/H interface in the progenitor.

As in the 1D simulation, the CO and He layers are compressed into a dense shell just behind the SN shock at a radius of $\approx 5 \times 10^5$ km at $t_{pb} = 9 \, s$ (see Figure 14 and Figure 16). Already at $t_{pb} \approx 1.5 \, s$, a reverse shock begins to form at the bottom of this dense shell (see the sharp inner edge of the light-blue, narrow ring at 5×10^5 km in Figure 16 at 9 s) . By this time the bulk of the neutrino-heated ejecta has expanded in the volume inside $\approx 3 \times 10^5$ km. While this innermost metal-rich material seems to expand in a basically self-similar fashion (see similarity of the snapshots until $t_{pb} = 150 \, s$ in Figure 15), the growth of the RT instability in small protrusions at the unstable contact interface near the outer edge of the dense shell begins to corrugate the surface of the (^{56}Ni+Tr)-rich ejecta. At $t_{pb} = 300 \, s$, the neutrino-heated ejecta of ^{56}Ni +Tr catch up with the expanding dense shell and are strongly decelerated. RT plumes become clearly visible near the He/H interface first at about 1400 s in Figure 15.

As a consequence, the higher entropy/lower density bubbles are compressed to flat structures, whereas the higher-density regions in between the bubbles are able to penetrate the dense shell, thereby inducing perturbations at the He/H interface. These RT plumes grow over the following hours around the mass shell of the He/H

interface, mixing clumps of ^{56}Ni from the central volume outward into the carbon and helium rich layers.

The reverse shock, which is visible at $t_{pb} = 2.3 \, h$ in Figure 16 as the yellow to blue discontinuity, begins to propagate back in radius, thereby compressing the innermost ejecta. At $t_{pb} \approx 10 \, h$ the inward passage of the reverse shock and the growth of the RT instability has erased the initial structures present at the onset of the explosion. However, the overall morphology of the neutrino-heated ejecta is still basically spherical with only small-scale asymmetries (see also Figure 17).

5.3.2   3D model z9.6

In Figure 18, we show slices of the ^{56}Ni+Tr mass fraction in the 3D simulation of model z9.6. The dashed white line marks the shock radius, while the dotted lines indicate the positions where the enclosed mass equals the mass interior to the CO/He and He/H interfaces of the progenitor. The dense shell that forms after the forward shock has crossed the CO/He interface (see Figure 14) is visible as the circular dark-red region at $\sim 1.5 \times 10^5$ km after 9 s in Figure 19. At that time the termination shock of the neutrino-driven wind can be seen at about 5×10^4 km, moving inward.

Within the first $\approx 9 \, s$ the fastest of the neutrino-heated ejecta encounter this dense CO-rich shell (see Figure 19) and are compressed and squeezed to flat structures around 30 s later. Similar to the results presented for the e8.8 model, the slightly over-dense regions between the high-entropy plumes induce long-wavelength perturbations as they deform and try to penetrate the RT unstable dense shell. Over the next few minutes, RT fingers grow on top of these deformations and fragment the dense shell into numerous ^{56}Ni-rich shrapnels.

While the fingers grow progressively, the second reverse shock from the shock propagation through the He layer (visible as the green to yellow discontinuity at $t_{pb} = 187 \, s$ in Figure 19) begins to propagate back in radius. At $t_{pb} = 829 \, s$ the reverse shock has almost reached the center of our numerical grid, having compressed and decelerated the innermost ejecta material. At $t_{pb} = 1.7 \, h$, the forward shock has crossed the He/H interface and the inner material has been fully shredded by the instability.

As the shock velocity does not change significantly at the He/H interface, we observe no additional growth of the RT instability nor the formation of another reverse shock. Thus, the morphology of the innermost ejecta seems to be determined early on, already before the shock crosses the He/H interface.

Comparing the distribution of ^{56}Ni and Tr of model e8.8 (Figure 15; $t_{pb} = 4.7 \, d$) and model z9.6 (Figure 18; $t_{pb} = 1.3 \, d$) shortly before shock breakout, we find a slightly more clumped morphology in the 9.6 $M_\odot$ progenitor. The structure of the neutrino-heated ejecta in model z9.6 also remains fairly spherical with many small-scale clumps (see Figures 19 and 20). However, different from model e8.8 one can recognize a hemispheric asymmetry with bigger plumes between the 8 o'clock and 10 o'clock positions in Figure 18 and weaker plumes in the opposite hemisphere. These aspherical structures go back to asymmetries that existed already in the first seconds of the explosion, visible by larger RT mushrooms and a slightly stronger shock expansion in the left hemisphere at $t_{pb} = 2 \, s$. The strongest plume sticks out near the 11 o'clock position in Figure 20.

5.3.3   3D model s9.0

The evolution of the neutrino-heated ejecta in model s9.0 proceeds drastically differently from the ECSN-like progenitors (Figures 21–
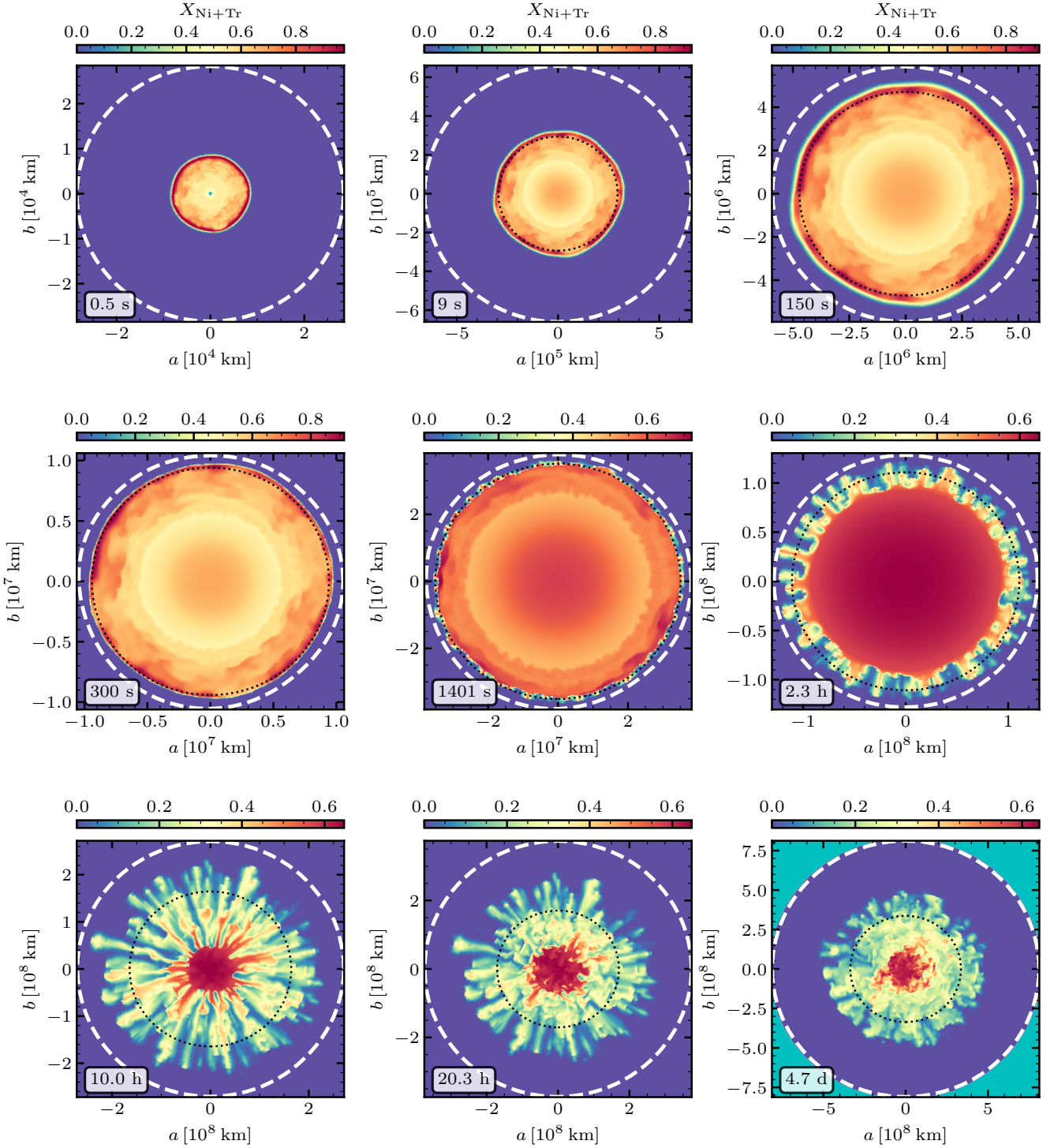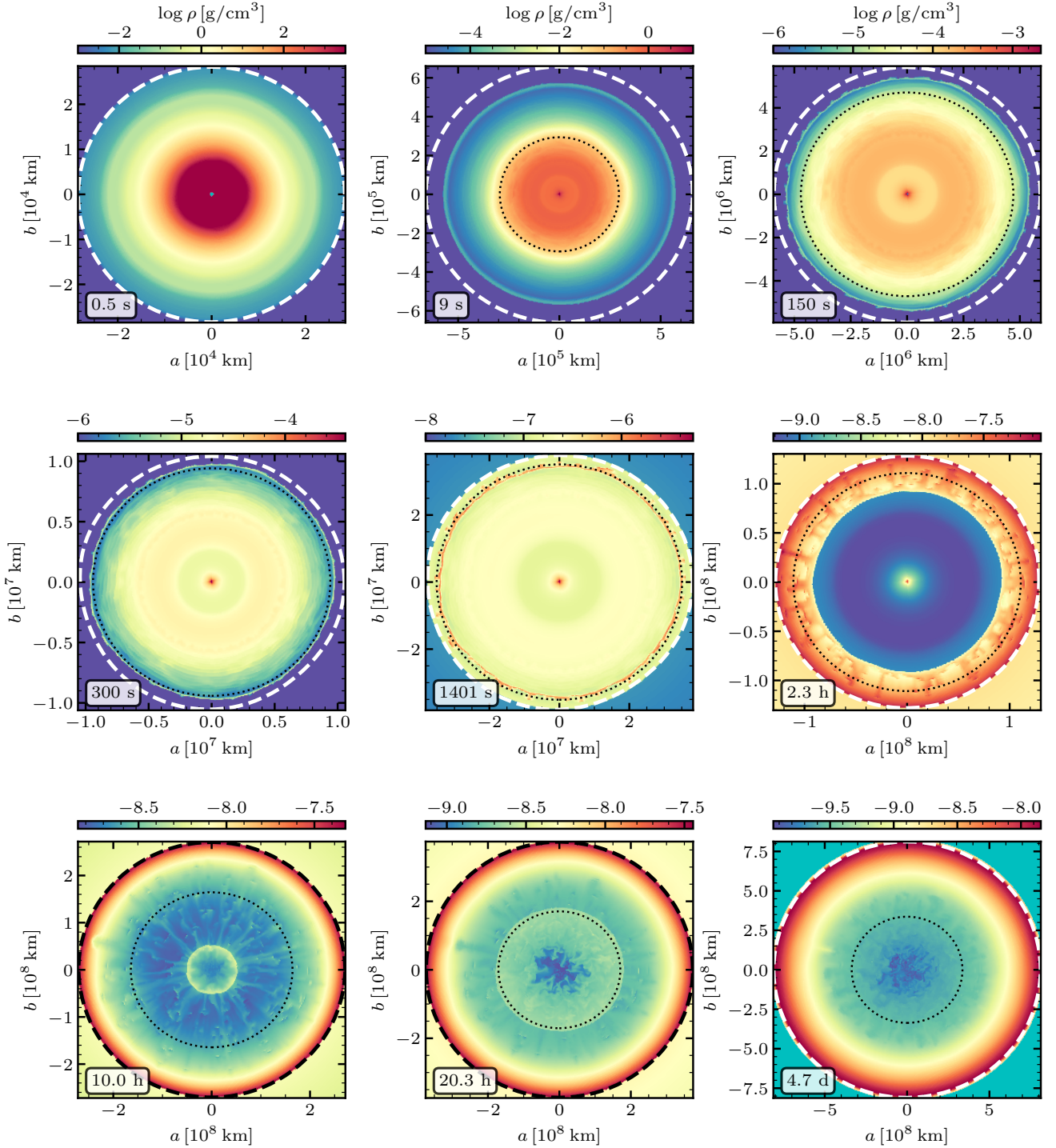
Figure 15. Slices showing the ^{56}Ni+Tr mass fraction in the 3D simulation of model e8.8. The dashed white line indicates the position of the SN shock and the dotted black line marks the radial location where the enclosed mass is equal to the mass coordinate of the He/H shell interface of the progenitor. Cyan colored regions in the bottom right panel represent the surrounding medium embedding the progenitor. Until ≈150 s the neutrino-heated ejecta expand essentially self-similarly. This untroubled expansion ends at about 300 s, when the material is decelerated in a dense postshock shell (see Figure 14). At ≈1400 s the growing RT instability at the He/H interface begins to affect the outer layers of the neutrino-heated ejecta. From roughly 2 h on the plumes grow in size, while the reverse shock (visible at the base of the plumes) begins to propagate back in radius (see Figure 13). About 9 h after bounce the reverse shock reaches the center, gets reflected there, and on the way compresses the metal-rich ejecta in the central region. Note that the plumes are almost evenly distributed in angular direction and radial extent.

Figure 16. Slices showing the density distribution in the 3D simulation of model e8.8. The dashed white or black line indicates the position of the SN shock and the dotted white or black line marks the radial location where the enclosed mass is equal to the mass coordinate of the He/H shell interface of the progenitor. Cyan colored regions in the lower right panel represent the surrounding medium embedding the progenitor. The dense shell at which the reverse shock will form (see also Figure 15) is first visible as the light yellow ring with a radius of about $\approx 3 \times 10^5$ km at $t_{pb} = 9$ s. The panel at $t_{pb} = 2.3$ h shows the formation of small RT fingers. These fingers grow with time and partly take up the neutrino-heated material (see panels at $t_{pb} \approx 2.3$ h and $t_{pb} \approx 10$ h). At $t_{pb} \approx 4.7$ d the innermost ejecta are characterized by an overall spherical shape, superimposed with the relics of the RT fingers. The reverse shock is very prominent at $t_{pb} \approx 2.3$ h and travels inward from about 3 h on (see Figure 13). It reaches the center at $t_{pb} \approx 9$ h to be reflected outward again (see lower left panel).
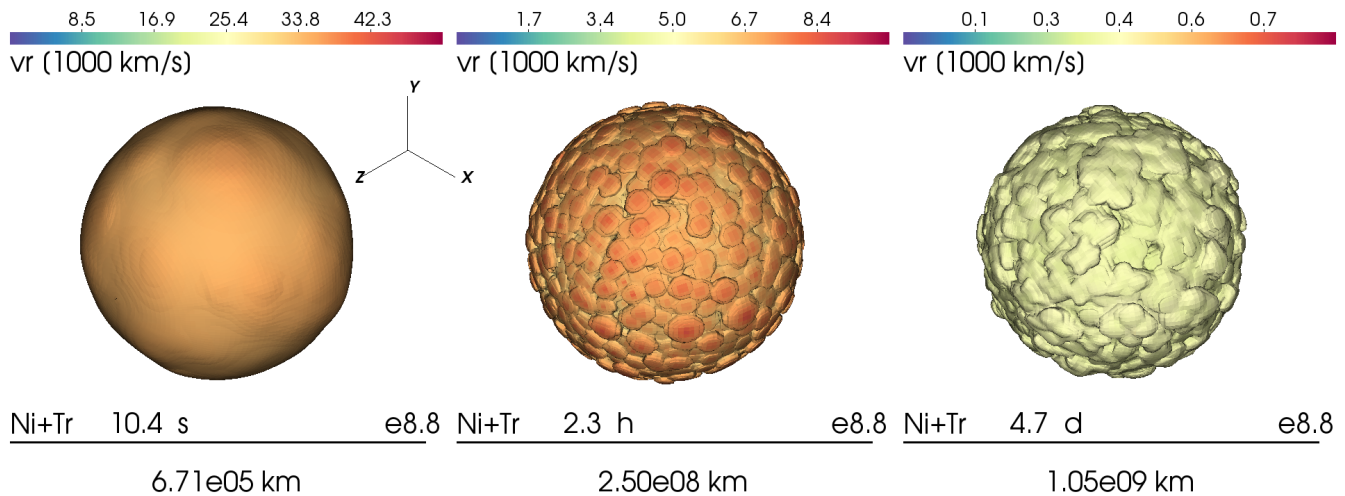
Figure 17. 3D renderings of the $X_{^{56}\mathrm{Ni+Tr}} = 0.03$ iso-surface of model e8.8 at the indicated times. The black lines indicate the radial scales of the plots. The color-coding represents the radial velocity of the material and the tripod in the left panel indicates the orientation of the global coordinate system. From the initially quasi-spherical distribution of the neutrino-heated ejecta with only low-amplitude perturbations we observe the growth of small-scale RT plumes. Because of the nearly spherical beginning of the explosion and the growth of RT instabilities only on small angular scales, the final distribution of the neutrino-heated ejecta is basically isotropic.

23). As discussed in Section 4, the initial asymmetries and shock deformation seen in model s9.0 are considerably larger than found in the ECSN-like models. Strong convection leads to the formation of a large high-entropy plume, which is rich in iron-group material and expands about two times faster than the surrounding material at the time of shock revival ($t_{\mathrm{pb}} \approx 0.5\,\mathrm{s}$). It crosses the CO/He interface of the star at $t_{\mathrm{pb}} \approx 1.3\,\mathrm{s}$, shortly after the forward shock. In comparison, the slowest moving material reaches the interface around 0.65 s later.

The crossing of the CO/He interface by the shock wave has several dynamical consequences. Due to the increasing ρr^3 outside of the interface, the shock is decelerated and the postshock matter is swept up and compressed into a dense shell. Note that the neutrino wind in this model is very weak and, different from model z9.6, there is no low-density central region and no wind termination shock. Instead, the central volume around the NS contains relics of ($^{56}\mathrm{Ni}$ +Tr)-rich low-density plumes and $^{56}\mathrm{Ni}$-poor, higher density downflows during the entire evolution.

The high-density shell behind the shock is aspherical in contrast to the shells found in the ECSN-like progenitors, which is also reflected by the still deformed SN shock (see first two panels in Figure 22 for $t_{\mathrm{pb}} = 3$ and 124 s). Around the dense shell we observe the growth of large plumes, which stem from the initial asymmetries of the explosion. These can be seen in the 10 o'clock direction in Figure 21 at $t_{\mathrm{pb}} = 124\,\mathrm{s}$ and in Figure 23. At the tops of these plumes small RT fingers grow, in line with the analysis of the amplification factors presented in Section 5.1. Note that at this point in time the still deformed SN shock crosses the He/H interface (see Table 1 and Figure 13).

Due to the varying ρr^3 profile around this composition interface, the shock accelerates and decelerates, thereby forming a dense shell (see the yellow-green ring in Figure 22 at $t_{\mathrm{pb}} = 742\,\mathrm{s}$ and the density spike in Figure 14). When the fast and dense metal-rich plume encounters the shell, it induces a high-amplitude perturbation in this RT unstable layer. From this perturbation, aided by the large initial momentum of the metal-rich plume, we observe the growth of a large RT structure, which assists the further outward expansion of the $^{56}\mathrm{Ni}$+Tr material of the initial, big plume. As the

shock is decelerated in the H-envelope, the dense metal-rich plume retains higher velocities than the speed of the shock and thus the plume is able to deform the forward shock on its way (see Figure 22 at $t_{\mathrm{pb}} \geq 2.4\,\mathrm{h}$).

Concurrently, the reverse shock, which forms at the bottom of the He/H interface, propagates back into the ejecta and strongly decelerates and compresses the ($^{56}\mathrm{Ni}$+Tr)-rich material close to the center (see Figures 21 and 22 at $t_{\mathrm{pb}} \approx 7.8\,\mathrm{h}$), whereas the fastest, biggest plume escapes the most dramatic deceleration, although its velocity also shrinks with time (see Figure 23). The growing RT instability around the CO/He interface (clearly visible in Figure 22 at $t_{\mathrm{pb}} \approx 7.8\,\mathrm{h}$) seems to only slightly affect the outer boundary of the central ($^{56}\mathrm{Ni}$+Tr)-rich material, as can be seen in Figure 21 at $t_{\mathrm{pb}} \geq 7.8\,\mathrm{h}$ (in line with the small amplification factors found in this region).

Due to the strong deceleration of the innermost material, the fast plume almost fully detaches from the core material as it propagates through the hydrogen envelope of the star (see last two panels in Figures 21, 22, and 23). It encounters the surface of the star at around $t_{\mathrm{pb}} \approx 2.1\,\mathrm{d}$, so more than half a day earlier than the spherically shaped main shock front, which reaches the stellar surface at $t_{\mathrm{pb}} \approx 2.8\,\mathrm{d}$. Why is the large plume able to travel with such high velocities, even deforming the forward shock, while the bulk of the $^{56}\mathrm{Ni}$+Tr mass travels at considerably slower speed? First, the fastest $^{56}\mathrm{Ni}$+Tr material is, at all times, in close vicinity of the immediate postshock matter (see Figure 13). Second, after the forward shock has crossed the He/H interface, the Ni-rich plume is decelerated less than the average shock (see Figure 13), since this material is denser than its surroundings in the hydrogen layer. Third, large growth rates at the He/H interface lead to an efficient outward mixing of the dense plume within the unstable layers, and the plume can therefore also escape the strong deceleration by the reverse shock. As a consequence, the ($^{56}\mathrm{Ni}$+Tr)-rich plume catches up with the forward shock in the hydrogen envelope. Due to its large momentum it deforms the outgoing forward shock in its trajectory. This is similar to a transient situation at about half an hour and 3 h in model e8.8, where the neutrino-heated ejecta in RT plumes catch up with the
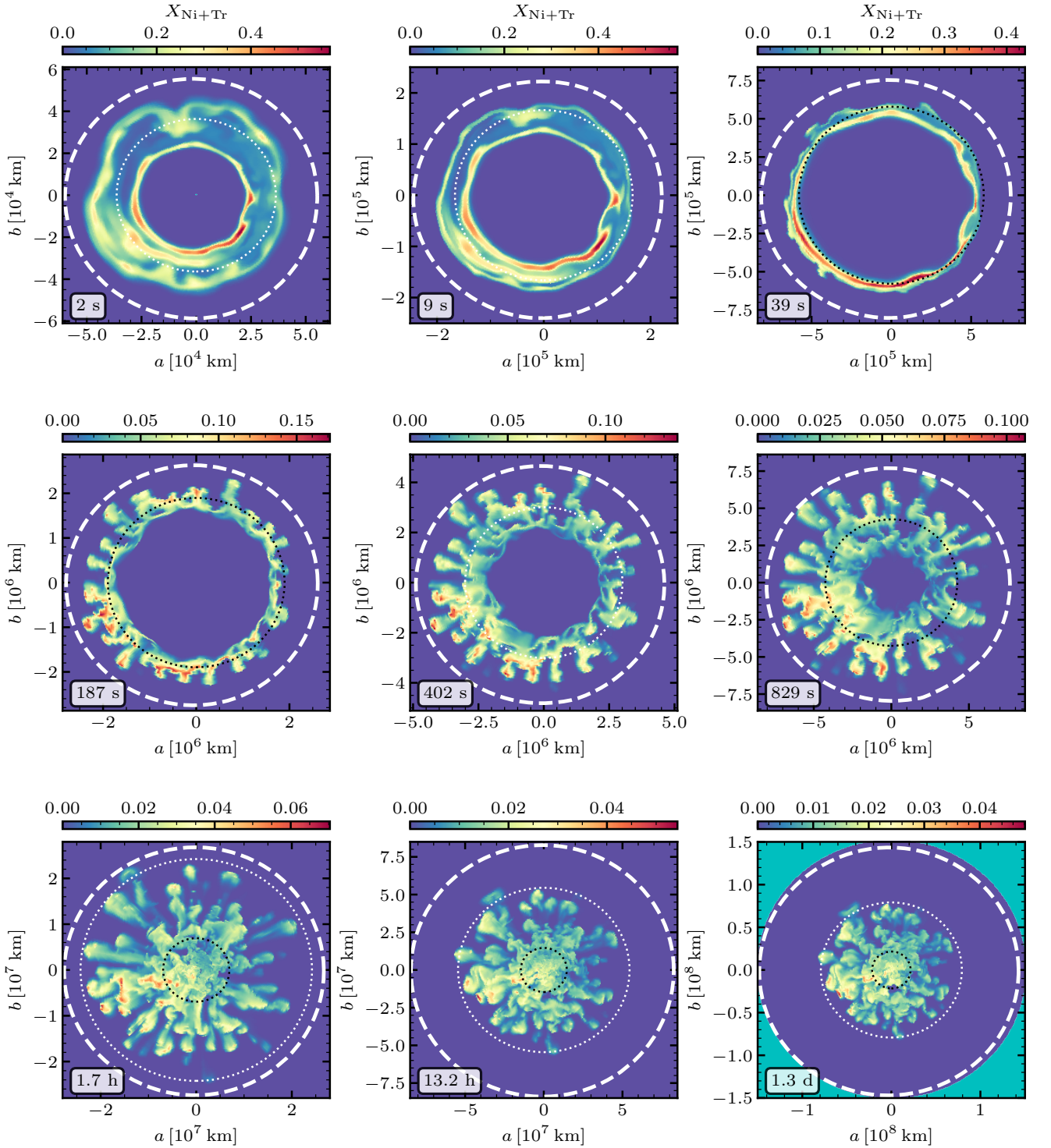
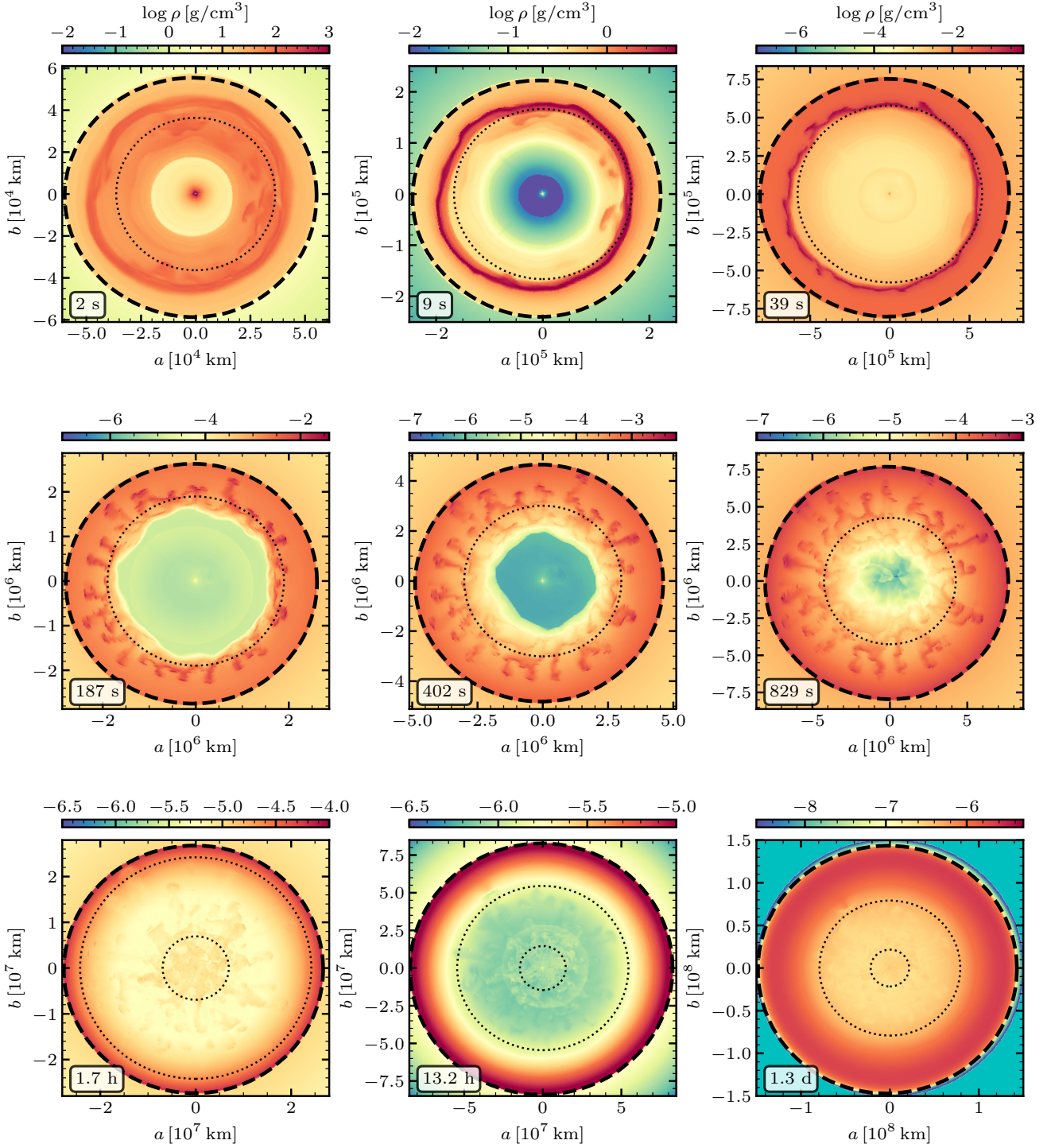**Figure 18.** Slices of the ^{56}Ni+Tr mass fraction of the 3D simulation of model z9.6 at the indicated times. Cyan colored regions in the bottom right panel represent the surrounding medium of the progenitor. The dashed white line marks the shock position, the dotted white or black lines indicate the radial locations where the enclosed mass equals the mass interior to the CO/He and He/H composition interfaces of the progenitor. The initial asymmetries that develop during the onset of the explosion are still visible at $t_{pb} = 1.5$ s, but they are soon compressed to flat structures as they collide with the RT unstable dense shell behind the CO/He interface (see times from $t_{pb} = 9$ s to $t_{pb} = 39$ s and also Figure 19). Over the next, roughly, one hour, the growing RT instability mixes the outer ^{56}Ni-rich layers outwards in mass coordinate in numerous small fingers. 1.7 h after bounce the RT instability has basically saturated and the first iron-rich clumps reach the He/H interface of the progenitor, where in model z9.6 no secondary RT instability occurs. The final morphology of the ^{56}Ni-rich ejecta has mostly lost any resemblance with the state at t_{map} and is dominated by small-scale asymmetries. However, the overall distribution of ^{56}Ni and Tr remains roughly spherical with many small-scale features and only a slight global deformation, which exhibits larger and stronger iron-rich plumes between the 8 o'clock and 10 o'clock directions and weaker structures in the opposite directions. A corresponding hemispheric asymmetry is already visible at the beginning of the explosion, see top left panel for $t_{pb} = 2$ s.

Figure 19. Slices showing the density in the 3D simulation of model z9.6 at the indicated times. Cyan colored regions in the bottom right panel represent the surrounding medium of the progenitor. The dashed black line marks the shock position, the dotted black lines indicate the radial locations where the enclosed mass equals the mass interior to the CO/He and He/H composition interfaces of the progenitor. A termination shock of the neutrino-driven wind is visible as the yellow/orange discontinuity at $t_{pb} \approx 2$ s. The shock deceleration in the He-layer leads to the formation of a dense shell that gets extremely compressed by the outward shock from the reflection of the wind termination shock at the center (see Figure 14). Over the next ≈ 100 s, RT plumes start to grow within the unstable layer between the two shocks, thereby fragmenting the dense shell. A second reverse shock forms when the SN shock propagates through the He-layer of the progenitor. As this reverse shock travels back in radius, similar to the results presented for model e8.8, the plumes grow to their maximal radial extent (see panels at $t_{pb} = 187$ s–829 s). The final morphology of the ejecta at $t_{pb} \approx 1.3$ d resembles the late-time morphology in model e8.8.
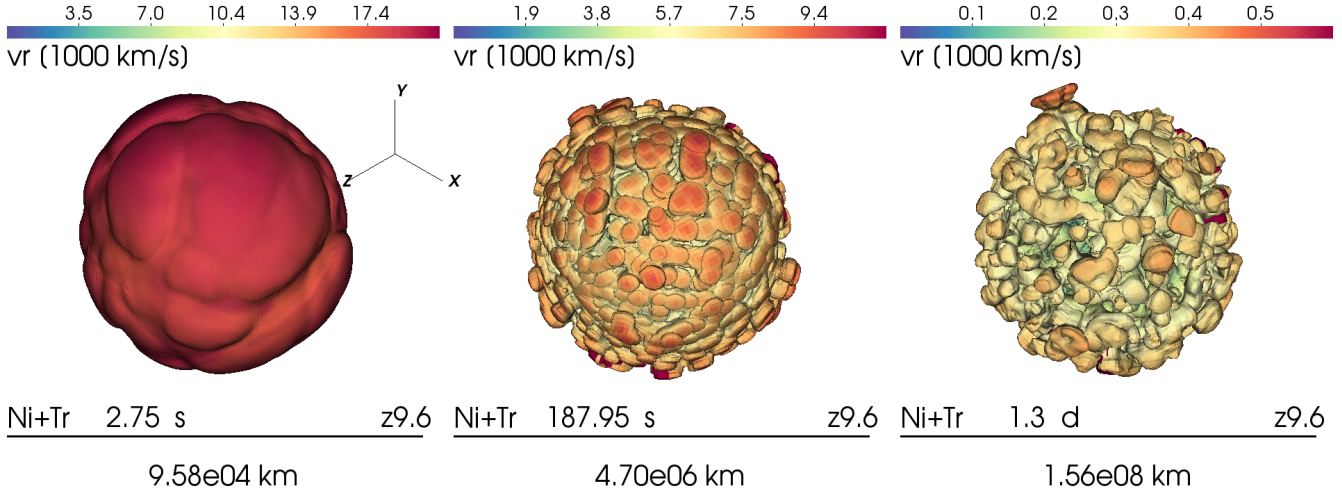
Figure 20. 3D renderings of the $X_{56\text{Ni}+\text{Tr}} = 0.03$ iso-surface of model z9.6 at the indicated times. The color-coding represents the radial velocity of the material, and the tripod in the left panel indicates the orientation of the global coordinate system. We find the growth of small-scale (high spherical harmonics mode numbers ℓ) RT plumes on top of the initial asymmetries of the explosion. The small amplitudes of the initial asymmetries and the narrow RT unstable layer prevent the growth of large global asymmetries, leaving the final state basically spherical. One initially bigger neutrino-heated bubble leads to a more extended plume near the 11 o'clock position in the right panel.

strongly decelerated immediate postshock material, thereby pushing the forward shock (see Figures 13 and 16).

5.4 Extent of mixing

In Figure 24, we display the normalized mass distributions of various nuclear species, including free protons from the freeze-out of NSE, hydrogen from the envelope, helium, carbon, oxygen-neon-magnesium, radioactive nickel, and the tracer nucleus of neutron-rich species for all of our models at the time of shock breakout as functions of radial velocity and mass coordinate (the latter is defined as enclosed mass $M(r)$ at radius r).

The distributions of the iron-group ejecta in the ECSN-like models (e8.8 and z9.6) have similar shapes in velocity and mass space (apart from the differences that result from the different initial progenitor composition). They are characterized by a maximum centred around 0.3×10^3 km s^{-1} and have a high-velocity tail which extends to $\sim 0.5 \times 10^3$ km s^{-1} (using $\Delta M_i / M_i = 8 \times 10^{-4}$ as a threshold value). The mixing in velocity space corresponds to mixing in mass coordinate to a maximum of $\sim 1.45 \, \mathrm{M}_\odot$ in model e8.8 and $\sim 1.95 \, \mathrm{M}_\odot$ in model z9.6, which corresponds to the bottom of the respective hydrogen envelope.

Thus, the mixing is more efficient in model z9.6 in comparison to model e8.8, although the explosion energy and the integrated growth factors are larger in the latter. Why is this the case? The answer can be found by inspecting Figures 15, 16 and 18, 19. Model z9.6 shows a larger asymmetry already at the onset of the explosion. Additionally, the density profile of the progenitor of model z9.6 exhibits less extreme declines outside of the Si/CO and CO/He interfaces than the sharp drop of the density at the edge of the degenerate core in the ECSN progenitor. This permits a shock expansion that is not quite as rapid as in model e8.8 (Figures 4 and 13). The initial asymmetry triggers more and faster growth of the RT instability at the CO/He interface in model z9.6 (see Figures 18, 19) on a time scale much shorter than the growth of the RT mushrooms in model e8.8. While in model z9.6 large RT plumes are visible

already at about 100 seconds after bounce, it takes a few hours for such structures to develop at the He/H interface of model e8.8 (see Figure 15). From this result we conclude that the extent of mixing during the SN blast is not only determined by the linear growth factors, but depends strongly on the initial explosion asymmetry seeding the growth of the RT instability at the unstable composition interfaces.

In contrast to the ECSN-like models, heavy elements are mixed to large mass coordinates and velocities in model s9.0. This is facilitated by the extreme initial asymmetries at the onset of the explosion. Fast metal-rich plumes arrive quickly at the He/H interface and trigger the RT instability there, thereby transporting a significant amount of the total ^{56}Ni+Tr mass to large mass coordinates into the H-envelope. Outward mixing of intermediate-mass elements is driven by the growth of the RT instability which causes a fragmentation of the dense shells that form after the forward shock crosses the CO/He and He/H interfaces. Most importantly, the biggest plume is able to transport ^{56}Ni+Tr-rich matter to large velocities and mass coordinates. It contains about 25% of the total ^{56}Ni+Tr mass at t_{map} and carries about half of that to radii well ahead of the average radius of the shock when it reaches the stellar surface. We find that about 4% of the ^{56}Ni+Tr-rich material travels with more than $1{,}000$ km s^{-1} and thus far ahead of the bulk of the metal-rich matter.

5.5 Long-time evolution of compact remnant properties

While the SN shock wave travels through the progenitor star, some material falls back onto the newly formed NS (e.g., Chevalier 1989; Woosley 1989; Zhang et al. 2008; Fryer 2009; Wong et al. 2014). This fallback is needed to explain the observed broad range of compact remnant masses (Zhang et al. 2008; Wong et al. 2014; Ertl et al. 2020). A first episode of fallback occurs when the neutrino-driven wind abates and the wind termination shock moves back towards the PNS (Arcones et al. 2007). This period happens at early times, roughly within ~ 10 s after bounce. At later times fallback is driven by the reverse shocks that originate from the acceleration
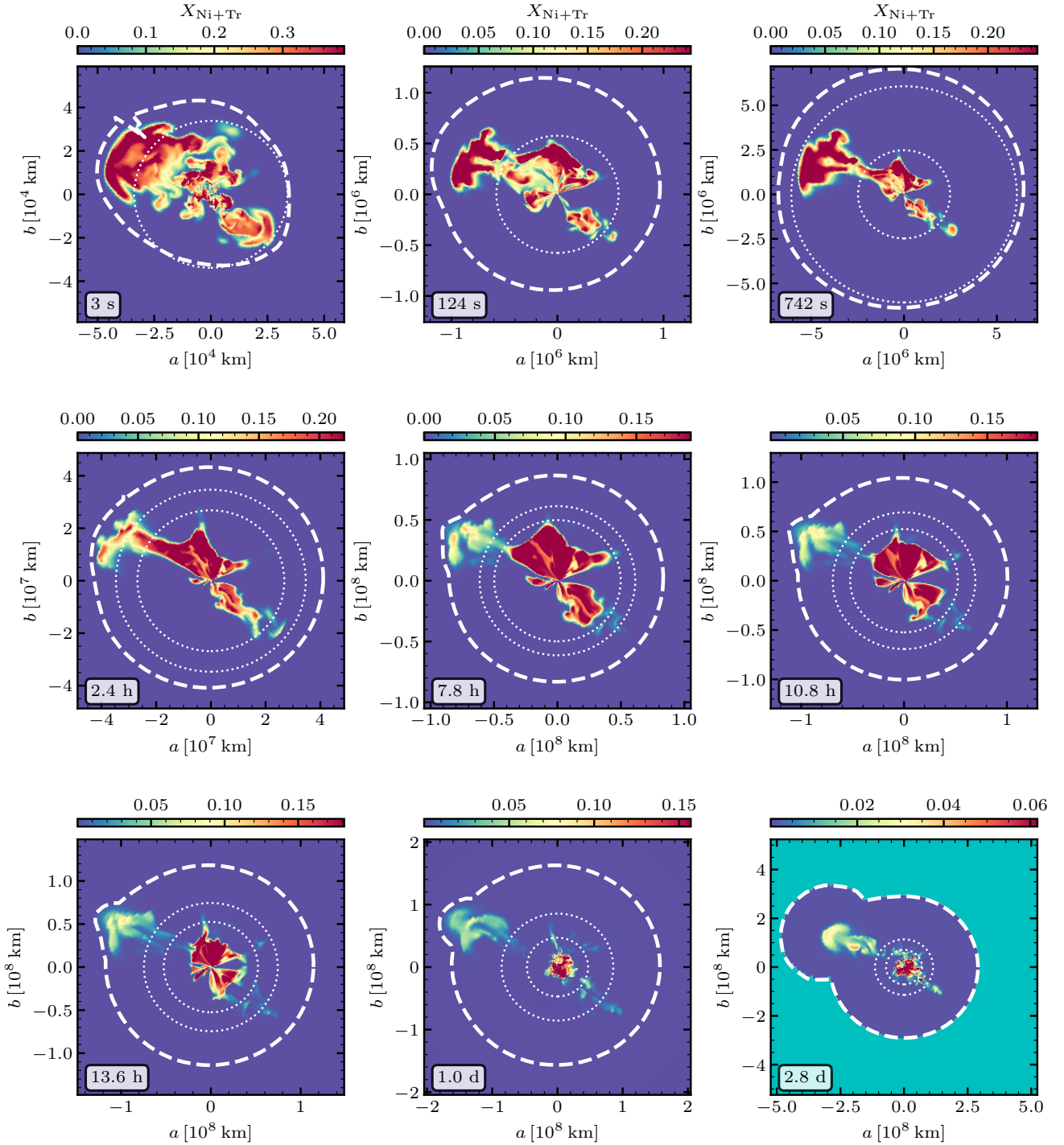
Figure 21. Slices of the ^{56}Ni+Tr mass fraction of model s9.0 at the indicated times. The dashed white line marks the shock surface, and the dotted white lines denote the positions where the enclosed mass equals the mass interior to the CO/He and He/H composition interfaces of the progenitor. The cyan colored region in the bottom right panel represents the surrounding medium of the progenitor. The ^{56}Ni+Tr distribution underlines the connection between the initial asymmetries, and the largest clump that overtakes the average shock even before shock breakout. At $t_{\rm pb} = 3$ s around 25% of the ^{56}Ni-rich material are ejected in the 10 o'clock direction. (The kink of the white dashed line for the shock surface at this time is a numerical artifact due to the shock-detection algorithm.) While the innermost ejecta are compressed and decelerated strongly by interaction with the dense shells and reverse shocks that form at the CO/He and He/H interfaces, about half of the large clump experiences less dramatic deceleration and deforms the otherwise spherical shock wave well before shock breakout.
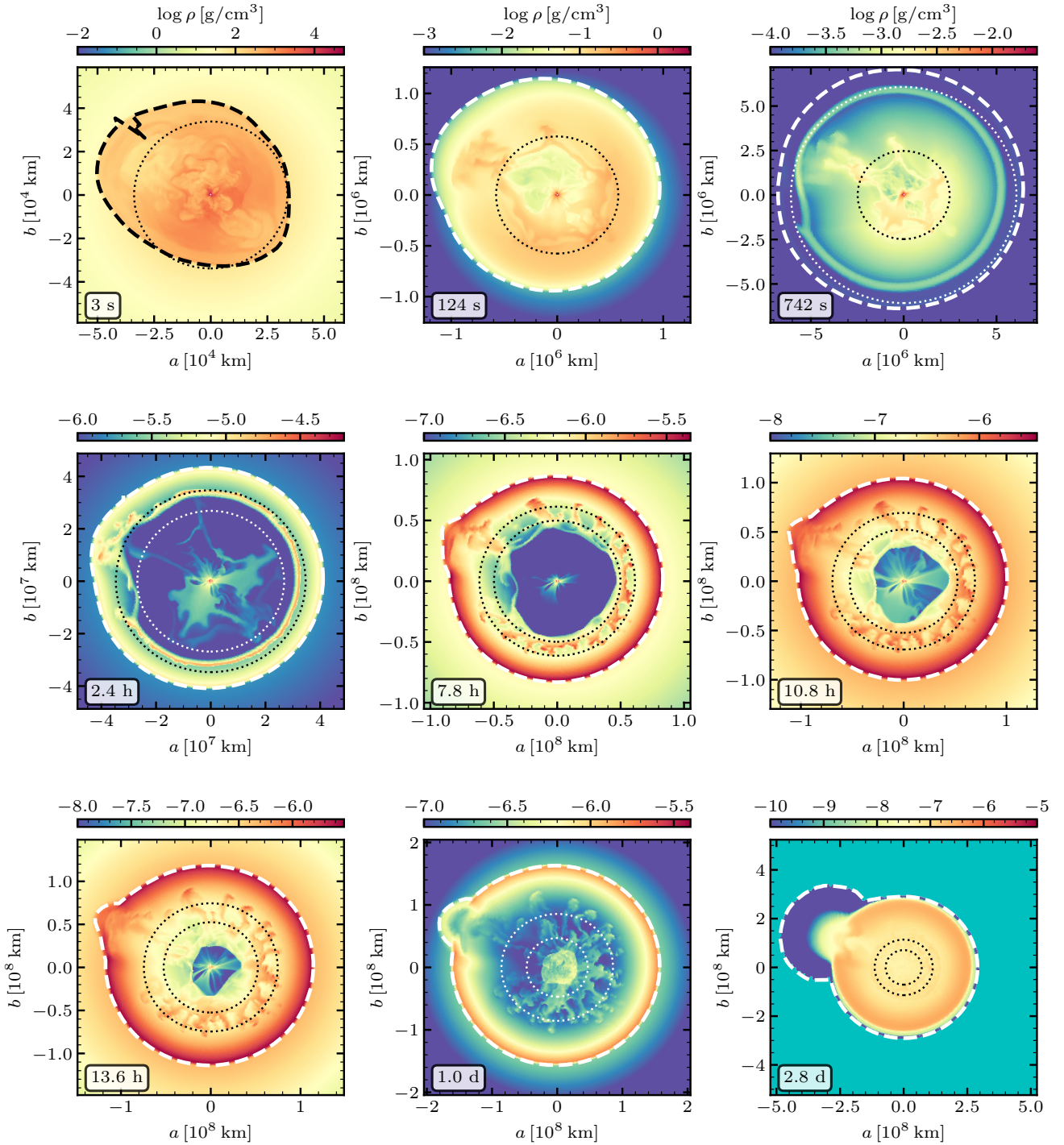
Figure 22. Slices of the density of model s9.0 at the indicated times. The dashed white or black line indicates the shock surface, whereas the dotted white or black lines mark the locations where the enclosed mass equals the mass interior to the CO/He and He/H composition interfaces of the progenitor. The cyan colored region in the bottom right panel represents the surrounding medium of the progenitor. Different from the ECSN-like progenitors, we observe here the growth of large-scale RT plumes caused by the great asymmetries at the onset of the explosion. The seed for the biggest later structure is set already at around 3 s after bounce when the shock passes the CO/He interface. (The kink of the black dashed line for the shock surface at this time is a numerical artifact due to the shock-detection algorithm.) We first observe the growth of the RT instability in the direction perturbed by the largest and fastest initial convective plume (see, e.g., $t_{pb} = 124$ s, at the 10 o'clock position), and there is less deceleration of this dense clump of ^{56}Ni+Tr when it penetrates the CO/He interface. It therefore begins to move far ahead of the slower ^{56}Ni+Tr. Shortly afterwards the plume arrives at the unstable He/H interface, inducing a large-scale perturbation there. While the slower clumps of ^{56}Ni+Tr are further decelerated by the reverse shock that forms at the He/H interface, the biggest clump begins to push the shock, thereby transporting a significant amount of neutrino-heated ejecta to velocities larger than the average shock velocity (see also Figure 13).
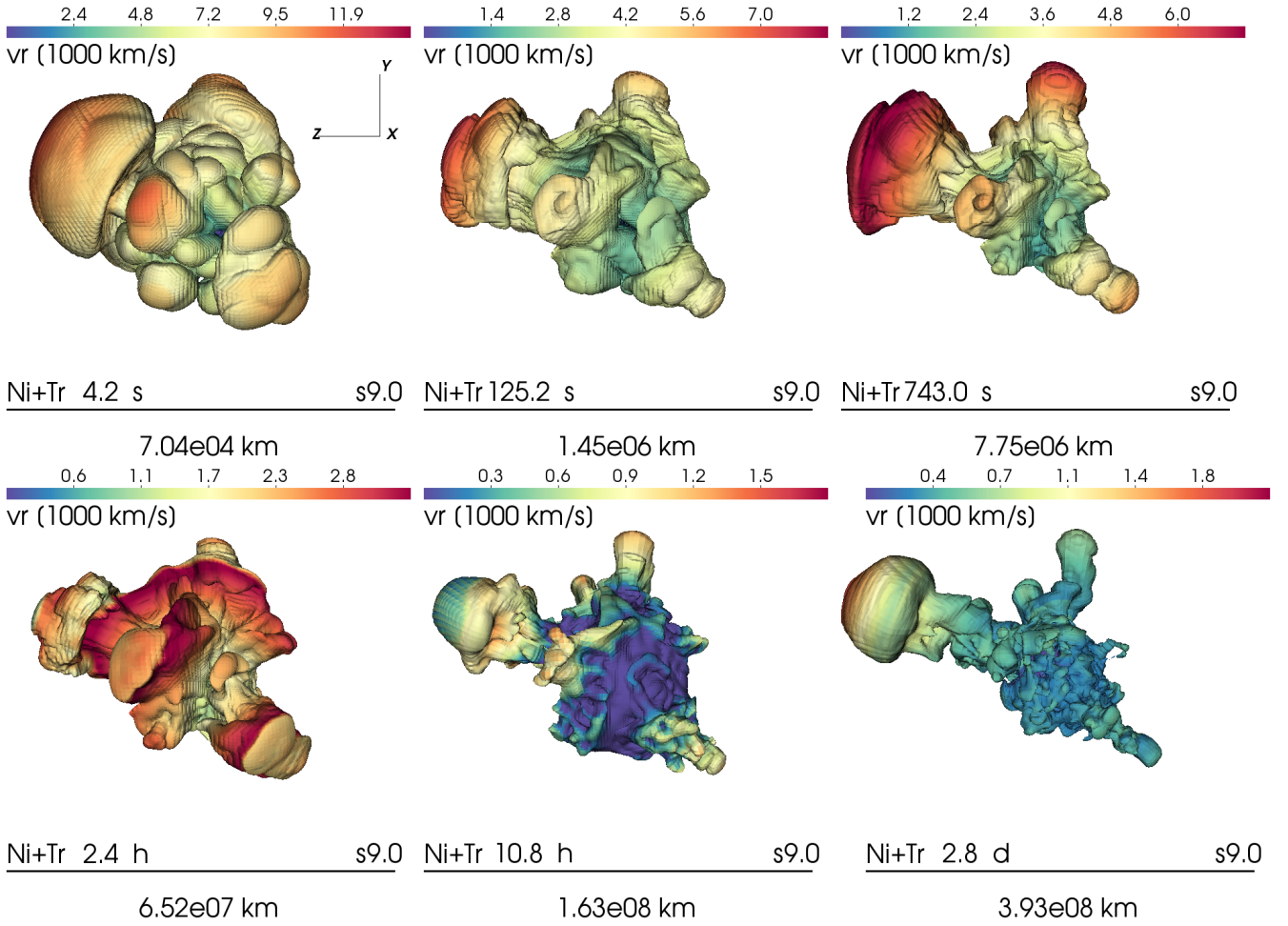
Figure 23. 3D renderings of the $X_{56\,\text{Ni+Tr}} = 0.03$ iso-surface of model s9.0 at the indicated times. The color-coding represents the radial velocity of the material, and the tripod in the left panel defines the orientation of the global coordinate system. During the first roughly 800 s, the largest initial asymmetries grow to extended metal-rich plumes. Slower iron-group matter in the interior is decelerated by the collision with the dense shell formed around the CO/He interface. In the following, these fastest clumps encounter the dense shell behind the He/H and induce large-amplitude perturbations in the RT unstable layer. Consequently, large metal rich RT fingers begin to grow from the interface. At $t_{pb} = 2.8$ d we find one very big and two smaller metal-rich plumes, of which the largest one penetrates the surface of the star even ahead of the average shock radius (see also Figures 21 and 22).

and deceleration phases of the SN shock passing the composition shell interfaces. As described in Sections 5.2 and 5.3, these reverse shocks propagate backward into the central volume.

In Figure 25 we show, starting from t_{map}, the corresponding time-dependent mass accretion rate through the inner boundary of our computational grid, $|\dot{M}(t)|(R_{\text{ib}})$ (top panel), the associated time-integrated accreted mass, $\int_{t_{\text{map}}}^{t} dt' \, |\dot{M}(t')|(R_{\text{ib}})$ (middle panel), and the evolution of the angular momentum of the NS, $J_{\text{NS}}(t)$, driven by the angular momentum that is carried by fallback material into the central volume and that is assumed to be accreted into the compact remnant (bottom panel) for all of our 3D long-time simulations. For comparison, Table 6 lists the values of the NS masses (baryonic and gravitational), total kick velocities, $v_{\text{NS}}^{\text{tot}}$, total angular momenta, J_{NS}, and spin periods, P_{NS}, as well as the angle between NS spin and kick vectors, θ_{vJ}, at t_{map} and at the end of the 3D simulations, t_{fin}.

During the first fallback episode, i.e., during the first tens of seconds, all three models behave differently because of their different evolution during the neutrino-wind phase. In model e8.8 the

forward shock is very fast and the slower neutrino-driven wind (adopted from a parametric 1D simulation; see Fig. 3) expands freely behind the shock without deceleration and without developing a reverse shock. After the termination of the neutrino-driven wind at ~2.5 s post bounce, fallback sets in, but the mass accretion onto the NS declines steeply, because the ejecta move rapidly outward, evacuating the surroundings of the compact object.

In model z9.6 a similar situation applies, but the faster and more long-lasting neutrino-driven wind (adopted from a self-consistently computed NS cooling model; see Fig. 3) is stronger and evacuates the neighbourhood of the NS even more extremely than in model e8.8. However, a reverse shock forms when the forward shock passes the CO/He interface and decelerates, while at the same time the neutrino-driven wind pushes from behind and compresses the post-shock matter into a dense shell. This reverse shock moves inward within a few seconds and creates the short accretion spike at ~8 s (Figure 25). The accretion peak decays within only a second when a reflected wave sweeps through the medium surrounding the PNS outward again. Model z9.6 displays the lowest mass accretion of all three models. In contrast, model s9.0 has by far the highest
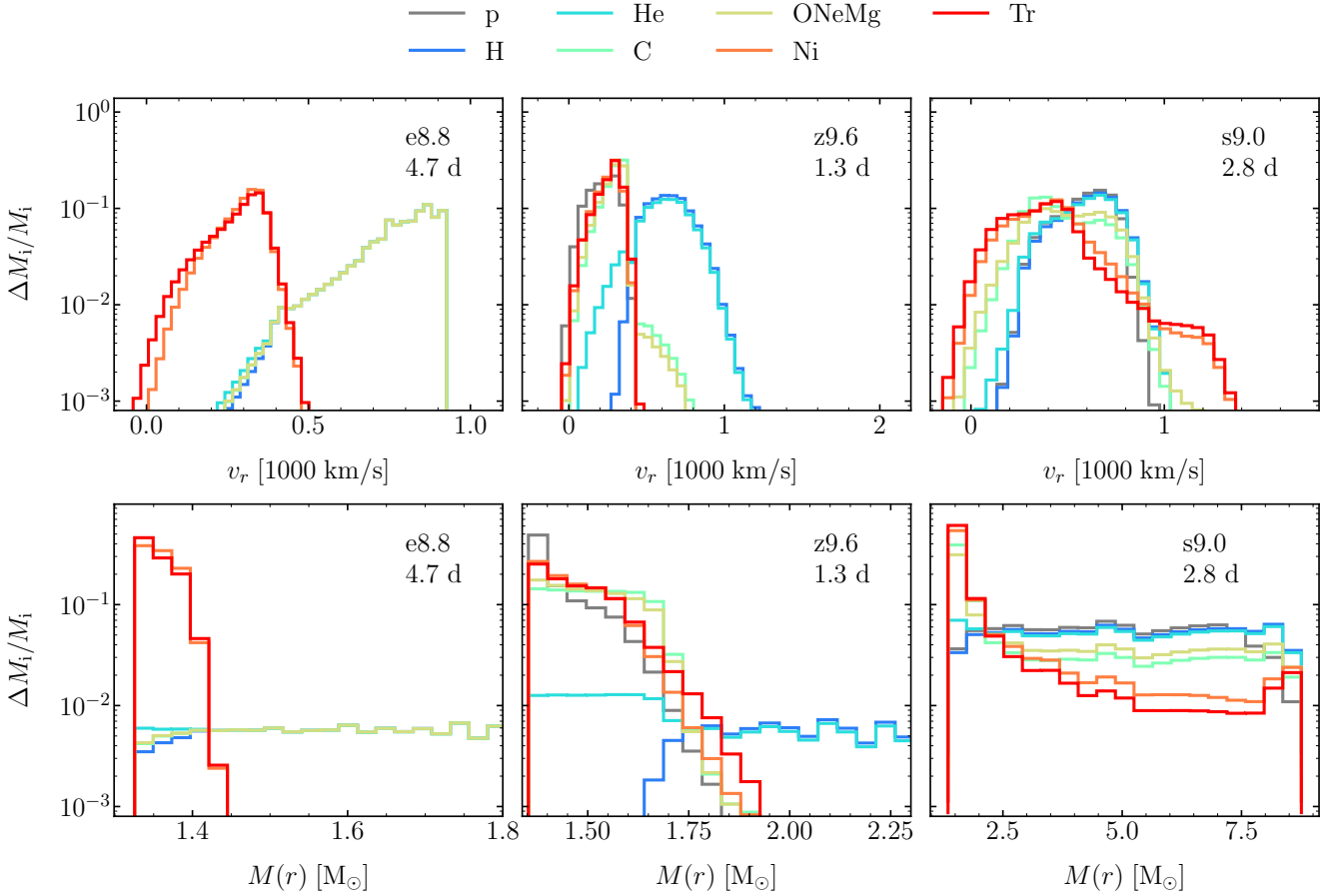
Figure 24. Normalized mass distributions of chemical elements versus radial velocity (top row) and enclosed mass (bottom row) for the ejecta of all of our 3D models at the time of shock breakout. We use 50 bins in velocity space and 30 bins in mass space, starting outside of the compact remnant mass and only showing the distributions up to $1.8\,M_\odot$ and $2.26\,M_\odot$ for models e8.8 and z9.6, respectively, since mixing of the neutrino-heated ejecta beyond these values of the enclosed mass is insignificant. For model s9.0 we consider the whole stellar domain for the visualization. The ECSN-like models (e8.8 and z9.6) mix only a tiny amount of ^{56}Ni into the bottom layers of the H-envelope, whereas efficient mixing in model s9.0 transports a significant amount of neutrino-heated ejecta to large mass coordinates up to the stellar surface.

Table 6. Overview of final NS properties in our 3D models at the time of shock breakout.

Model	t_{map} [s]	$v_{\mathrm{NS}}^{\mathrm{tot,map}}$ [km/s]	$J_{\mathrm{NS}}^{\mathrm{map}}/10^{45}$ [cm^{2}g/s]	θ_{vJ} [°]	M_{map} [M$_\odot$]	M_{g} [M$_\odot$]	$P_{\mathrm{NS}}^{\mathrm{map}}$ [s]	t_{fin} 10^5 [s]	$v_{\mathrm{NS}}^{\mathrm{tot,fin}}$ [km/s]	$J_{\mathrm{NS}}^{\mathrm{fin}}/10^{45}$ [cm^{2}g/s]	$\theta_{vJ}^{\mathrm{fin}}$ [°]	M_{fb} [10^{-3} M$_\odot$]	M_{fin} [M$_\odot$]	$M_{\mathrm{g}}^{\mathrm{fin}}$ [M$_\odot$]	$P_{\mathrm{NS}}^{\mathrm{fin}}$ [s]
e8.8	0.47	0.44	0.70	90.0	1.326	1.210	10.58	4.5	0.46	1.77	114.3	0.316	1.326	1.210	4.16
z9.6	1.44	34.90	2.55	45.4	1.353	1.231	2.96	5.0	31.48	40.2	163.6	0.065	1.353	1.231	0.19
s9.0	3.14	40.87	8.05	31.3	1.351	1.230	0.94	4.1	41.32	253.2	101.7	4.999	1.356	1.234	0.030

Notes: The left part of the table (columns 2–8) lists the properties of the PNS at t_{map} (see also Table 4). The right part of the table (columns 10–16) gives the corresponding final NS properties at the end of our long-time simulations, t_{fin}. $v_{\mathrm{NS}}^{\mathrm{tot,fin}}$ is the final total kick velocity of the NS, $J_{\mathrm{NS}}^{\mathrm{fin}}$ its final angular momentum, $\theta_{vJ}^{\mathrm{fin}}$ the angle between spin and (total) kick vectors, M_{fb} the total fallback mass, M_{fin} the final baryonic mass, $M_{\mathrm{g}}^{\mathrm{fin}}$ the gravitational mass and $P_{\mathrm{NS}}^{\mathrm{fin}}$ the spin period, adopting a NS radius of 12 km. It is assumed that all fallback matter is accreted by the NS.

mass accretion through the inner grid boundary since its neutrino-driven wind is very weak. Therefore the NS is not surrounded by a large low-density wind bubble, but instead accretion downflows and rising plumes of neutrino-heated matter continue to coexist in the vicinity of the NS for many seconds of postbounce evolution. The mass accretion rate during the early fallback phase exhibits a correspondingly high plateau between ∼3 s and ∼10 s.

Models e8.8 and z9.6 reach the asymptotic scaling $\dot{M} \propto t^{-5/3}$

(Chevalier & Klein 1978; Zhang et al. 2008; Dexter & Kasen 2013; Wong et al. 2014) already after about 10 s, and this persists until the late fallback associated with the reverse shocks sets in at about 1000 s in z9.6 and at about 9 h in e8.8. In contrast, model s9.0 displays clear deviations from the −5/3 power-law until roughly 1 h, and only gradually approaches the −5/3 power-law behavior later, because of large-scale asymmetries in the fallback material.
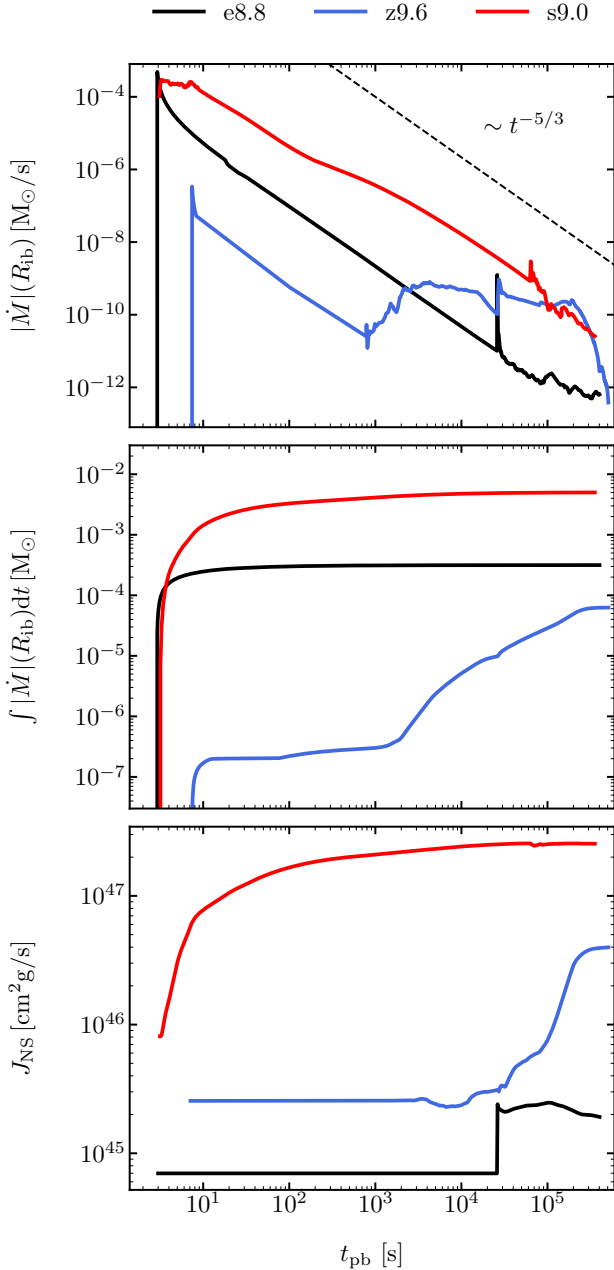
Figure 25. Time evolution of the NS mass-accretion rate (top panel), cumulative accretion of mass (middle panel), and NS angular momentum (bottom panel) associated with fallback during the long-time simulations of all 3D models. After some initial transition phase, which lasts longer in model s9.0 because of the 3D asymmetries of the slow ejecta in the vicinity of the NS, all models adjust to the well-known power-law decline according to $\dot{M} \propto t^{-5/3}$ (black dashed line). This continues until the reverse shock from the outer layers in each model has propagated inward and reaches the inner boundary of the computational grid at radius R_{ib}. In models e8.8 and s9.0 early fallback clearly dominates, whereas in model z9.6 the reverse shock contributes significantly to the total fallback mass. Angular momentum carried through R_{ib} by the infalling matter changes the initial angular momentum of the NS under the assumption that all fallback matter is accreted by the NS. In models e8.8 and z9.6 late fallback associated with the reverse shock causes the main effect on J_{NS}, whereas in model s9.0 the total angular momentum rises continuously and most steeply at early times, when some of the highly asymmetric ejecta fall back onto the NS.

Late accretion due to the reverse shock from the He/H interface is triggered only after ~16 h.

With an integral value around $5 \times 10^{-3}\,\mathrm{M_\odot}$ model s9.0 has the highest total fallback mass (middle panel of Fig. 25), the other two models possess at least 10 times lower values. In all of the three cases the fallback mass is too low to have any significant impact on the NS mass or kick (see Table 6). In principle, the asymmetric fallback of matter can change the net momentum carried by the ejecta with a corresponding increase of the momentum of the NS in the opposite direction. In the considered models this modifies the NS velocity by at most a few kilometers per second (certainly $\lesssim 10\,\mathrm{km\,s^{-1}}$), with the biggest effect in model z9.6 because of the early onset of the reverse-shock induced accretion in this case.

However, the asymmetric fallback of matter also carries angular momentum through the inner grid boundary. Although very little mass is accreted, matter that falls back from large radii can transport appreciable amounts of angular momentum, accounting for the dominant contribution to the total NS angular momentum in all of our simulations. In model s9.0 the angular momentum of the NS increases by more than a factor of 10 to $10^{47}\,\mathrm{g\,cm^2\,s^{-1}}$ within the first 10 s of fallback accretion. It further grows continuously by another factor 2.5 until the 3D simulation was stopped over 4 d later. The final angular momentum of the NS is more than 30 times bigger than at 3 s after bounce. In models e8.8 and z9.6 the NS angular momentum begins to change only when the late reverse shocks reach the center and anisotopic structures begin to be accreted. This amplifies the initial angular momentum of the NS in z9.6 still by a factor of 15 (see bottom panel in Figure 25). In contrast, in model e8.8 the total effect is much more modest because of the low mass associated with the late fallback and the weak asymmetry of the explosion in this case.

Nevertheless, also in model e8.8 the spin period estimated for a NS with 12 km radius decreases from ~11 s at 0.5 s after bounce to a final value of nearly 4 s (Table 6). For z9.6 the spin period shrinks from 3 s at $t_{\mathrm{map}} = 1.44\,\mathrm{s}$ to finally 0.19 s, and for s9.0 the final period is as low as 0.030 s, whereas it had been ~1 s before the fallback.

The NS spins seem to be randomly oriented relative to the NS kick directions, i.e., the angles between NS spin vector and total kick vector, θ_{vJ}, do not show any preference for spin-kick alignment, neither at early times nor days later when the fallback is complete and the simulations are terminated. This is not unexpected and it is in line with previous findings (Wongwathanarat et al. 2013; Müller et al. 2019; Chan et al. 2020; Powell & Müller 2020). To date there is no suggestion based on well accepted physics (i.e., without invoking uncertain ingredients or extreme physical assumptions) for a convincing mechanism that could provide spin-kick alignment. Even if such an alignment were achieved during the first seconds of the explosion, when ejecta and NS are still in contact through hydrodynamical and gravitational forces and the NS is kicked by anisotropic neutrino radiation, it is very hard to imagine how this initial alignment could not be overruled by the stochastic effects of the later fallback and its dominant influence on the NS spin. It might require very rapid progenitor rotation, possibly very strong magnetic fields, to impose a preferred direction for the explosion, correlating the NS recoil acceleration and the spin-up of the NS either by angular momentum inherited during the collapse from the rotating progenitor or later through accretion of stellar angular momentum by fallback (for a suggestion of such a mechanism, see Janka 2017).

Recently, Chan et al. (2020) presented results of an explosion simulation for a non-rotating, zero-metallicity (Pop III) $12\,\mathrm{M_\odot}$ pro-

genitor, including the effects of anisotropic fallback. The overall behavior of this model is similar to our model s9.0, however much more extreme, because the model has a considerably higher fallback mass (nearly $0.2\,M_\odot$), and the corresponding change of the NS kick is several $10\,\mathrm{km\,s^{-1}}$. The accretion of angular momentum associated with the fallback spins the NS up from an early period around $100\,\mathrm{ms}$ to a final period of only a few milliseconds. Interestingly, in this model as well as in the other two cases considered by Chan et al. (2020), in which black holes are formed by fallback, the final angles between spin and kick vectors are close to 90 degrees, very similar to our result for model s9.0. Chan et al. (2020) explain such a perpendicular orientation by the fact that the directions of the accretion streams remain relatively constant in time, thereby corresponding to a single, off-center momentum impulse onto the remnant. Our models e8.8 and s9.0 comply with this pattern, but model z9.6 deviates from this behavior, showing spin-kick anti-alignment.

5.6 Dependence on the explosion energy

In Figure 26 we present the normalized mass distributions of chemical elements as functions of radial velocity for the 2D simulations of model e8.8, using the explosion calibrations as listed in Table 2, at the time of shock breakout.

Comparing the distributions of model $\mathrm{e8.8^{2D}_{10}}$ with the 3D simulation, the extent of mixing in model e8.8 does not seem to be significantly dependent on the chosen dimensionality. This allows us to investigate the influence of the explosion energy on the efficiency of mixing in our 2D simulations of model e8.8.

Inspecting Figure 26, we find that the bulk of ^{56}Ni resides at low velocities of $\sim(0.2-0.4)\times10^3\,\mathrm{km\,s^{-1}}$, increasing with explosion energy roughly as $v_r \sim \sqrt{E_{\mathrm{exp}}}$. For larger explosion energies the downward mixing (to smaller velocities) of lighter elements also seems to be more efficient, but the effect is small and affects only $\lesssim1\%$ of the respective masses. For lower explosion energies the amount of ^{56}Ni+Tr experiencing fallback ($v_r < 0$) grows.

The mixing in velocity space corresponds to a distribution of ^{56}Ni and Tr in mass space to a maximum mass coordinate of about $1.42-1.60\,M_\odot$ (see Figure 27), also increasing with explosion energy, using $\Delta M/M = 1\times10^{-4}$ as a threshold value for plotting the distributions. Note that the $4.49\,M_\odot$ of the hydrogen envelope of the progenitor extended initially from $1.34\,M_\odot$ to $5.83\,M_\odot$, thus mixing only affects the innermost part of the envelope.

As the iron-core progenitors are exploded self-consistently, their explosion energies are fixed within our framework. Drawing direct connections between the amount of mixing and the explosion energy can therefore not be done. Comparing the z9.6 model with the electron-capture model, which both have similar explosion energies, however, suggests that the influence is secondary. More decisive for the amount of nickel mixing are the progenitor structure and initial asymmetries right after shock revival. This view is supported by the strong mixing exhibited by model s9.0, which has a comparable explosion energy as well. The velocity and density perturbations that are present at the onset of the explosion, combined with the strong acceleration and deceleration of the forward shock in the envelope of the progenitor, yield high growth rates of RT instability over a larger range in the mass coordinate and thus dominate over effects caused by different explosion energies in a given progenitor.

6 COMPARISON TO PREVIOUS STUDIES

Some previous works also explored the explosion properties of CC-SNe of low-mass iron and ONeMg-core progenitors. The study by Radice et al. (2017) simulated the onset of the explosion of models e8.8$_n$, z9.6, and s9.0 in 2D with varied microphysics. They found for model e8.8$_n$ an explosion energy of up to $1.8\times10^{50}\,\mathrm{erg}$, which is about a factor of two higher than obtained for the same $8.8\,M_\odot$ star by Kitaura et al. (2006); Janka et al. (2008); Hüdepohl et al. (2010); Fischer et al. (2010), and von Groote (2014). Consistently, their 2D simulations yielded explosion energies for models z9.6 and s9.0 that were $\sim50\%$ higher than in our simulations, namely $1.2\times10^{50}\,\mathrm{erg}$ and $0.7\times10^{50}\,\mathrm{erg}$, respectively; their 3D calculations of model s9.0 yielded even $1.0\times10^{50}\,\mathrm{erg}$ (Burrows et al. 2020).

Müller et al. (2019) focused on the onset of the explosion in helium core progenitors from binary evolution and low-mass single stars also including model z9.6. They found a slightly higher explosion energy of model z9.6 of around $1.3\times10^{50}\,\mathrm{erg}$ at the end of their simulation. Moreover, their explosion energy still seems to grow fairly steeply when they stopped their simulation.

However, Müller et al. (2019) used an approximative neutrino transport treatment ("fast multi-group transport", FMT) with simplified neutrino interactions, and therefore their explosion energies cannot be considered as quantitatively absolutely reliable.[10] The reason why Radice et al. (2017) and Burrows et al. (2020) obtained consistently more energetic explosions than in our VERTEX-PROMETHEUS simulations is unclear to us, in particular because their FORNAX code is claimed to possess neutrino physics that is compatible with that of VERTEX-PROMETHEUS.

We note that, due to the higher explosion energies found in the studies of other groups, the final PNS masses there are smaller than ours in general. A more energetic explosion drives a stronger wind from the PNS, which carries away mass from its surface or reduces further accretion. For example Müller et al. (2019) found the PNS baryonic mass of model z9.6 to be $1.35\,M_\odot$, close to ours, and Burrows et al. (2019) determined the PNS mass of model s9.0 to be $1.342\,M_\odot$, whereas we get $1.351\,M_\odot$ before fallback accretion and $1.356\,M_\odot$ afterwards. The explosion energies and PNS masses of Radice et al. (2017) and Burrows et al. (2020) are not only in conflict with ours but also with other previous studies as for example Kitaura et al. (2006); Janka et al. (2008); Hüdepohl et al. (2010); von Groote (2014) for model e8.8 and Glas et al. (2019a) for model s9.0. These studies consistently attain lower explosion energies with around $10^{50}\,\mathrm{erg}$ for model e8.8 and around $0.5\times10^{50}\,\mathrm{erg}$ for model s9.0, respectively.

Concerning the long-time evolution of the explosion of low-mass CCSNe progenitors, Müller et al. (2018) followed the expansion of the SN shock from its initiation by neutrino heating until shock breakout in an ultra-stripped helium star (he2.8) with a helium-core mass of $1.49\,M_\odot$, which is structurally similar to our

---

[10] In contrast to VERTEX, the FMT treatment neglects fluid-velocity effects and neutrino energy-bin coupling, computes the flux factor from a two-stream approximation (i.e. only for ingoing and outgoing directions, while VERTEX solves the Boltzmann equation for many directions), and uses a subset of additionally simplified neutrino opacities. Therefore, naturally, FMT is not on equal level in accuracy with the VERTEX neutrino transport. Correspondingly, comparisons of FMT and VERTEX results in Müller & Janka (2015) showed "reasonably good overall agreement", but differences in the neutrino luminosities and mean energies can still be considerable (see also Chan & Müller 2020, for a comparison of FMT with Boltzmann transport).
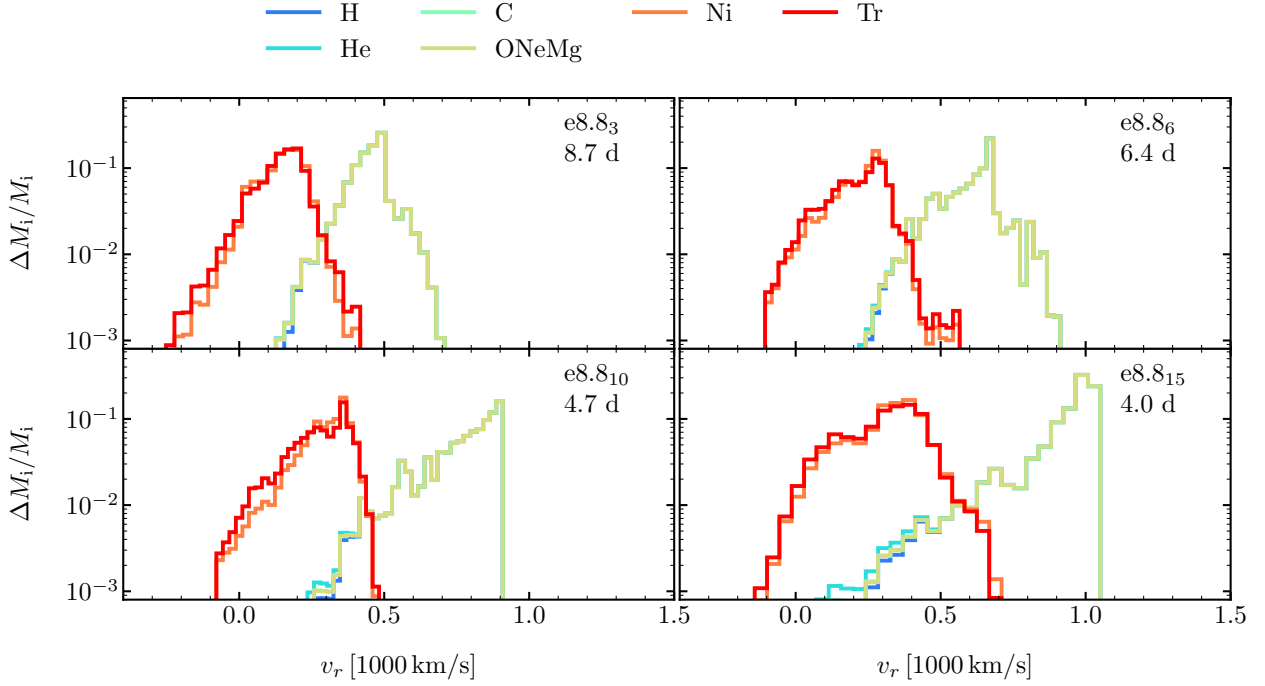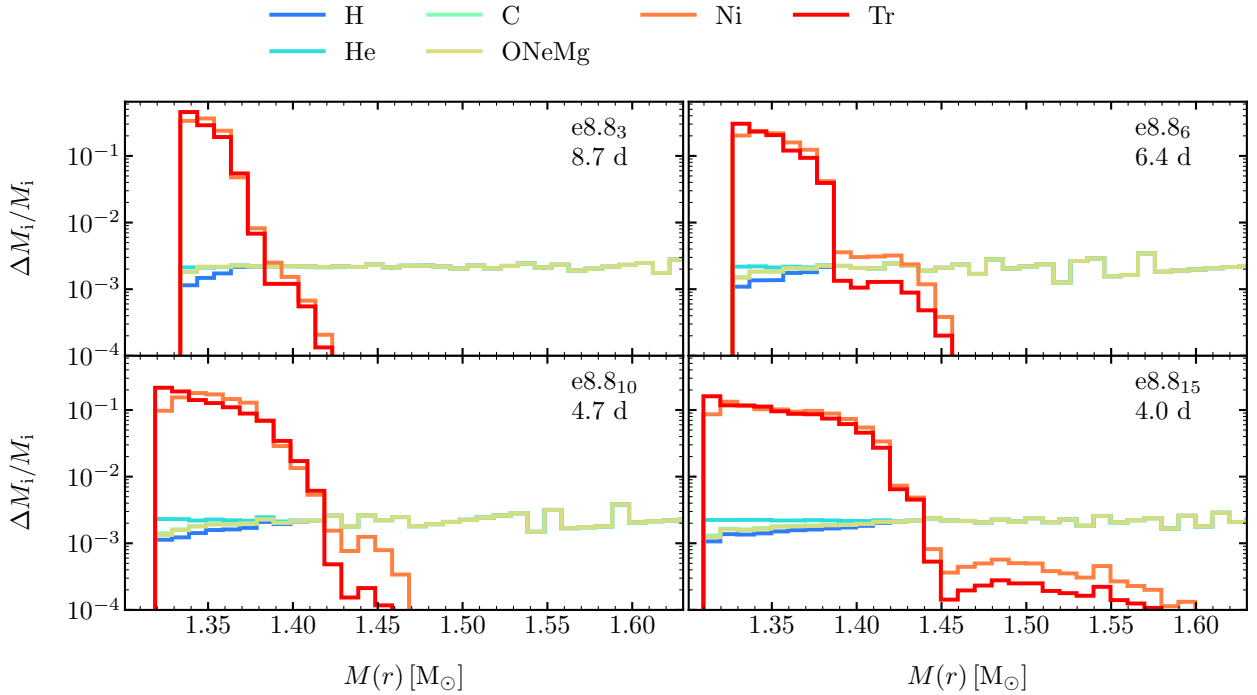
Figure 26. Normalized mass distributions of chemical elements as functions of radial velocity for the long-time 2D simulations of model e8.8 (based on the calibrations listed in Table 2) at the time of shock breakout. Maximum velocities and the velocities of the bulk of ^{56}Ni and Tr scale roughly with $\sqrt{E_{\rm exp}}$, implying slightly enhanced mixing for more energetic models (see also Figure 27). Note that the line corresponding to carbon is hardly visible because it coincides with the line for ONeMg.

Figure 27. Normalized mass distributions of chemical elements as functions of enclosed mass for the 2D simulations of model e8.8 (based on the calibrations listed in Table 2) at the time of shock breakout. Models with higher $E_{\rm exp}$ show slightly more efficient mixing of iron-group material. Note that the line corresponding to carbon is hardly visible because it coincides with the line for ONeMg.

model z9.6. The SN runs (s2.8) of Müller et al. (2018) and Müller et al. (2019) also explode with energies only slightly higher than our simulation of model z9.6, and comparing the maximum mass coordinate of the neutrino-heated ejecta, they exhibit a similar extent of mixing. In their simulation a small fraction of the total iron-group material is mixed to the edge of the helium core of the progenitor star, quite analogously to the case of our model z9.6, where we find a small fraction of the total neutrino-heated ejecta to be mixed out to $M(r) \sim 1.8\,M_\odot$.

Other studies such as those of Kifonidis et al. (2006), Hammer et al. (2010), Wongwathanarat et al. (2015), Chan et al. (2018), Chan et al. (2020), and Ono et al. (2020) and Orlando et al. (2020) also performed simulations of the long-time evolution of CCSNe after shock revival, based on 2D/3D initial data of the beginning explosion. These studies, however, focused on more massive RSG progenitors or BSG progenitors that stand as a proxy for Sanduleak -69 202, the progenitor of SN1987A. Kifonidis et al. (2006) and Hammer et al. (2010) used a $15\,M_\odot$ BSG, while Wongwathanarat et al. (2015) explored various BSG and RSG models from 15–$20\,M_\odot$, and Chan et al. (2018) and Chan et al. (2020) investigated zero-metallicity (Pop III) stars, i.e., a $12\,M_\odot$ progenitor and a black-hole forming $40\,M_\odot$ model. Ono et al. (2020) employed two BSG models with $16.3\,M_\odot$ and $18.3\,M_\odot$ and two RSG stars with ZAMS masses of $18\,M_\odot$ and $19.8\,M_\odot$. While the studies of Kifonidis et al. (2006); Hammer et al. (2010); Wongwathanarat et al. (2015); Chan et al. (2018); Chan et al. (2020) started with initial data from neutrino-driven explosion simulations, Ono et al. (2020) and Orlando et al. (2020) initiated the explosions by injecting energy near the IG/Si interface and parameterized the deformation of the outgoing shock wave in order to mimic the effect of non-radial instabilities at the onset of the explosion and to reproduce the observed morphology of SN1987A. Long-time 3D SN simulations for studying mixing and explosion asymmetries by Ellinger et al. (2012) and Joggerst et al. (2009); Joggerst et al. (2010) started their runs of zero metallicity, low-metallicity, and solar metallicity $15\,M_\odot$ and $25\,M_\odot$ progenitors from spherically symmetric explosions.

These more massive progenitors differ strongly in their ρr^3-profiles when compared to our ECSN-like models. Only model s9.0 exhibits structural features (e.g., a significant variation of the density gradient at the He/H interface) similar to the RSG models of Wongwathanarat et al. (2015). Consequently, all models of the mentioned studies evolve considerably differently from the ECSN-like progenitors presented here. Larger amplification factors at the composition interfaces and a more extended region of instability lead to the growth of large RT plumes, which are absent in models e8.8 and z9.6. Model s9.0, however, behaves in a more similar way, despite the smaller ZAMS mass and considerably lower explosion energy. Although the previous studies are tuned to give around 10^{51} erg for the explosion energy (e.g., to be compatible with observations of SN1978A), we find a similar efficiency of mixing in s9.0, reflected by the distributions of the chemical elements at the end of our simulation. This efficient mixing is facilitated by the strongly asymmetric onset of the explosion and the growth of strong secondary RT instability at the composition interfaces triggered by the initial ejecta asymmetries.

7 SUMMARY AND CONCLUSIONS

In this study we presented results of 1D, 2D, and 3D SN simulations for three non-rotating low-mass progenitors, two of which were RSGs of $9.6\,M_\odot$ (z9.6) and $9\,M_\odot$ (s9.0), respectively, which had

formed $\sim 1.30\,M_\odot$ iron cores at the end of their lives, and the third one was a newly constructed $8.8\,M_\odot$ super-AGB star as ECSN progenitor (e8.8) with a highly degenerate $\sim 1.34\,M_\odot$ ONeMg core[11] and a pre-collapse mass of $5.83\,M_\odot$. Our aim was a comparison of observable features between the models, including the remnant properties, ejecta composition and asymmetries, as well as the radial mixing of chemical species during the SN blast. To this end our simulations covered continuously all evolutionary phases, from the onset of stellar core collapse to core bounce, shock formation, shock stagnation, delayed shock revival by neutrino heating, shock propagation through the stellar mantle and envelope, to shock breakout from the surface of the star, and beyond this moment until fallback of matter to the central compact remnant was complete.

Our investigation by means of neutrino-hydrodynamical simulations was focused on neutrino-driven explosions, because all of the considered progenitors explode self-consistently and fairly quickly after core bounce by the delayed neutrino-driven mechanism. We therefore did not invoke any additional effects such as "jittering jets" (e.g., Soker 2010), which have been suggested as alternative or additional mechanism to revive the stalled SN shock (e.g., Soker 2019), and whose effects have recently been claimed to play a role in the low-energy explosions of low-mass SN progenitors (Gofman & Soker 2020).

7.1 Explosion energies and NS properties

Collapse and explosion of ONeMg-core progenitors have been investigated extensively before by fully self-consistent simulations (Kitaura et al. 2006; Janka et al. 2008; Hüdepohl et al. 2010; Fischer et al. 2010; Müller et al. 2013; von Groote 2014; Radice et al. 2017), yielding quite a spread of blast-wave energies, ranging from several 10^{49} erg to nearly 2×10^{50} erg, depending on details such as the treatment of neutrino transport, general relativity, and the EoS of supranuclear matter in the PNS. Therefore, we simulated the explosions of model e8.8 in 1D, 2D, and 3D with the PROMETHEUS-HOTB code by imposing suitable neutrino luminosities to tune the SN energies to values between 3×10^{49} erg and 1.5×10^{50} erg. Our models reproduce the generic behavior seen previously when the shock wave expands extremely rapidly at running down the steep density gradient that marks the edge of the ONeMg core.

We picked our 3D ECSN model of e8.8 to have an explosion energy of 1.0×10^{50} erg, which is in the ballpark of the previous self-consistent runs by Kitaura et al. (2006) and Hüdepohl et al. (2010), but it is only about half of the energy obtained by Radice et al. (2017). The hydrodynamic kick of the NS in this 3D model was less than $0.5\,\mathrm{km\,s^{-1}}$, and in all of our 2D realizations it stayed below about $1.5\,\mathrm{km\,s^{-1}}$, in agreement with the low kick values obtained by Gessner & Janka (2018).

Models z9.6 and s9.0 were exploded fully self-consistently in 3D by applying the VERTEX-PROMETHEUS code with sophisticated neutrino transport. First results of the initial ~ 0.5 s after bounce for these two simulations were presented by Melson et al. (2015a) and Melson et al. (2020). The explosion energies saturate at values below 10^{50} erg, in the case of z9.6 at 0.85×10^{50} erg, and for s9.0 at about 0.5×10^{50} erg (compatible with Glas et al. 2019a). This is again roughly a factor of two lower than the energies found in 2D and 3D simulations for s9.0 by Radice et al. (2017), Burrows et al. (2019), and Burrows et al. (2020), and in 3D for z9.6 by Müller et al. (2019).

---

[11] But note the remark in Sect. 2.1 that the true mass of the ONeMg core should have been $1.39\,M_\odot$.

However, all of our 3D models explode with energies consistent with the 5×10^{49}–10^{50} erg of the Crab SN (Yang & Chevalier 2015), which has been interpreted as ECSN or as CCSN of a low-mass iron-core progenitor (e.g., Smith 2013; Tominaga et al. 2013). Moreover, all models produce small ejecta masses of radioactive ^{56}Ni, between about $4\times10^{-3}\,M_\odot$ and roughly $6\times10^{-3}\,M_\odot$.

Both iron-core SN models develop a pronounced dipole mode of the lepton-number emission by neutrinos, which goes back to the LESA (Lepton-Emission Self-sustained Asymmetry) phenomenon. The NS kicks induced by the corresponding dipole component of the total neutrino luminosity are around $25\,\mathrm{km\,s^{-1}}$, which is sub-dominant compared to the hydrodynamical NS kick ($\sim30\,\mathrm{km\,s^{-1}}$) in s9.0 but higher than the hydrodynamical kick ($\sim10\,\mathrm{km\,s^{-1}}$) in z9.6. The neutrino-induced kicks might further increase after the end of the evolution that we simulated with detailed neutrino transport (about 0.5 s after bounce), although in model z9.6 a quadrupole emission mode begins to dominate the dipole mode at that time, and the NS acceleration by anisotropic neutrino radiation becomes correspondingly small.

All of our SN simulations of the low-mass progenitors produce NSs with baryonic masses between $\sim1.30\,M_\odot$ and $\sim1.35\,M_\odot$, corresponding to gravitational masses between $\sim1.20\,M_\odot$ and $\sim1.23\,M_\odot$. Right after their formation, during the first seconds of their lives, the new-born NSs spin slowly with periods in the range of seconds, corresponding to angular momenta of the order of some $10^{45}\,\mathrm{g\,cm^2s^{-1}}$. However, this initial spin is dwarfed by later fallback effects. Despite the small fallback masses of at most a few $10^{-3}\,M_\odot$, which neither change the NS masses nor NS kicks to any relevant extent, the fallback transports large amounts of angular momentum to the compact remnant. The angular momentum received from fallback material outruns the previous angular momentum by up to a factor of 30 and can shrink the NS spin period from seconds to tens of milliseconds.

For example, the compact remnant in model s9.0 thus attains a spin period of nearly 1 s before fallback due to asymmetric mass ejection during the early stages of the explosion that transferred an angular momentum of only $8\times10^{45}\,\mathrm{g\,cm^2s^{-1}}$ to the NS. After fallback the spin period of the new-born NS is 30 ms only. This is very close to the 17–19 ms estimated for the birth period of the Crab pulsar in SN 1054 (Manchester & Taylor 1977; Bejger & Haensel 2003; Lyne et al. 2015). The NS in this model received a kick velocity of $41\,\mathrm{km\,s^{-1}}$. However, the velocity is still rising when we stopped monitoring the neutrino- (LESA-) induced component of the NS kick (reaching $\sim25\,\mathrm{km\,s^{-1}}$ in our models), and the final value of the total kick velocity might well be higher. Therefore, we consider this result to be in the ballpark of the spatial velocity of the Crab pulsar, which is inferred to be around $160\,\mathrm{km\,s^{-1}}$ with rather big uncertainties (Hester 2008; Kaplan et al. 2008). A possible spin-kick alignment of the Crab pulsar (see the detailed discussion in Kaplan et al. 2008), however, cannot be explained by our model; s9.0 yields a final angle of $\sim100°$ between NS spin and kick. Since the dominant mechanism for spinning up the NS is fallback, it is very difficult to understand how such a late-time effect, whose angular momentum is connected to stochastic asymmetries of the fallback matter, could correlate with the NS kick direction, which is determined in the first seconds after the onset of the explosion (see also Chan et al. 2020, for similar conclusions for explosions of more massive progenitors). It is also not easy to imagine a scenario where either rotation of the progenitor star (which is not taken into account in our pre-collapse models) or the inclusion of the NS motion in the modelling (which we do not follow because of our use of an inner grid boundary for the long-time runs) could lead

to spin-kick alignment as a deterministic consequence of physical effects. We therefore hypothesize that the spin-kick alignment of the Crab pulsar, if true and a relic of the SN explosion and not just a projection effect, is a purely incidental outcome.

From all of the three progenitors, only s9.0 seems to have favorable properties to explain the explosion energy of SN 1054 as well as the magnitude of the spin and kick of the Crab pulsar. Models e8.8 and z9.6 explode too symmetrically and possess too little fallback to yield the short spin period. Moreover, in such symmetric explosions the NS kick is strongly dominated by a component associated with anisotropic neutrino emission (which our simulations tracked only in models z9.6 and s9.0). Model s9.0 also demonstrates that very low explosion energies ($\sim0.5\times10^{50}$ erg in this case) do not exclude sizable NS kick velocities when the explosion occurs highly asymmetrically; the momentum asymmetry of the ejecta is $\alpha_{\mathrm{ej}}\sim10\%$ after ~3 s in this model.

Therefore we reason that the observed kick and spin of the Crab pulsar may be most naturally explained by considerable asymmetries of the explosion and fallback in a CCSN of a low-mass Fe-core progenitor. It is also important to note that the considered progenitors of z9.6 and s9.0 are just two samples of this class of SN progenitors, and there is a large variety of them, filling the gaps in between, and beyond, including more extreme hAGB-like models beyond z9.6. Therefore our study is just a starting point in exploring this most interesting regime, which is not small in terms of its weight by the stellar initial mass function (e.g., for the z-series it spans the range of ~9.6–$10.3\,M_\odot$).

Nevertheless, alternative possibilities cannot be excluded on grounds of our results, because our conclusions apply for the considered low-mass progenitor properties, which do not include rotation at the onset of core collapse. Rotation of the progenitor core can be relevant for the spin of the NS, in particular in explosions with little fallback or little angular momentum connected to the fallback (for a recent discussion of the many facets of angular momentum transport in massive-star evolution and possible implications for NS rotation, see Ma & Fuller 2019). For example, the degenerate pre-collapse core may spin up considerably during contraction, and the compact ONeMg core near the Chandrasekhar mass limit might rotate rapidly, if the initial angular momentum is (partially) conserved. This latter requirement may be enabled by the fact that the core evolves very much independently from the envelope due to the very steep density gradient around the core-envelope interface of a super-AGB star. Thus, the angular momentum transport from the core to the extended envelope could be small. Rotation could even increase the mass of the degenerate ONeMg core compared to the non-rotating case ("super-Chandra" cores), with a mass excess that depends on the degree of differential rotation (Uenishi et al. 2003; Benvenuto et al. 2015; Hachisu et al. 2012).

Another possibility could be a close binary progenitor scenario, in which, for example, the formation and collapse of an ONeMg core might occur as a result of the merging of two white dwarfs in a certain common-envelope configuration formed during the close binary evolution (Nomoto 1985). In such a case, the disrupted white dwarf material would form a relatively dense envelope around the collapsing ONeMg core and affect the properties of the resulting NS. This scenario as well as the previous one might account for the spin of the Crab pulsar, but both of them are likely to share the problem with our explosion models of e8.8 and z9.6 that the NS kicks stay too low.

If the NS progenitor was a member of a close binary system, as was speculated for the Crab pulsar (Tsygan 1975), the NS properties may have been affected by the binary nature. In this case

the observed NS velocity might originate from the breakup of the binary when SN 1054 exploded (Blaauw 1961) instead of an intrinsic SN kick. However, spin-kick alignment of the Crab pulsar in such a scenario would require extreme fine tuning of the binary evolution (Horvat et al. 2018).

7.2   Ejecta composition, asymmetries, and mixing

Our three 3D models exhibit considerable differences in their ejecta morphology and long-time evolution. The degree of asymmetry and extent of radial mixing show a clear dependence on the steepness of the density profile around the degenerate core. If the density drops steeply, as in the ECSN-like models of e8.8 and z9.6, quick shock revival and fast shock expansion favor buoyant plumes and bubbles from postshock convection to freeze in on relatively small scales when the shock starts to accelerate outwards. Consequently, asymmetries in the ejecta possess small scales, corresponding to higher-order spherical harmonics modes. In contrast, in model s9.0, which has a significantly flatter density decline around the iron core and higher mass-accretion rate during the shock stagnation phase, the $\sim$300 ms delay for the onset of the explosion permits the development of large-scale asymmetries with dominant dipolar and quadrupolar deformation modes.

Despite these differences, both iron-core models resemble each other in the directional Y_e variations imposed on the neutrino-heated material by the neutrino-emission dipole of the LESA: neutron-rich material is predominantly ejected in one hemisphere, whereas an excess of proton-rich matter is expelled on the opposite side. The width of the mass distribution, however, is broader in the case of z9.6, with Y_e reaching down to nearly 0.39 and up to $\sim$0.63, in contrast to $0.46 \lesssim Y_e \lesssim 0.58$ in s9.0.

In both the e8.8 and z9.6 progenitors, the SN shock expands very rapidly at the beginning, but is dramatically decelerated when it travels through the hydrogen plus helium shells with their positive gradients of ρr^3. This triggers the formation of a strong reverse shock propagating inward as well as the creation of conditions for the growth of RT instability, which distributes the neutrino-processed material including freshly nucleosynthesized radioactive species like ^{56}Ni in stretched fingers and plumes within an extended spatial volume. Nevertheless, very little of this material gets mixed into the hydrogen envelope, and the corresponding distribution remains narrow in mass space, stretched out only over the innermost $\sim$0.1 M$_\odot$ of the ejecta in the case of e8.8 and $\sim$0.6 M$_\odot$ in z9.6. In both cases the maximum ^{56}Ni velocities are around 500 km s^{-1}.

In contrast, in model s9.0 the SN shock propagates rather steadily, yet less rapidly (though still with $\sim$10^4 km s^{-1}), during the first 150 s, but it is also strongly decelerated after entering the hydrogen envelope. Because the shock is highly deformed in this explosion and the postshock ejecta are extremely asymmetric from the beginning, these initial ejecta asymmetries trigger the rapid and powerful growth of Richtmyer-Meshkov instability and RT instability at the He/H interface. Big plumes of nickel-rich matter, originating from the biggest bubbles at the time of shock revival, shape the large-scale asymmetry of the SN blast by penetrating deep into the hydrogen envelope. In fact, the most extended of these plumes is pushed by buoyancy forces so strongly that it catches up with the continuously decelerated SN shock and creates a massive deformation of the shock front, thus overtaking the average shock radius. This effect persists until the shock breaks out from the stellar surface, which therefore happens highly asymmetrically. The first, biggest plume pushes the shock through the surface of the progenitor after roughly 2.1 days, whereas the main sphere of the shock reaches the stellar surface considerably later after 2.8 days. Since radioactive nickel is mixed through the entire hydrogen envelope in this model, it expands with velocities up to 1400 km s^{-1} after the breakout from the star (and might be even further accelerated due to radioactive decay heating).

The bubble-driven, asymmetric breakout of the SN shock in our 9 M$_\odot$ model will have ramifications for theoretical studies of this evolution phase and for the interpretation of corresponding observations (e.g., Nakar & Sari 2010; Kozyreva et al. 2020). Since at that time the giant plume contains about 10–20% of the radioactive material produced in the deepest layers of the SN, the one-sided expansion of such a feature will cause a strongly direction-dependent emission of gamma-rays and X-rays, which will occur particularly early in the hemisphere of the bubble breakout (for recent investigations of high-energy radiation emission based on asymmetric 3D explosion models, see Alp et al. 2018, 2019; Orlando et al. 2020; Jerkstrand et al. 2020). The deep mixing of iron-group nuclei and radioactive species from the core through the whole hydrogen shell also plays an important role in shaping the Type-II SN light curve during the luminosity peak (Utrobin et al. 2017). Moreover, the large-scale deformation of the stellar envelope by extended, wide-angle plumes enriched with heavy elements might also offer an explanation why some Type-IIP SNe show an unusually early rise of the polarization *before* the tail phase is entered, and thus *before* the helium core is exposed by the transparency of the hydrogen envelope (Nagao et al. 2019). Last but not least, an outward pushing RT plume with its long-stretched stem might be a mechanism to create the faint protrusion extending out from the northern rim of the visible Crab Nebula, which is often called northern ejecta 'jet' (e.g., Gull & Fesen 1982; Blandford et al. 1983; Davidson & Fesen 1985; Fesen & Staker 1993; Black & Fesen 2015). Such an origin would naturally allow for understanding the fact that the jet's sharp western limb and its blueshifted and redshifted sides seem to be radially aligned with the center of expansion of the remnant (Black & Fesen 2015). The hollow appearance of the jet in [OIII] line emission, its remarkably empty, elliptical shape, and its growing diameter with larger distance from the remnant center, all of which define a funnel-like structure, could be naturally explained in such a picture. The jet walls would be expected to contain oxygen swept up when the RT plume penetrates the oxygen shell of the progenitor, whereas the jet's interior should contain a reduced oxygen fraction but enhanced content of iron-group elements and possibly also silicon.

An alternative possibility to create Crab's northern ejecta funnel might be a jet produced by a fallback disk. The specific angular momentum associated with the 5×10^{-3} M$_\odot$ of fallback matter (about 2.5×10^{16} cm^2 s^{-1} for a total of $\sim 2.5 \times 10^{47}$ g cm^2 s^{-1}) is large enough to keep the matter on Keplerian orbits at a radius of 30–35 km around the NS (Noam Soker, 2020, private communication). If an accretion disk forms, a part of the disk matter might be expelled again in jets. With an escape velocity around 10^{10} cm s^{-1}, even only 10% of the fallback mass would carry a considerable amount of energy (Soker 2020) with sufficient excess energy to punch a funnel into the SN ejecta. It is interesting to note that the disk and jet would be expected at a large angle relative to the NS kick direction, because the angular momentum and kick vectors are nearly perpendicular (see Table 6). This resembles the geometry in the Crab case, where the northern jet has a large angle relative to the NS's projected direction of motion.

A more detailed analysis of the evolving plume structure, based preferably also on higher-resolution 3D simulations, and more detailed studies of the fallback accretion are needed to consolidate

such appealing scenarios. Another interesting extension of our work concerns the nucleosynthetic post-processing of the LESA-affected neutron-rich and proton-rich components of the neutrino-heated ejecta. Since our 2D and 3D results of the mass distributions as functions of Y_e exhibit, overall, fairly close similarities, however, we expect basic confirmation of the trends already seen in a recent study of element formation in the ejecta of 2D simulations for low-mass stars including the e8.8 and z9.6 progenitors (Wanajo et al. 2018). Finally, it would be desirable to repeat our 3D explosion modeling with 3D pre-collapse conditions originating from the latest phases of convective oxygen and silicon shell burning (e.g., Arnett & Meakin 2011; Couch et al. 2015; Müller 2016; Müller et al. 2016; Yoshida et al. 2019; Yadav et al. 2020). The large-scale density and velocity perturbations created by the convective shell burning prior to collapse are more realistic seeds for the growth of postshock instabilities than the artificial, small-amplitude, stochastic cell-by-cell seed perturbations that we imposed on the spherical progenitor models in our present calculations. The larger physical perturbations of 3D initial models might lead to earlier explosions, in particular of the s9.0 progenitor, and might also affect the shock and explosion asymmetry right after shock revival (see Couch & Ott 2013; Müller & Janka 2015; Müller et al. 2017; Kazeroni & Abdikamalov 2020).

REFERENCES

Abbott B. P., LIGO Scientific Collaboration VIRGO Collaboration 2017, Phys. Rev. Lett., 119, 161101
Abbott B. P., LIGO Scientific Collaboration VIRGO Collaboration 2020, ApJL, 892, L3
Alp D., Larsson J., Fransson C., Gabler M., Wongwathanarat A., Janka H.-T., 2018, ApJ, 864, 175
Alp D., et al., 2019, ApJ, 882, 22
Arcones A., Janka H. T., Scheck L., 2007, A&A, 467, 1227
Arnett W. D., Meakin C., 2011, ApJ, 733, 78
Arnett W. D., Bahcall J. N., Kirshner R. P., Woosley S. E., 1989a, ARA&A, 27, 629
Arnett D., Fryxell B., Müller E., 1989b, ApJL, 341, L63
Bejger M., Haensel P., 2003, A&A, 405, 747
Benvenuto O. G., Panei J. A., Nomoto K., Kitamura H., Hachisu I., 2015, ApJL, 809, L6
Bethe H. A., Wilson J. R., 1985, ApJ, 295, 14
Blaauw A., 1961, Bull. Astron. Inst. Netherlands, 15, 265
Black C. S., Fesen R. A., 2015, MNRAS, 447, 2540
Blandford R. D., Kennel C. F., McKee C. F., Ostriker J. P., 1983, Nature, 301, 586
Blondin J. M., Mezzacappa A., 2007, Nature, 445, 58
Blondin J. M., Mezzacappa A., DeMarino C., 2003, ApJ, 584, 971
Bludman S. A., van Riper K. A., 1978, ApJ, 224, 631
Buras R., Rampp M., Janka H.-T., Kifonidis K., 2006, A&A, 447, 1049
Burrows A., 2013, Rev. of Mod. Phys., 85, 245
Burrows A., Hayes J., Fryxell B. A., 1995, ApJ, 450, 830
Burrows A., Radice D., Vartanyan D., 2019, MNRAS, 485, 3153
Burrows A., Radice D., Vartanyan D., Nagakura H., Skinner M. A., Dolence J. C., 2020, MNRAS, 491, 2715
Chan C., Müller B., 2020, arXiv e-prints, p. arXiv:2003.02845
Chan C., Müller B., Heger A., Pakmor R., Springel V., 2018, ApJ, 852, L19
Chan C., Müller B., Heger A., 2020, arXiv e-prints, p. arXiv:2003.04320
Chevalier R. A., 1989, ApJ, 346, 847
Chevalier R. A., Klein R. I., 1978, ApJ, 219, 994
Childs H., et al., 2012, VisIt: An End-User Tool For Visualizing and Analyzing Very Large Data
Colella P., Woodward P. R., 1984, J. Comput. Phys., 54, 174
Colgate S. A., White R. H., 1966, ApJ, 143, 626
Couch S. M., O'Connor E. P., 2014, ApJ, 785, 123
Couch S. M., Ott C. D., 2013, ApJL, 778, L7
Couch S. M., Chatzopoulos E., Arnett W. D., Timmes F. X., 2015, ApJL, 808, L21
Davidson K., Fesen R. A., 1985, ARA&A, 23, 119
Dexter J., Kasen D., 2013, ApJ, 772, 30
Ellinger C. I., Young P. A., Fryer C. L., Rockefeller G., 2012, ApJ, 755, 160
Ertl T., Janka H. T., Woosley S. E., Sukhbold T., Ugliano M., 2016, ApJ, 818, 124
Ertl T., Woosley S. E., Sukhbold T., Janka H. T., 2020, ApJ, 890, 51
Fernández R., 2010, ApJ, 725, 1563
Fesen R. A., Staker B., 1993, MNRAS, 263, 69
Fischer T., Whitehouse S. C., Mezzacappa A., Thielemann F. K., Liebendörfer M., 2010, A&A, 517, A80
Foglizzo T., Galletti P., Scheck L., Janka H. T., 2007, ApJ, 654, 1006
Fryer C. L., 2009, ApJ, 699, 409

Fryxell B., Müller E., Arnett D., 1989, in Hillebrandt W., Müller E., eds, Nuclear Astrophysics. Max Planck Institute for Astrophysics, Garching, p. 100

Fryxell B., Müller E., Arnett D., 1991, ApJ, 367, 619

Gessner A., Janka H.-T., 2018, ApJ, 865, 61

Glas R., Just O., Janka H.-T., Obergaulinger M., 2019a, ApJ, 873, 45

Glas R., Janka H. T., Melson T., Stockinger G., Just O., 2019b, ApJ, 881, 36

Gofman R. A., Soker N., 2020, MNRAS, 494, 5902

Grefenstette B. W., et al., 2017, ApJ, 834, 19

Gull T. R., Fesen R. A., 1982, ApJL, 260, L75

Hachisu I., Kato M., Saio H., Nomoto K., 2012, ApJ, 744, 69

Hammer N. J., Janka H.-T., Müller E., 2010, ApJ, 714, 1371

Heger A., Woosley S. E., 2010, ApJ, 724, 341

Herant M., Benz W., Hix W. R., Fryer C. L., Colgate S. A., 1994, ApJ, 435, 339

Hester J. J., 2008, Ann. Rev. Astron. Astrophys., 46, 127

Hillebrandt W., 1982, A&A, 110, L3

Horowitz C. J., 2002, Phys. Rev. D, 65, 043001

Horvat M., Conroy K. E., Pablo H., Hambleton K. M., Kochoska A., Giammarco J., Prša A., 2018, ApJS, 237, 26

Hüdepohl L., Müller B., Janka H. T., Marek A., Raffelt G. G., 2010, Phys. Rev. Lett., 104, 251101

Hunter J. D., 2007, Comp. Sci. Eng., 9, 90

Janka H. T., 1991, PhD thesis, Technische Universität München

Janka H. T., 2001, A&A, 368, 527

Janka H.-T., 2012, Ann. Rev. Nucl. Part. Sci., 62, 407

Janka H.-T., 2017, ApJ, 837, 84

Janka H. T., Müller E., 1995, Phys. Rep., 256, 135

Janka H. T., Müller E., 1996, A&A, 306, 167

Janka H.-T., Müller B., Kitaura F. S., Buras R., 2008, A&A, 485, 199

Janka H.-T., Hanke F., Hüdepohl L., Marek A., Müller B., Obergaulinger M., 2012, Prog. Theor. Exp. Phys., 2012, 01A309

Janka H.-T., Melson T., Summa A., 2016, Ann. Rev. Nucl. Part. Sci., 66, 341

Jerkstrand A., 2017, in Alsabti A. W., Murdin P., eds, Handbook of Supernovae. Springer International Publishing, p. 795, doi:10.1007/978-3-319-21846-5_29

Jerkstrand A., Ertl T., Janka H.-T., Müller E., Sukhbold T., Woosley S. E., 2018, MNRAS, 475, 277

Jerkstrand A., et al., 2020, MNRAS, 494, 2471

Joggerst C. C., Woosley S. E., Heger A., 2009, ApJ, 693, 1780

Joggerst C. C., Almgren A., Woosley S. E., 2010, ApJ, 723, 353

Jones E., Oliphant T., Peterson P., et al., 2001, SciPy: Open source scientific tools for Python, http://www.scipy.org/

Jones S., et al., 2013, ApJ, 772, 150

Jones S., Röpke F. K., Pakmor R., Seitenzahl I. R., Ohlmann S. T., Edelmann P. V. F., 2016, A&A, 593, A72

Jones S., Côté B., Röpke F. K., Wanajo S., 2019, ApJ, 882, 170

Kageyama A., Sato T., 2004, Geochem. Geophys. Geosyst., 5, Q09005

Kaplan D. L., Chatterjee S., Gaensler B. M., Anderson J., 2008, ApJ, 677, 1201

Kazeroni R., Abdikamalov E., 2020, MNRAS, 494, 5360

Kifonidis K., Plewa T., Janka H.-T., Müller E., 2003, A&A, 408, 621

Kifonidis K., Plewa T., Scheck L., Janka H.-T., Müller E., 2006, A&A, 453, 661

Kirsebom O. S., et al., 2019, Phys. Rev. Lett., 123, 262701

Kitaura F. S., Janka H.-T., Hillebrandt W., 2006, A&A, 450, 345

Kozyreva A., Nakar E., Waldman R., Blinnikov S., Baklanov P., 2020, MNRAS, 494, 3927

Lattimer J. M., Prakash M., 2000, Phys. Rep., 333, 121

Lattimer J. M., Schutz B. F., 2005, ApJ, 629, 979

Lattimer J. M., Swesty D. F., 1991, Nucl. Phys. A., 535, 331

Lentz E. J., et al., 2015, ApJL, 807, L31

Leung S.-C., Nomoto K., Suzuki T., 2020, ApJ, 889, 34

Liebendörfer M., 2005, ApJ, 633, 1042

Lyne A. G., Jordan C. A., Graham-Smith F., Espinoza C. M., Stappers B. W., Weltevrede P., 2015, MNRAS, 446, 857

Ma L., Fuller J., 2019, MNRAS, 488, 4338

Manchester R. N., Taylor J. H., 1977, Pulsars. W. H. Freeman

Marek A., Dimmelmeier H., Janka H.-T., Müller E., Buras R., 2006, A&A, 445, 273

Marek A., Janka H. T., Müller E., 2009, A&A, 496, 475

Melson T. F., 2016, Dissertation, Technische Universität München, München

Melson T., Janka H.-T., Marek A., 2015a, ApJ, 801, L24

Melson T., Janka H.-T., Bollig R., Hanke F., Marek A., Müller B., 2015b, ApJ, 808, L42

Melson T., Kresse D., Janka H.-T., 2020, ApJ, 891, 27

Mirizzi A., Tamborra I., Janka H. T., Saviano N., Scholberg K., Bollig R., Hüdepohl L., Chakraborty S., 2016, Nuovo Cimento Rivista Serie, 39, 1

Miyaji S., Nomoto K., Yokoi K., Sugimoto D., 1980, PASJ, 32, 303

Müller B., 2016, Publ. Astron. Soc. Australia, 33, e048

Müller B., Janka H.-T., 2014, ApJ, 788, 82

Müller B., Janka H. T., 2015, MNRAS, 448, 2141

Müller E., Steinmetz M., 1995, Comp. Phys. Commun., 89, 45

Müller E., Fryxell B., Arnett D., 1991a, in ESO Conf. Works. Proc.. p. 99

Müller E., Fryxell B., Arnett D., 1991b, A&A, 251, 505

Müller B., Janka H.-T., Marek A., 2013, ApJ, 766, 43

Müller B., Viallet M., Heger A., Janka H.-T., 2016, ApJ, 833, 124

Müller B., Melson T., Heger A., Janka H.-T., 2017, MNRAS, 472, 491

Müller B., Gay D. W., Heger A., Tauris T. M., Sim S. A., 2018, MNRAS, 479, 3675

Müller B., et al., 2019, MNRAS, 484, 3307

Nadyozhin D. K., 1994, ApJS, 92, 527

Nagao T., et al., 2019, MNRAS, 489, L69

Nakar E., Sari R., 2010, ApJ, 725, 904

Nomoto K., 1984, ApJ, 277, 791

Nomoto K., 1985, in Kafatos M. C., Henry R. B. C., eds, The Crab Nebula and Related Supernova Remnants. Cambridge University Press, Cambridge, pp 97–113

Nomoto K., 1987, ApJ, 322, 206

Nomoto K., Sparks W. M., Fesen R. A., Gull T. R., Miyaji S., Sugimoto D., 1982, Nature, 299, 803

Nomoto K., Shigeyama T., Hashimoto M.-A., 1987, in ESO Conf. Works. Proc.. p. 325

Nomoto K., Shigeyama T., Kumaga S., Hashimoto M.-A., 1988, Proc. Astron. Soc. Aust., 7, 490

Nomoto K., Filippenko A. V., Shigeyama T., 1990, A&A, 240, L1

O'Connor E. P., Couch S. M., 2018a, ApJ, 854, 63

O'Connor E. P., Couch S. M., 2018b, ApJ, 865, 81

O'Connor E., Ott C. D., 2011, ApJ, 730, 70

Ohnishi N., Kotake K., Yamada S., 2006, ApJ, 641, 1018

Ono M., Nagataki S., Ferrand G., Takahashi K., Umeda H., Yoshida T., Orlando S., Miceli M., 2020, ApJ, 888, 111

Orlando S., et al., 2020, A&A, 636, A22

Ott C. D., Roberts L. F., da Silva Schneider A., Fedrow J. M., Haas R., Schnetter E., 2018, ApJL, 855, L3

Pérez F., Granger B. E., 2007, Comp. Sci. Eng., 9, 21

Plewa T., Müller E., 1999, A&A, 342, 179

Pllumbi E., Tamborra I., Wanajo S., Janka H.-T., Hüdepohl L., 2015, ApJ, 808, 188

Powell J., Müller B., 2020, MNRAS, 494, 4665

Qian Y. Z., Woosley S. E., 1996, ApJ, 471, 331

Radice D., Burrows A., Vartanyan D., Skinner M. A., Dolence J. C., 2017, ApJ, 850, 43

Rampp M., Janka H.-T., 2002, A&A, 396, 361

Rayleigh 1882, Proc. London Math. Soc., s1-14, 170

Roberts L. F., Ott C. D., Haas R., O'Connor E. P., Diener P., Schnetter E., 2016, ApJ, 831, 98

Salpeter E. E., 1955, ApJ, 121, 161

Scheck L., Kifonidis K., Janka H.-T., Müller E., 2006, A&A, 457, 963

Sedov L. I., Friedman M., Holt M., Cole J. D., 1961, J. Appl. Mech., 28, 159

Skinner M. A., Dolence J. C., Burrows A., Radice D., Vartanyan D., 2019, ApJS, 241, 7

Smith N., 2013, MNRAS, 434, 102

Soker N., 2010, MNRAS, 401, 2793

Soker N., 2019, arXiv e-prints, p. arXiv:1907.13312

Soker N., 2020, arXiv e-prints, p. arXiv:2005.07645

Stevenson D. S., 2014, Extreme Explosions: Supernovae, Hypernovae, Magnetars and Other Unusual Cosmic Blasts. Springer, New York, NY, doi:https://doi.org/10.1007/978-1-4614-8136-2

Sukhbold T., Ertl T., Woosley S. E., Brown J. M., Janka H.-T., 2016, ApJ, 821, 38

Summa A., Hanke F., Janka H.-T., Melson T., Marek A., Müller B., 2016, ApJ, 825, 6

Suzuki T., Zha S., Leung S.-C., Nomoto K., 2019, ApJ, 881, 64

Swartz D. A., Sutherland P. G., Harkness R. P., 1995, ApJ, 446, 766

Takiwaki T., Kotake K., Suwa Y., 2012, ApJ, 749, 98

Takiwaki T., Kotake K., Suwa Y., 2014, ApJ, 786, 83

Tamborra I., Raffelt G., Hanke F., Janka H.-T., Müller B., 2014a, Phys. Rev. D, 90, 045032

Tamborra I., Hanke F., Janka H.-T., Müller B., Raffelt G. G., Marek A., 2014b, ApJ, 792, 96

Timmes F. X., Arnett D., 1999, ApJS, 125, 277

Tominaga N., Blinnikov S. I., Nomoto K., 2013, ApJL, 771, L12

Tsygan A. I., 1975, Soviet Ast., 18, 798

Tubbs D. L., 1979, ApJ, 231, 846

Uenishi T., Nomoto K., Hachisu I., 2003, ApJ, 595, 1094

Ugliano M., Janka H.-T., Marek A., Arcones A., 2012, ApJ, 757, 69

Utrobin V. P., Wongwathanarat A., Janka H. T., Müller E., 2015, A&A, 581, A40

Utrobin V. P., Wongwathanarat A., Janka H. T., Müller E., 2017, ApJ, 846, 37

Vartanyan D., Burrows A., Radice D., Skinner M. A., Dolence J., 2018, MNRAS, 477, 3091

Vartanyan D., Burrows A., Radice D., Skinner M. A., Dolence J., 2019, MNRAS, 482, 351

Wanajo S., Janka H.-T., Müller B., 2011, ApJL, 726, L15

Wanajo S., Müller B., Janka H.-T., Heger A., 2018, ApJ, 852, 40

Wong T.-W., Fryer C. L., Ellinger C. I., Rockefeller G., Kalogera V., 2014, arXiv e-prints, p. arXiv:1401.3032

Wongwathanarat A., Hammer N. J., Müller E., 2010a, A&A, 514, A48

Wongwathanarat A., Janka H.-T., Müller E., 2010b, ApJL, 725, L106

Wongwathanarat A., Janka H. T., Müller E., 2013, A&A, 552, A126

Wongwathanarat A., Müller E., Janka H.-T., 2015, A&A, 577, A48

Wongwathanarat A., Janka H.-T., Müller E., Pllumbi E., Wanajo S., 2017, ApJ, 842, 13

Woosley S. E., 1989, NY Acad. Sci. Ann., 571, 397

Woosley S. E., Heger A., 2015, ApJ, 810, 34

Yadav N., Müller B., Janka H. T., Melson T., Heger A., 2020, ApJ, 890, 94

Yang H., Chevalier R. A., 2015, ApJ, 806, 153

Yoshida T., Takiwaki T., Kotake K., Takahashi K., Nakamura K., Umeda H., 2019, ApJ, 881, 16

Zha S., Leung S.-C., Suzuki T., Nomoto K., 2019, ApJ, 886, 22

Zhang W., Woosley S. E., Heger A., 2008, ApJ, 679, 639

von Groote J. C., 2014, Dissertation, Technische Universität München, München

APPENDIX A: PNS COOLING MODEL AND INNER BOUNDARY CONDITION IN PROMETHEUS-HOTB

As stated in Section 3.4, we use the modeling approach of Ugliano et al. (2012), Sukhbold et al. (2016), and Ertl et al. (2020) in simulations with PROMETHEUS-HOTB. The central $1.1\,M_\odot$ of the PNS are excised from the computational domain and replaced by an inner grid boundary at R_{ib}. The shrinking of the cooling and deleptonizing PNS is mimicked by the contraction of the inner grid boundary, whose time dependence (see also Arcones et al. 2007) is given by

$$R_{ib}(t) = R_{ib,f} + (R_{ib,i} - R_{ib,f})\exp\left(-\frac{t}{t_0}\right), \qquad (A1)$$

where $R_{ib,f}$ is the final radius, $R_{ib,i}$ the initial radius and t_0 the contraction timescale. $R_{ib,f}$ and t_0 are two representatives of our set of free parameters and are chosen to mimic the behavior of the PNS contraction found in more sophisticated simulations of PNS cooling (see Scheck et al. 2006; Sukhbold et al. 2016, for comparisons with such results).

As detailed in Ugliano et al. (2012), the PNS core of mass $M_c = 1.1\,M_\odot$ is described by an analytic one-zone model under the constraints of energy conservation and the virial theorem including the effects associated with the growing pressure of the accretion layer. The accumulation of mass around the PNS core is followed by the hydrodynamic simulations. The one-zone model provides the time-dependent total neutrino luminosity that leaves the excised core and is imposed as boundary condition (split up into contributions of each of the neutrino species) at the bottom of the computational domain at R_{ib}. It is given by

$$L_{\nu,\text{tot}} = -\frac{2}{5}\frac{3\Gamma - 4}{3(\Gamma - 1)}\frac{GM_c^2 \dot{R}_c}{R_c^2}$$
$$-\frac{3\Gamma - 4}{3(\Gamma - 1)}\frac{a\,GM_c m_{\text{acc}}\dot{R}_c}{R_c^2} - \frac{a\,GM_c\dot{m}_{\text{acc}}}{3(\Gamma - 1)R_c}. \qquad (A2)$$

Here, $\Gamma = 3$ is the adiabatic index of the PNS core (assumed to be homogeneous), G is the gravitational constant, M_c is the core mass, a is a parameter which characterizes the accretion luminosity, and $m_{\text{acc}}(t)$ is the mass contained between the radius of the inner grid boundary, $R_{ib}(t)$, and the radius r_0 at which the density falls below $\rho_0 = 10^{10}\,\text{g cm}^{-3}$. We define $\dot{m}_{\text{acc}}(t) = -4\pi r_0^2 v_0 \rho_0$, where v_0 is the fluid velocity at the position r_0. In multi-dimensional simulations, $\dot{m}_{\text{acc}}$ is determined from angle-averaged values. The time dependence of the core radius R_c in Equation (A2) is prescribed by

$$R_c(t) = R_{c,f} + (R_{c,i} - R_{c,f})\left(1 + \frac{t}{t_L}\right)^p, \qquad (A3)$$

where $p < 0$ is another parameter. We always set the characteristic time scale $t_L = 1\,\text{s}$ and use initially $R_{c,i} = R_{ib,i}$. Note that in general the PNS core radius and the radius of the inner grid boundary can differ during parts of the evolution. The quintuple of p, $R_{ib,f}$, a, $R_{c,f}$, and t_0 constitutes our set of five parameters to approximate the physics of the time evolution of the PNS and to enable SN explosions with chosen energy. The calibration of these parameters was done using the method described in Ertl et al. (2016).

APPENDIX B: CORRECTION TO NEUTRINO-NUCLEON SCATTERING IN PROMETHEUS-HOTB

Because of numerical issues in the neutrino transport module of the previous version of PROMETHEUS-HOTB, long-time simulations

($t_{pb} > 3$ s) including our neutrino transport approximation showed spurious oscillations in the energy source terms Q_ν. In particular, cases where no or only a very late explosion was observed were affected. These undesired effects were caused by an improper treatment of the energy source terms connected to our non-conservative description of neutrino-nucleon scattering. Scheck et al. (2006) coined the net energy exchange rate through neutrino-nucleon scattering, following Tubbs (1979) and Janka (1991), in a closed form:

$$Q_{\nu N} = \frac{1}{4} \frac{\sigma_0 c}{(m_e c^2)^2} C_N \mathcal{E}_N \frac{n_N}{m_N c^2} \{\langle \epsilon^4 \rangle - 6T\langle \epsilon^3 \rangle\}$$
$$\times \frac{L_{e,\nu}}{4\pi r^2 f_\nu c\langle \epsilon \rangle}, \qquad (B1)$$

which is their equation (D.68). Here, the $\langle \epsilon^n \rangle$ (n being a natural number) are spectral averages of powers of the neutrino energy, and T is the gas temperature in MeV. When the temperature exceeds $\langle \epsilon^4 \rangle / 6\langle \epsilon^3 \rangle$, the net rate $Q_{\nu N}$ is negative and neutrinos *receive* energy from the stellar medium through scattering reactions with nucleons. Since the scattering term was implemented in this closed form and could change its sign, it appeared either as an opacity producing contribution to the neutrino-energy absorption rate Q^- (when $Q_{\nu N}$ was positive) or as an energy source rate for neutrinos, Q^+ (when $Q_{\nu N}$ was negative), in the analytic integral of the transport equation employed by Scheck et al. (2006). Because of the associated big changes and alternating signs, the tight coupling of fluxes and source terms caused large-amplitude oscillations in the transport solution for the neutrino fluxes, induced by large variations of the heating and cooling source terms Q^+ and Q^-. This led to unphysical heating of the matter, creating additional luminosity and preventing further cooling of the PNS.

A simple solution to this problem is to split Equation (B1) into two separate source-/sink terms, a neutrino-energy emission rate represented by the temperature-dependent term,

$$Q_{\nu N}^{em} = \frac{3}{2} \frac{\sigma_0 c}{(m_e c^2)^2} C_N \mathcal{E}_N \frac{n_N}{m_N c^2} T\langle \epsilon^3 \rangle \frac{L_{e,\nu}}{4\pi r^2 f_\nu c\langle \epsilon \rangle}, \qquad (B2)$$

and a neutrino-energy absorption rate,

$$Q_{\nu N}^{abs} = \frac{1}{4} \frac{\sigma_0 c}{(m_e c^2)^2} C_N \mathcal{E}_N \frac{n_N}{m_N c^2} \langle \epsilon^4 \rangle \frac{L_{e,\nu}}{4\pi r^2 f_\nu c\langle \epsilon \rangle}. \qquad (B3)$$

The latter rate corresponds to an exponential attenuation factor of the luminosity connected with the neutrino absorption opacity. This factor also accounts for the re-absorption of neutrinos that are locally produced in each computational cell, and thus it can damp source-rate variations very efficiently.

APPENDIX C: MULTIPOLE DECOMPOSITION OF THE NEUTRINO LEPTON-NUMBER FLUX

For our discussion, we decompose the electron-neutrino lepton-number flux density $F_{\nu_e}^n - F_{\bar{\nu}_e}^n$ into spherical harmonics. $F_{\nu_e}^n$ and $F_{\bar{\nu}_e}^n$ denote the individual radial number flux densities of ν_e and $\bar{\nu}_e$, respectively. The real spherical harmonics are defined as

$$Y_\ell^m(\theta, \phi) = \begin{cases} \sqrt{2} N_\ell^m P_\ell^m(\cos\theta)\cos(m\phi) & m > 0, \\ N_\ell^0 P_\ell^0(\cos\theta) & m = 0, \\ \sqrt{2} N_\ell^{|m|} P_\ell^{|m|}(\cos\theta)\sin(|m|\phi) & m < 0, \end{cases} \qquad (C1)$$

with normalization factors

$$N_\ell^m = \sqrt{\frac{2\ell+1}{4\pi} \frac{(\ell-m)!}{(\ell+m)!}} \qquad (C2)$$

and associated Legendre polynomials $P_\ell^m(\cos\theta)$. The coefficients for the multipole analysis are

$$c_\ell^m = \sqrt{\frac{4\pi}{2\ell+1}} \int d\Omega\, r^2 \left[F_{\nu_e}^n(\theta,\phi) - F_{\bar{\nu}_e}^n(\theta,\phi)\right] Y_\ell^m(\theta,\phi). \qquad (C3)$$

In our chosen normalization, the reconstruction reads

$$F_{\nu_e}^n(\theta,\phi) - F_{\bar{\nu}_e}^n(\theta,\phi) = \frac{1}{r^2} \sum_{\ell=0}^{\infty} \sqrt{\frac{2\ell+1}{4\pi}} \sum_{m=-\ell}^{\ell} c_\ell^m Y_\ell^m(\theta,\phi). \qquad (C4)$$

From the coefficients c_ℓ^m, the multipole moments can be calculated according to

$$A_\ell = \sqrt{\sum_{m=-\ell}^{\ell} \left(c_\ell^m\right)^2}. \qquad (C5)$$

Tamborra et al. (2014b) used a different definition for the monopole and dipole components of the lepton-number flux density. Their $A_{Monopole}$ is equal to our A_0, whereas $A_{Dipole} = 3A_1$. This can be easily seen if we consider the lepton-number flux density to consist only of monopol and dipole components. If we also align the coordinate system into the dipole direction, the reconstruction of Equation (C4) reads

$$F_{\nu_e}^n(\theta,\phi) - F_{\bar{\nu}_e}^n(\theta,\phi) = \frac{1}{4\pi r^2} c_0^0 + \frac{3}{4\pi r^2} c_1^0 \cos\theta. \qquad (C6)$$

Note that c_1^{-1} and c_1^1 vanish in this orientation of the coordinate system. Expressed in terms of the multipole moments, the latter expression becomes

$$F_{\nu_e}^n(\theta,\phi) - F_{\bar{\nu}_e}^n(\theta,\phi) = \frac{1}{4\pi r^2} A_0 + \frac{3}{4\pi r^2} A_1 \cos\theta. \qquad (C7)$$

According to Tamborra et al. (2014b), $F_{\nu_e}^n(\theta,\phi) - F_{\bar{\nu}_e}^n(\theta,\phi)$ is proportional to $A_{Monopole} + A_{Dipole}\cos\theta$, if higher-order multipoles do not contribute. We can directly infer $A_{Dipole} = 3A_1$.

APPENDIX D: NEUTRON STAR KICK AND SPIN

Two mechanisms are considered that can lead to a recoil kick of the newly formed NS during the SN blast. First, asphericities developing during the explosion exert hydrodynamic and gravitational forces on the PNS. Both accelerate the PNS in the direction opposite to the strongest direction of the explosion, compatible with global momentum conservation. Since the gravitational effects become dominant during the long-time evolution, this kick mechanism was termed "gravitational tug-boat mechanism" (Wongwathanarat et al. 2013). For a thorough discussion of its physics details, the reader is referred to Scheck et al. (2006), Wongwathanarat et al. (2013), Janka (2017), Gessner & Janka (2018), and Müller et al. (2019). Second, anisotropic emission of neutrinos, specifically the anisotropic neutrino energy flux density, $F_\nu^e(\theta,\phi)$, radiated from the surface of the PNS (θ and ϕ are the direction angles in a polar grid of the star), exerts a force onto the PNS in the direction opposite to the most intense neutrino emission.

Using the momentum conservation equation, the hydrodynamic PNS kick can be simply estimated as

$$\boldsymbol{P}_{NS}^{hyd} = \boldsymbol{v}_{NS}^{hyd} M_b = -\boldsymbol{P}_{gas}, \qquad (D1)$$

where $\boldsymbol{v}_{NS}^{hyd}$ is the hydrodynamic kick velocity, M_b is the baryonic (PNS) mass contained inside the radius R_{NS} where the angle-averaged density drops below 10^{11} g cm^{-3}, and $\boldsymbol{P}_{gas} = \int_{R_{gain}}^{R_{sh}} \rho \boldsymbol{v} dV$

is the total linear momentum of the ejecta between the gain radius, R_{gain}, and the SN shock, R_{sh}. The momentum transfer by escaping neutrinos is given by

$$\dot{\boldsymbol{P}}_\nu(t) = \oint_{r=R_{\text{free}}} \frac{F_\nu^{\text{e}}}{c} \, \boldsymbol{e}_r \, \mathrm{d}S = -\dot{\boldsymbol{P}}_{\text{NS}}^\nu(t), \tag{D2}$$

where F_ν^{e} is the neutrino energy flux summed over all species, c the speed of light, $\boldsymbol{e}_r$ the unit vector in radial direction, and R_{free} the radius of evaluation (typically about 400 km), exterior to which neutrinos stream essentially freely and a tiny fraction of still interacting neutrinos can be ignored. Using $\boldsymbol{P}_\nu(t) = \int_0^t \dot{\boldsymbol{P}}_\nu(t')\mathrm{d}t'$, the total kick velocity of the PNS at any time t can be calculated as

$$\boldsymbol{v}_{\text{NS}}^{\text{tot}}(t) = \frac{\boldsymbol{P}_{\text{NS}}^{\text{hyd}}(t) + \boldsymbol{P}_{\text{NS}}^\nu(t)}{M_{\text{b}}(t)} = -\frac{\boldsymbol{P}_{\text{gas}}(t) + \boldsymbol{P}_\nu(t)}{M_{\text{b}}(t)} . \tag{D3}$$

One can characterize the asymmetry of the ejecta and neutrino emission by means of anisotropy parameters. The hydrodynamic parameter reads

$$\alpha_{\text{ej}} = \frac{|\boldsymbol{P}_{\text{gas}}|}{P_{\text{ej}}}, \tag{D4}$$

where

$$P_{\text{ej}} = \int_{R_{\text{gain}}}^{R_{\text{sh}}} \rho |\boldsymbol{v}| \mathrm{d}V \tag{D5}$$

is the total momentum stored in the ejecta, which becomes equal to the total radial momentum when the ejecta expand essentially radially. For the neutrino anisotropy parameter we use the total energy loss rate in neutrinos, which is given by

$$\dot{E}_\nu(t) = \oint_{r=R_{\text{free}}} F_\nu^{\text{e}} \, \mathrm{d}S . \tag{D6}$$

The time-dependent total flux of neutrino momentum through the sphere at R_{free} is given by $c^{-1}\dot{E}_\nu$ allowing us to define the instantaneous neutrino emission anisotropy parameter as

$$\widetilde{\alpha}_\nu(t) = c \, \frac{|\dot{\boldsymbol{P}}_\nu(t)|}{\dot{E}_\nu(t)} . \tag{D7}$$

In analogy to the linear ejecta momentum at a time t, the momentum radiated by neutrinos until time t is

$$\frac{1}{c} E_\nu(t) = \frac{1}{c} \int_0^t \oint_{r=R_{\text{free}}} F_\nu^{\text{e}}(t') \, \mathrm{d}S \, \mathrm{d}t' \tag{D8}$$

so that the time-integrated neutrino emission asymmetry at time t becomes

$$\alpha_\nu(t) = c \, \frac{|\boldsymbol{P}_\nu(t)|}{E_\nu(t)} . \tag{D9}$$

In addition, we compute the PNS spin by integrating the flux of angular momentum through a sphere of radius r_0 around the origin,

$$\frac{\mathrm{d}\boldsymbol{J}_{\text{NS}}}{\mathrm{d}t} = -r_0^2 \int_{4\pi} \rho v_r \, \boldsymbol{r} \times \boldsymbol{v} \, \mathrm{d}\Omega, \tag{D10}$$

where ρ is the matter density, v_r the radial velocity, and $\boldsymbol{r}$ and $\boldsymbol{v}$ are the position and velocity vectors, respectively. During the early post-bounce evolution with neutrino treatment, $r_0 = 100\,\text{km}$, whereas we use $r_0 = R_{\text{ib}}$ during the long-time simulations.

In order to estimate the spin period of the PNS $P_{\text{NS}} = 2\pi I_{\text{NS}}/|J_{\text{NS}}|$, with I_{NS} being the moment of inertia of the PNS, we use the approximation by Lattimer & Schutz (2005),

$$I_{\text{NS}} = 0.237 M_{\text{g}} R_{\text{NS}}^2 \left[1 + 4.2A + 90A^4 \right], \tag{D11}$$

$$A = M_{\text{g,M}_\odot} R_{\text{NS,km}}^{-1},$$

where $M_{\text{g,M}_\odot}$ is the gravitational mass of the PNS in units of $\text{M}_\odot$, and $R_{\text{NS,km}}$ is the radius of the PNS in units of km. In the above equation, the gravitational mass M_{g} can be estimated from the baryonic mass M_{b} as (Lattimer & Prakash 2000)

$$M_{\text{g}} = M_{\text{b}} - \frac{0.6\beta}{1 - 0.5\beta} M_{\text{g}}, \tag{D12}$$

where $\beta = GM_{\text{g}}/R_{\text{NS}}c^2$.

APPENDIX E: SIMPLIFIED NEUTRINO TREATMENT IN VERTEX-PROMETHEUS

The computational demands of the full-fledged neutrino transport in our VERTEX-PROMETHEUS code are a severe obstacle for continuing simulations well beyond post-bounce times of $\sim 0.5\,\text{s}$. In order to follow explosions to much later times including neutrino effects, we newly implemented a simplified neutrino treatment based on a light-bulb-like scheme for neutrino emission and absorption. Within this framework, we do not solve the neutrino transport equations (i.e., we switch off the transport module VERTEX). Instead, we obtain local neutrino source terms for application in the hydrodynamics module PROMETHEUS from an analytical scaling and transformation of the neutrino source terms that are present in a model at the end of the VERTEX-PROMETHEUS simulation. This moment in time is chosen to be in an evolutionary phase where the model is well on the way to a successful explosion.

Doing so, we aim at capturing the most crucial neutrino effects after the onset of the explosion in a computationally efficient way, while keeping numerical transients at a minimum and thus ensuring a seamless continuation of our simulations after switching off the VERTEX transport. To further increase the time step, we remap the 3D (hydrodynamical) PNS data within 10 km to 1D and slightly reduce the radial resolution in the PNS interior at the beginning of our simulations with simplified neutrino treatment. Moreover, adding more radial zones, the outer grid boundary is shifted from initially 10.000 km to ~ 70.000 km to be able to follow the outward propagation of the shock through the exploding star at later times ($t \gtrsim 1\,\text{s}$ after bounce). In the following, we will elaborate on our new approximate neutrino treatment.

E1 Source terms for energy and lepton number

In our new simplified approach, we apply the following expressions for the net neutrino cooling and heating rates per volume (i.e., the energy source terms):

$$Q_{\text{erg}}^-(\boldsymbol{r}) = Q_{\text{erg}}^0(x) \cdot \left(\frac{\rho(\boldsymbol{r})}{\rho_0(r_0)} \right)^a \left(\frac{T(\boldsymbol{r})}{T_0(r_0)} \right)^6 , \tag{E1}$$

$$Q_{\text{erg}}^+(\boldsymbol{r}) = Q_{\text{erg}}^0(x) \cdot \left(\frac{\rho(\boldsymbol{r})}{\rho_0(r_0)} \right) \left(\frac{R_{\text{gain}}(t_0)}{R_{\text{gain}}(t)} \right)^2 \cdot f_L \, f_E , \tag{E2}$$

where Equation (E1) is employed in regions where $Q_{\text{erg}}^0(x) < 0$ (i.e., PNS cooling), while Equation (E2) is applied where $Q_{\text{erg}}^0(x) > 0$ (i.e., gain-layer heating).[12] The quantities with superscript or subscript "0" are the angle-averaged net heating and cooling rates, Q_{erg}^0,

---

[12] We use Equation (E2) only outside of the PNS, i.e. at radii $r > R_{\text{NS}}$, while we do not allow for heating inside the PNS. Analogously, we do not allow for an increase of the electron fraction by neutrino sources via Equation (E6) in the interior of the PNS.

the angle-averaged density, ρ_0, and the angle-averaged temperature, T_0, at time t_0 when we switch from the transport calculation with VERTEX at $t \leqslant t_0$ to our simplified neutrino treatment at $t > t_0$.[13] To adjust the radial profile of heating and cooling to the contraction of the gain radius, which roughly follows the contraction of the PNS radius, we define the variable $x \equiv r_0/R_{\mathrm{gain}}(t_0) = r(t)/R_{\mathrm{gain}}(t)$, which connects the radial coordinate $r = r(t)$ with $r_0 = r(t_0)$. The factor $[R_{\mathrm{gain}}(t_0)/R_{\mathrm{gain}}(t)]^2$ results from the transformation responsible for the inward shift of the heating profile and ensures that the net heating rate drops like r^{-2} at large radii.

The functional ansatz of Equations (E1) and (E2) fulfills the requirement of a continuous and smooth transition of cooling and heating before and after t_0. The scaling of the heating and cooling rates is motivated by the rough scaling of the ν_e and $\bar{\nu}_e$ absorption rates with the density of a gas of free nucleons, and the scaling of (nondegenerate) electron and positron capture rates on nucleons with the temperature (see, e.g., Janka 2001). The parameter a in Equation (E1) is chosen to be of order unity, depending on the model under consideration, and adjusted to best reproduce the PNS contraction behaviour obtained in a corresponding 1D PNS-cooling simulation with mixing-length convection. For the cases considered in this work, we found $a = 2$ to be a reasonable choice. The factors f_L and f_E in Equation (E2) contain the dependencies of the neutrino heating rate on the radiated luminosities L_{ν_e} and $L_{\bar{\nu}_e}$ (for the energy transferred by ν_e and $\bar{\nu}_e$ absorption per unit of time) and on the mean squared neutrino energy (for the basic energy dependence of the absorption cross section), which we replace by the squared arithmetic average of the mean energies E_{ν_e} and $E_{\bar{\nu}_e}$ of ν_e and $\bar{\nu}_e$ leaving the PNS. In the spirit of our approach explained above, we therefore use the following functional scaling prescriptions:

$$f_L = \frac{L_{\nu_e}(t) + L_{\bar{\nu}_e}(t)}{L_{\nu_e}(t_0) + L_{\bar{\nu}_e}(t_0)}, \qquad \text{(E3)}$$

which holds for core-luminosity-dominated conditions, and

$$f_E = \left(\frac{E_{\nu_e}(t) + E_{\bar{\nu}_e}(t)}{E_{\nu_e}(t_0) + E_{\bar{\nu}_e}(t_0)} \right)^2 \left(\frac{M_{\mathrm{b}}(t)}{M_{\mathrm{b}}(t_0)} \right)^2 . \qquad \text{(E4)}$$

Guided by the findings of Müller & Janka (2014), f_E is assumed to scale with the square of the (baryonic) PNS mass, M_{b}. The approximate time dependence of the ν_e and $\bar{\nu}_e$ luminosities and of the corresponding mean energies is adopted from the PNS-cooling behavior in a 1D explosion simulation of the z9.6 progenitor with VERTEX-PROMETHEUS, which results in a NS of similar mass ($M_{\mathrm{b}} = 1.36\,\mathrm{M}_\odot$, $M_{\mathrm{g}} = 1.26\,\mathrm{M}_\odot$) as obtained in our 3D simulations of the z9.6 and s9.0 models (see Table 4). The mass scaling in Equation (E4) shall account for a possible difference in the evolution of the PNS mass between the 1D and 3D models.

In a manner analogous to Equations (E1) and (E2), we apply the following source terms for the net rates of change (per volume) of the electron number density by neutrino emission and absorption:

$$Q_{\mathrm{lep}}^-(\boldsymbol{r}) = Q_{\mathrm{lep}}^0(x) \cdot \left(\frac{\rho(\boldsymbol{r})}{\rho_0(r_0)} \right)^a \left(\frac{T(\boldsymbol{r})}{T_0(r_0)} \right)^5 \max\left\{ 0, \frac{Y_e(\boldsymbol{r}) - 0.01}{Y_e^0(r_0) - 0.01} \right\}, \qquad \text{(E5)}$$

$$Q_{\mathrm{lep}}^+(\boldsymbol{r}) = Q_{\mathrm{lep}}^0(x) \cdot \left(\frac{\rho(\boldsymbol{r})}{\rho_0(r_0)} \right) \left(\frac{R_{\mathrm{gain}}(t_0)}{R_{\mathrm{gain}}(t)} \right)^2 \cdot f_L\, f_E\, f_{Y_e}\,, \qquad \text{(E6)}$$

where Q_{lep}^0 denotes the angle-averaged net change-rate of the electron density and Y_e^0 the angle-averaged electron fraction at time t_0, when we switch from the calculation with detailed neutrino transport to our simplified neutrino treatment. Deleptonization, as per Equation (E5), applies in regions where $Q_{\mathrm{lep}}^0(x) < 0$ (and $Y_e > 0.01$), whereas for $Q_{\mathrm{lep}}^0(x) > 0$ (and outside of the PNS, cf. footnote 12), the electron number density is changed according to Equation (E6). Since outflowing ejecta in the neutrino-heating layer gain electron number by neutrino absorption while accretion flows deleptonize, which our angle-averaged source terms cannot capture in detail in multi-dimensional conditions, we include a factor f_{Y_e} in Equation (E6). It is defined in terms of the electron fraction (Y_e) as

$$f_{Y_e} = \begin{cases} \max\left\{ 0, \min\left\{ 1, \dfrac{1.1\, Y_e^{\mathrm{eq}} - Y_e(\boldsymbol{r})}{0.1\, Y_e^{\mathrm{eq}}} \right\} \right\}, & \text{if } v_r(\boldsymbol{r}) \geqslant 0, \ \ (\text{E7a}) \\[2ex] (-1) \cdot \Theta\{ Y_e(\boldsymbol{r}) - 0.1 \}, & \text{if } v_r(\boldsymbol{r}) < 0, \ \ (\text{E7b}) \end{cases}$$

with v_r denoting the radial velocity and Θ being the Heaviside step function. The negative sign of Equation (E7b) is supposed to approximately account for the fact that accretion downflows settling onto the PNS lose electron number. Applying Equation (E7a) shall ensure that Y_e in the ejecta is limited by its kinetic equilibrium value of $Y_e^{\mathrm{eq}} = \left[1 + \lambda_{\bar{\nu}_e}/\lambda_{\nu_e} \right]^{-1}$, which is approached when ν_e absorption on neutrons is balanced by $\bar{\nu}_e$ absorption on protons (Qian & Woosley 1996). For the capture rates of ν_e and $\bar{\nu}_e$, λ_{ν_e} and $\lambda_{\bar{\nu}_e}$, respectively, we employ equations (5)–(8) of Pllumbi et al. (2015), which provide the detailed expressions including corrections associated with the neutron-proton mass difference and with weak magnetism (Horowitz 2002). The time-dependent neutrino luminosities and energy moments needed to evaluate the neutrino absorption rates are again taken from a corresponding 1D simulation of PNS cooling.[14]

The gain radius in Equations (E1), (E2), (E5) and (E6), which governs the radial migration of the heating and cooling profile, also needs to be prescribed as a function of time, because its behavior can be tracked only with self-consistent neutrino transport. In our simple heating and cooling treatment we couple the evolution of $R_{\mathrm{gain}}(t)$ to the contraction of the PNS radius $R_{\mathrm{NS}}(t)$ in the following way:

$$R_{\mathrm{gain}}(t) = \left[(C_0 - b)\, \frac{\dot{M}(t)}{\dot{M}(t_0)} + b \right] \cdot R_{\mathrm{NS}}(t), \qquad \text{(E8)}$$

where $C_0 = R_{\mathrm{gain}}(t_0)/R_{\mathrm{NS}}(t_0)$ denotes the ratio of the gain radius to the PNS radius at time t_0, and $b = \min\{1.01, C_0\}$ determines the assumed asymptotic value of $R_{\mathrm{gain}}(t)$ at late times when the mass accretion rate $\dot{M}(t)$ has declined to an insignificant level. This prescription accounts for an inflated PNS mantle and therefore increased gain radius due to ongoing accretion, and it ties in continuously with the evolution of $R_{\mathrm{gain}}(t)$ at times before we switch our neutrino treatment. $\dot{M}$ is evaluated at a fixed radius of 100 km and for downflows ($v_r < 0$) only.

A note of caution is indicated here. We noticed that our cooling prescription according to Equation (E1) can lead to runaway cooling, because a built-in mechanism of self-regulation is missing

---

[13] The radial profiles of $Q_{\mathrm{erg}}^0, \rho_0, T_0$, and Y_e^0 of Equation (E5) are smoothed by time-averaging over the last few ms of the calculations with detailed transport.

[14] Constraining Y_e from the high side in Equation (E7a) is relevant only when our approach is applied in spherically symmetric explosion models. In our 3D simulations we found that Y_e always remains fairly close to 0.5 or the equilibrium value because of the effects of coexisting outflows and downflows. Artificial regulation towards the equilibrium value by the factor f_{Y_e} in Equation (E7a) did therefore not become active in the 3D cases.

in the cooling rate. This can affect regions in the deep interior of the PNS at late evolution times ($t \gtrsim 1$ s after bounce), but it can also cause artifacts already early on in progenitors that are more massive than the ones considered in the present work. In massive stars it can happen that powerful accretion flows reach down to, or even below, the gain radius, in course of which cooling in the narrow layer between the neutrinosphere and the gain radius is overestimated, causing accelerated PNS contraction. An optical-depth-dependent exponential damping term turns out to be ineffective in such a situation, because the artificial effect occurs in a region of rather low optical depth. Devising a cure of these problems is currently work in progress. In the simulations of z9.6 and s9.0, the cooling implementation described above worked well and ensured a smooth and continuous contraction of the PNS with a gradient nicely extrapolating the behavior of the VERTEX-PROMETHEUS simulations.

Nevertheless, in the case of the s9.0 progenitor we encountered the mentioned issues with runaway cooling in a thin shell in the deep interior of the PNS. Instead of fixing them by a hard cut-off of the local cooling, we globally switched off the anyway low energy and lepton-number loss rates of Equations (E1) and (E5), respectively, at ∼ 1 s after bounce and continued our simulation with gain-layer heating only. Since the PNS radius at that time had decreased to 20 km already and its further contraction was only slow, we could not witness any transient or discontinuous behavior as a consequence of our measure. In order to account for the subsequent shallow PNS contraction seen in the guiding 1D PNS-cooling simulation, which would shift R_{gain} in the 3D run closer in (see Equation (E8)) and thus would enhance the heating of the PNS surroundings, we scale Equations (E2) and (E6) with another factor

$$f_{\text{NS}} = \max \left\{ 1, \left(\frac{R_{\text{NS}}(t)}{R_{\text{NS}}^{\text{1D}}(t)} \right)^2 \right\} . \tag{E9}$$

Here, $R_{\text{NS}}^{\text{1D}}$ is adopted from the corresponding 1D model that also provides the time-dependent neutrino luminosities and mean energies used in the scaling factors of f_L and f_E in Equations (E3) and (E4), as well as in Y_e^{eq}. This scaling increases the source rates Q_{erg}^+ and Q_{lep}^+ when the PNS radius in the 1D simulation with VERTEX-PROMETHEUS becomes smaller than in our 3D simulation with simplified neutrino treatment, thus ensuring that neutrino heating at the bottom of the SN ejecta is not underestimated.

E2 Neutrino pressure correction

Switching off the neutrino transport would also lead to a sudden drop of pressure support in the high-density regime, if the contributions of neutrinos to the total pressure were ignored. To avoid unphysical artifacts (such as PNS oscillations), we replace the neutrino-momentum source term in the hydrodynamics equations by an adequate neutrino-pressure contribution that is added to the gas pressure.

Assuming that neutrinos are in local chemical equilibrium with matter at sufficiently high densities, we can employ the following analytic expression (using the sums of relativistic fermi integrals from Bludman & van Riper 1978):

$$p_\nu^{\text{eq}} = \frac{4\pi(k_{\text{b}}T)^4}{3(hc)^3} \left[\frac{21\pi^4}{60} + \frac{1}{2}\eta_{\nu_e}^2 \left(\pi^2 + \frac{1}{2}\eta_{\nu_e}^2 \right) \right] , \tag{E10}$$

where T is the local temperature, k_{b} Boltzmann's constant, and $\eta_{\nu_e} = \mu_{\nu_e}/(k_{\text{b}}T)$ the degeneracy parameter of electron neutrinos,

with μ_{ν_e} denoting the ν_e chemical potential. Equation (E10) includes the pressure contributions from neutrinos and antineutrinos of all three flavors with $\mu_\nu = 0$ for both muon and tau neutrinos.

Since the assumption of local chemical equilibrium does not hold in regions of low matter densities, i.e., close to and outside of the neutrinosphere, we describe the neutrino pressure in the entire computational domain according to

$$p_\nu = p_\nu^{\text{eq}} \cdot f_p(\rho) \cdot \min \left\{ 1, \frac{\rho}{10^{13} \text{ g/cm}^3} \right\} , \tag{E11}$$

where the expression in the curly braces reduces the neutrino pressure gradually with decreasing density, and the density dependent factor $f_p(\rho)$ is defined as

$$f_p(\rho) = \frac{p_{\text{VERTEX}}(\rho, t_0)}{p_\nu^{\text{eq}}(\rho, t_0)} . \tag{E12}$$

It is computed as the ratio of the neutrino pressure from the VERTEX transport module, p_{VERTEX}, to the analytical equilibrium-neutrino pressure according to Equation (E10). Both the numerator and the denominator of Equation (E12) are evaluated at time t_0 (when we change our neutrino treatment) and averaged over all directions. The ratio is then tabulated as a function of the matter density, ρ. At high densities the factor of Equation (E12) is applied to correct for a possible small mismatch of the analytic equilibrium pressure of Equation (E10) and the numerical value from the VERTEX transport, connected to resolution and discretization effects. With the same prescriptions we also include the neutrino energy and pressure contributions to the general relativistic corrections in the effective gravitational potential (case A) of Marek et al. (2006). Again, this treatment ensures a minimum of numerical noise and, as well as possible, it allows for a transient-free transition when the VERTEX transport is replaced by our approximate heating and cooling description.